The University Of Sheffield.

Unsteady Aerodynamics of Vertical Axis Wind Turbines

Nidiana Rosado Hau

A thesis submitted in partial fulfilment of the requirements for the degree of Doctor of Philosophy

The University of Sheffield
Faculty of Engineering
Department of Mechanical Engineering

January, 2021

I, the author, confirm that the Thesis title "Unsteady aerodynamics of vertical axis wind turbines" is my own work. I am aware of the University's Guidance on the Use of Unfair Means (*www.sheffield.ac.uk /ssid/unfair − means*). This work has not been previously presented for an award at this, or any other, university. This thesis is accompanied for some published research articles and some of them in preparation as follows:

- (Published) Rosado Hau N., Ma L., Ingham D. & Pourkashanian M., A critical analysis of the stall onset in vertical axis wind turbines, Journal of Wind Engineering and Industrial Aerodynamics, Vol 204, September 2020.
- (Published) Rosado Hau N., Ma L., Ingham D. & Pourkashanian M. , A Procedure to Predict the Power Coefficient of Vertical Axis Wind Turbines at Low Tip Speed Ratios, Conference proceedings, AIAA Scitech 2019 Forum, San Diego California, *https://doi.org/*10.2514 /6.2019 − 1066.
- (In preparation) Rosado Hau N., Ma L., Ingham D. & Pourkashanian M , Effect of the upstream and downstream torque contributions on the performance of vertical axis wind turbines

Signature_____

Date_____

ACKNOWLEDGMENTS

I would like to express my deep gratitude to Professor Lin Ma, Derek Ingham and Mohamed Pourkashanian, my research supervisors, for their guidance during these four years and their patience in the reading and improvement of this thesis.

I wish to thank to the National Council of Science and Technology (CONACYT) and the Secretary of Energy of Mexico (SENER) for the PhD funding and for give me the opportunity to learn in an international environment.

I also want to extent my special gratitude to my friends, especially to Mohamed El Sakka and Oscar Farias for their valuable support during my CFD learning process.

This thesis is dedicated with all my love to my parents, Filomeno Rosado Gonzalez and Benigna Hau, who taught me to never stop learning from others.
To my dear David F. Morales Aldana and his family for all their support and affection during all these years.

When you think you have no reason to go on, use that pain to create your own art. Someone, somewhere and somehow, will be inspired by your resilience.
Nidiana

ABSTRACT

This thesis aims to substantially contribute to the understanding of the unsteady aerodynamics that remains unclear in the VAWTs. The analysis has been carried out by using computational fluid dynamics techniques very carefully verified with experimental data and using a modified Leishman-Beddoes dynamic stall algorithm. The results of this investigation are based on the analysis of oscillating aerofoils at constant and time-varying Reynolds and VAWTs with one, two and three blades evaluated at the tip speed ratio range of 1.5-5 using four symmetrical aerofoils and two-cambered aerofoils. The results have shown that: (i) the stall-onset angle in the VAWTs is defined by the combined effect of the tip speed ratio, pitch angle, angular frequency and relative velocity in the final value of the non-dimensional pitch rate when the angle of attack approaches the static stall angle; (ii) Under the fully attached regime, the symmetrical aerofoils performed better than the cambered aerofoils especially at the downstream zone of the rotor. This zone has shown to play the most significant role in the reduction of the overall torque coefficient and this reduction increases with the tip speed ratio, thus, a poor lift force coefficient at negative angles of attack can mitigate the advantages of a high lift/drag aerofoil observed at positive angles of attack. (iii) The curvature effect becomes more relevant with the increase of the tip speed ratio but also appears to be affected by the number of blades, therefore, a fast tool to design VAWTs needs to take into account this phenomenon in order to give reliable results. In the methods proposed in this thesis, despite being limited to the cases investigated, they demonstrate to be a potential tool to predict the unsteady loads in the VAWTs. The present investigation gives sufficient aerodynamic information to design strategies that improve VAWT performance.

CONTENTS

NOMENCLATURE

A Area

C Constant variable

C_C, C_D, C_L Chordwise, drag and lift force coefficients

C_{D0} Drag coefficient at zero angle of attack

$C_{L\alpha}$ Slope of the static attached flow coefficients

C_{N1} Normal force at the separation point

$C^I_{N\alpha}$ Impulsive component due step change in the angle of attack

C^I_{Nq} Impulsive component due to the pitch rate

C_N Normal force coefficient

C^C_N Circulatory component of the normal force

C^f_N Boundary layer component of the normal force

C^v_N Vortex component of the normal force

C_P Power coefficient

$C_{Q,T}$ Total torque coefficient

C_Q Torque coefficient

C_R, C_T Radial and tangential force coefficient on a VAWT.

C_{fx} Skin friction, $\sigma_x/0.5\rho U^2_{ref}$

D Rotor diameter, m

$D_I, D_q, D_f, D_p, D_\alpha$ Deficiency functions

E_0 Parameter to adjust the static chordwise force coefficient

L, M Lift stall and moment stall points

N_b Number of blades

N_{th} Number of streamtubes elements

P_{coeff} Pressure coefficient

R Rotor radius, m

S_1,S_2 Parameters to adjust the Kirchoff flow equation.

T Period of oscillation

T_p Time delay constant base in the pressure criteria

T_r Time delay constant base in the chordwise force criteria

U Incoming wind flow for the oscillating aerofoil, m/s

U_{ref} Actual wind speed on the aerofoil, m/s

V_∞ Free stream wind velocity in the VAWTs, m/s

V_{dw} Induced velocity on the downwind rotor

V_e Equilibrium velocity between the upwind and the downwind rotor

V_{inst} Wind sped at a specific time, m/s

V_{mean} Average of the relative velocity in one revolution, m/s

V_{rel} Relative velocity, m/s

V_{up} Induced velocity on the upwind rotor

V_x X-component of the wind velocity, m/s

X, Y Deficiency functions

X_r Local tip speed ratio, $\omega R/V$

a_1, a_2 Maximum interference factors at upstream and downstream respectively

c Chord, m

d_i, d_w, d_o Geometrical dimensions of the mesh domain.

dw Downstream

f Non dimensional static separation point, $f = x/c$

f_{crt} Critical point of the TE separation point

n Number of time step

q Non-dimensional pitch rate

r Normalized pitch rate $q = \dot{\alpha}c/V$

t Time, s

u, u' Interference factors, upstream and downstream

up Upstream

x/c Non-dimensional chord distance

Δs Non-dimensional time step, $2U_{ref}\Delta t/c$

Δt_{sep} Time elapsed from the static to the dynamic stall angle

α Angle of attack, ($^\circ$)

α_0 Virtual increase in the effective angle due to the camber effects, (°)

α_E Effective angle

α_f Effective angle of the dynamic separation point

α_{max} Maximum angle of attack in the upstroke

α_{os} Dynamic stall-onset angle, (°)

α_{ss} Static stall angle, (°)

β Pitch angle, (°)

δ Angle between the blades and the z-axis

$\dot{\alpha}$ Pitch rate, (rad/s)

γ Compressibility factor $\sqrt{1-M^2}$

κ Reduced frequency, $(\omega c/2U_{ref})$

λ Tip speed ratio, $\omega R/V_\infty$

ω Rotational speed, rad/s

ϕ Path angle, (°)

ρ Density

σ Solidity, $(N_b c/2R)$

τ Non-dimensional time constant, (t/T)

θ Azimuthal angle, (°)

θ_{in} Azimuthal angle with the stall inception, (°)

θ_{max} Azimuthal angle with a maximum C_Q, (°)

LIST OF FIGURES

LIST OF TABLES

LIST OF ACRONYMS

AOA Angle of attack

CFD Computational Fluid Dynamics

CFL Courant-Friedrichs-Lewy

DMST Double Multiple Stream Theory

HAWT Horizontal Axis Wind Turbine

LB Leishman-Beddoes

LE Leading Edge

LES Large Eddy Simulation

LSB Laminar Separated Bubble

TSR Tip Speed Ratio

TE Trailing Edge

PIV Particle Image Velocimetry

RANS Reynolds-averaged Navier-Stokes equations

VAWT Vertical Axis Wind Turbine

Chapter 1

Introduction

1.1 Background

The use of renewable energies to produce electricity has rapidly expanded all around the world in the last few years. This expansion has been due to the growing interest in reducing the $C0_2$ emissions produced by the electricity sector when using fossil fuels. Therefore, some international agreements have been achieved in order to reduce the CO_2 emissions by many of the countries throughout the world [11].

Among the renewable energy technologies, the wind energy has continued to gain more attention since it is considered to be the most competitive economically regarding the traditional fossil fuels technologies and has been demonstrated to be the least expensive renewable energy at the end of 2018 [12]. Wind energy technologies consist mainly of horizontal axis wind turbines (HAWTs) and vertical axis wind turbines (VAWTs).

HAWTs are typically spread out as large wind farms. Still, despite the maturity of the HAWT technology [13, 14, 15, 16, 17], some issues regarding the grid interconnections remain to be solved due to the centralization of the power systems [16]. Also, large farms require to be located in locations with very good wind resource, i.e. high average wind speed, over 10 m/s and far away from the ground obstacles in order to reduce the wind turbulence and thus the increasing of the tower-height [18, 14, 16].

VAWTs, despite being a technology under development, have been demonstrated to have a huge potential to be installed in urban regions and thus closer to the consumer locations [19]. For example, (i) VAWTs present omnidirectional capabilities without a need of an alignment system to the wind direction, and operate independently of the variable wind direction; (ii) have less sensitivity to the turbulence created by the

ground obstacles and due to this feature, the cost of installing the VAWTs tower is reduced compared with the HAWTs, and (iii) the VAWT produces less noise during its operation.

Due to the above-mentioned advantages of the VAWTs, the improvement in their energy production has become of much interest in the last few years [20, 21, 22, 23]. From the two different classifications of VAWTs, namely, the Savonius and Darrieus, the last one has been demonstrated to have the largest power coefficient [2] and therefore is the concept most widely studied and it is the one selected in this investigation.

The fully understanding of the VAWT aerodynamics is fundamental in order to improve its power performance. Due to the high number of geometrical and operating conditions involved during the VAWT operation, investigating its aerodynamics becomes a very complex task. In the past, the investigation of the VAWTs performance and their aerodynamics relied on experimental tests. Due to the constantly rotating of the blades, the acquisition of the unsteady loads faces many technical challenges, and hence the most typically reported data is the power coefficient [24].

Nowadays, with the advances in computer science, computational fluid dynamics techniques (CFD) that are properly verified with experimental data offers an excellent option to obtain more in-depth details of the flow field around the blades. Therefore, its use to study VAWTs has been extended in the last few years [6, 25, 26, 27, 28, 29] However, despite the many efforts to investigate the VAWTs, most of the studies have focused on the analysis of the power performance, and prevails the need of more detailed analysis of the VAWTs aerodynamics such as the vorticity evolution, the tangential, normal and torque coefficients both upstream and downstream of the rotor [30, 24, 31, 32, 9].

Some of the important aspects of the unsteady aerodynamics in VAWTs, such as the dynamic stall phenomenon and the curvature effects, both upstream and downstream of the rotor, prevails not to be very well understood. Recent studies have demonstrated that the dynamic stall takes place under low tip speed ratios [7, 33] but others parameters, such as the index chord/radius, may play a significant role in defining the stall-inception [7]. Since dynamic stall has been demonstrated to cause a reduction in the power coefficient, there is an urgent need to investigate the causes of this phe-

nomenon in the VAWTs.

During the operation of the VAWTs at high tip speed ratio, where dynamic stall does not take place, it has been observed that there is a decrease in the power coefficient and this has been associated to secondary effects such as the shaft, arms, etc. In addition, a few investigations on the curvature effect have shown that this parameter becomes significant at high tip speed ratios but its influence on the VAWT performance at both upstream and downstream of the rotor remains also unrevealed.

Overall, the lack of understanding in the above-described aspects of the VAWTs aerodynamics has limited the development of a fast engineering tool that is capable of accurately and quickly predicting the power coefficient of any VAWT. That means that although many efforts have been made in the past in order to develop a fast tool capable of predicting the power coefficient of any VAWT, none of the existing methods are reliable since many aspects of the VAWT aerodynamics remains unclear and as a result, on using current methods, requires a strict verification with experimental data, and this has not been available until the last few years.

1.2 Aims and objectives of this thesis

The aim of this thesis is to contribute to a much better understanding of the unsteady aerodynamics of the vertical axis wind turbines at both sides, upstream and downstream, of the VAWT rotor and then, to contribute to the development of an engineering tool that is capable of predicting accurately the unsteady loads on VAWTs.

This thesis bridges some of the most important and essential gaps in the unsteady aerodynamics of VAWTs that contribute to the progress in the maturity of the VAWT technology as described in the following major objectives:

- To elucidate the significance of the chord, rotational speed, tip speed ratio, pitch angle, Reynolds number and relative velocity in the stall-inception of the VAWTs.

- To analyse the unsteady aerodynamics at both zones of the rotor with the increase of the tip speed ratio by using symmetrical and cambered aerofoils.

- To assess and modify the Leishman-Beddoes algorithm in order to be able to accurately predict the unsteady loads of oscillating aerofoils and VAWTs in the range of Reynolds number of $0.8 - 3.3 \times 10^5$.

- To investigate the influence of the tip speed ratio and the number of blades on the induced-virtual camber due to the curvature effects.

- To developed a new method that is able to predict accurately the unsteady loads present under dynamic stall and non-stall conditions.

This investigation uses computational fluid dynamic simulations that have been rigorously assessed for oscillating aerofoils and vertical axis wind turbine unsteady loads, i.e. the azimuthal torque coefficient in both the upstream and downstream regions of the rotor at several tip speed ratios. Further, the Leishman-Beddoes model has been employed to compute and validate the modelling results with the experimental data for oscillating aerofoils and to assess it as a tool to predict the unsteady loads on the VAWTs. The more pertinent modification to the dynamic stall model was made in order to consider the influence of the number of blades and this model was very useful to understand the influence of the curvature effect on the VAWT performance. Moreover, the double multiple streamtube theory has been assessed in the prediction of the unsteady loads at both zones of the rotor.

1.3 Limitations

This investigation is limited to the range of solidity 0.1325-0.3975 and this range is considered to be in the range of interest in VAWTs design for urban locations. Additionally, this investigation has considered two-dimensional analyses, and thus 3D effects are not considered but this is an important issue that needs to be fully investigated in the future in order to include the best corrections to the 2D model.

In order to obtain a full engineering tool that is capable of predicting the VAWT performance under any operating conditions, more effort is required in the understanding of the unsteady aerodynamics that characterizes these devices, constantly changing

in both the angle of attack and relative velocity and to develop a mathematical model that best reflects the physics of the flow. Despite this, the thesis has addressed the issues that are most urgent to be investigated and has laid out the solid groundwork for future improvements.

1.4 Outline of the thesis

This thesis includes in Chapter 2 a valuable background of unsteady aerodynamics with a focus on the dynamic stall phenomenon and the current theory stage. In addition, it presents a literature review of the unsteady aerodynamic theory of VAWTs that describes the aspects that until now remain unrevealed.

Chapter 3 describes the research methodology followed in this thesis and gives more insights into the methods adopted to investigate the unsteady aerodynamics, namely, the CFD simulations, the Leishman-Beddoes dynamics stall and some discussion of the double multiple streamtube method as a fast tool to predict the performance of VAWTs. As a novel outcome of this chapter, the verification with experimental data of the CFD numerical technique to predict the torque coefficient at the downstream of the rotor at several tip speed ratios is included.

Chapter 4 includes for the first time an extensive analysis of the operating conditions of VAWTs that influence the stall-inception. The tip speed ratio, reduced frequency, pitch angle, relative velocity, Reynolds number and aerofoil profile are investigated using an oscillating aerofoil that describes the angle of attack and relative velocity present in VAWTs. The results are fundamental in the understanding of the dynamic stall in any VAWT since it has correlated the influence of the operating conditions with the stall inception.

Chapter 5 evaluates the upstream and downstream contribution of the torque coefficient for several aerofoils in order to better understand the range of tip speed ratios where dynamic stall takes place and to correlate the behaviour of the azimuthal torque coefficient with the optimum tip speed ratio of operation on the VAWTs. These results present much useful information that enables one to identify the important behaviour, not only of the dynamic stall phenomenon but also on the poor unsteady forces down-

stream of the rotor, with the increase in the tip speed ratio.

Chapter 6 discusses the key parameters of the Leishman-Beddoes dynamic stall to predict the unsteady loads at low Reynolds number in the range of $0.8-3.3\times10^5$. In addition, it computes the time delay constant of the aerofoils NACA0015, NACA0018 and NACA0021 within the mentioned range of Reynolds number not previously reported in the literature. The modifications to the LB algorithm are described and assessed in the prediction of the unsteady loads for oscillating aerofoils under dynamic stall conditions. Additionally, the assessment of the double multiple streamtube method coupled with the modified LB algorithm to predict the VAWTs performance is carried out.

Chapter 7, the last research chapter, analyses the curvature effect due to the tip speed ratio and the number of blades using CFD simulations and the modified LB dynamic stall model. In addition, the interference factor, both upstream and downstream of the rotor, was investigated and a mathematical relationship was proposed. For the virtual incidence due to the curvature effects, it is found that there is a mathematical relationship with the tip speed ratio and the number of blades. The virtual incidence increases with the tip speed ratio but at the same tip speed ratio reduced its value with the increase in the number of blades. The present findings have allowed the proposing of a new method that is promising in predicting the unsteady loads of VAWT and that takes into account the dynamic stall and non-stall conditions.

Finally, in Chapter 8 the general conclusions of these investigations are presented as well a discussion of the limitations and future work that will further improve the prediction of VAWTs.

Chapter 2

Unsteady aerodynamics

2.1 Background

Aerodynamics is defined as the science of the fluid dynamics dealing with the interaction between the air and a solid body when a relative movement exists between them [34]. When the properties of the fluid are considered to be independent of the time, the aerodynamics is called steady; when the nature of the flow field is characterized by a time-dependent variation of their parameters at a given position, then the aerodynamics is called unsteady [34]. The unsteady aerodynamics may result from a different number of unsteady sources. For example, from a non-uniform velocity such as from a sudden gust or a time-varying incident flow and, from the movement pattern described by the solid body merged into a flow field such as rotation, pitching, plunging, flutter, etc. [35].

The great interest in unsteady aerodynamics has emerged when the use of a steady aerodynamic analysis was not able to explain and predict the loads present in devices such as wings and helicopters [36]. After that, over the years, the interest has been ever increasing since unsteady aerodynamics can explain the reason why some insects are able to fly [37] and more recently to improve the design of unmanned aerial vehicles performance [38] and wind turbines [39].

In the earliest development of unsteady theories, Theodorsen [40] proposed an analytical solution based on the non-stationary potential flow to predict the loads on a wing section oscillating within a very small amplitude of oscillation. At that time, the large amplitudes of oscillation were neglected since the interest was focused on predicting the loads due to the flutter motion of the wings. After that, with the growing aircraft industry and the interest to improve the performance and design of those vehi-

cles, the number of experimental tests increased as well as the theories which proposed some analytical solutions to predict the loads due to different unsteady mechanisms [39, 41, 42].

An interesting phenomenon, called dynamic stall and related to the unsteady aerodynamics was discovered for the first time in helicopters as stated in [39]. Since then, enormous efforts have been made experimentally in order to understand its physics and its influence on the aerodynamic loads. Many experiments using aerofoils oscillating and describing the movement pattern of the blades, that usually takes place on helicopters, have been performed under several conditions. For example, the influence of variables such as the Mach number, Reynolds number, oscillatory frequency, mean and amplitudes in the angles of oscillation, aerofoils shape, etc. have been carried out [43, 44, 4, 45, 46]. All these investigations have led to a much better understanding of the unsteady aerodynamics and to the development of semi-empirical mathematical methods, that use the Theodorsen theory as a basis [41] and that are able to predict the unsteady aerodynamic loads due to the influence of the dynamic stall phenomenon.

The two main characteristics that have been observed under unsteady conditions are the time-lag in the aerodynamic response of the aerofoil regarding the steady conditions, and the presence of the dynamic stall phenomenon characterised by a vortex formation near the leading edge of the aerofoil. The transient mechanism may cause an effective angle of attack (the angle between the incident wind velocity and the chord of the aerofoil) being larger than the static stall angle (the moment when a sudden loss in the static forces is observed as shown in Fig. 2.1(a). This figure 2.1(a) includes the normal force coefficient (the resultant aerodynamic force perpendicular to the aerofoil-chord when a flow past the aerofoil surface) as a function of the angle of attack for a steady aerofoil NACA0015 and, an oscillatory NACA0015 where the angle of attack is within the static stall angle. The Fig. 2.1(b) includes the normal force coefficient for a steady aerofoil NACA0015 and, an oscillatory NACA0015 describing an angle of attack that goes further the static stall angle.

Either the transient mechanism produces an angle of attack within the static stall angle or larger than the static stall angle, then the time lag takes place. Under this regime, called the unsteady attached regime, the observed force coefficient presents a

lower magnitude than the steady values during the upstroke motion (with an increase in the angle of attack) and presents larger values than the steady values during the downstroke motion (with the decrease in the angle of attack), see Fig. 2.1(a). A more detailed discussion is included in [35, 47].

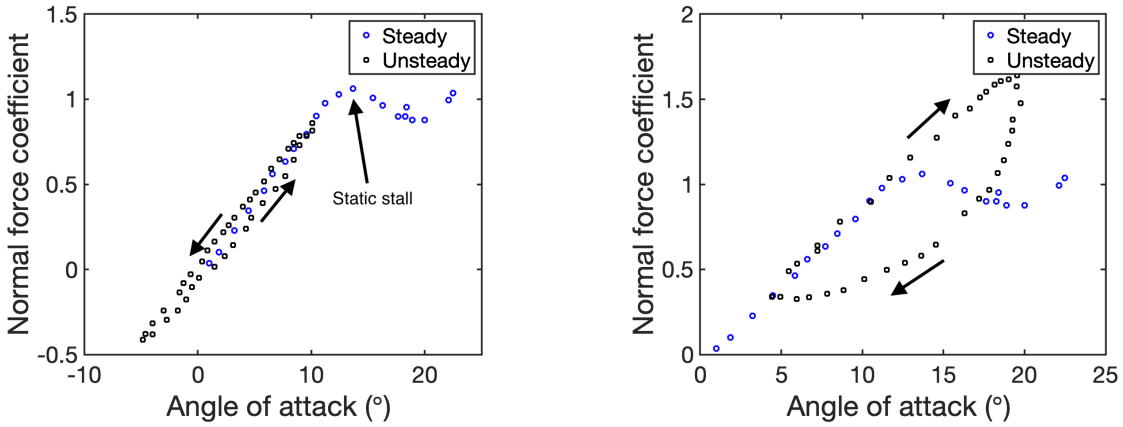

Figure 2.1: The normal force coefficient as a function of the angle of attack for a steady NACA0015 aerofoil at Reynold number of 1.5×10^6 compared with the normal force coefficient of oscillatory NACA0015 with a maximum angle of attack (a) within the static stall angle and, (b) larger than the static stall angle [1].

The second characteristic of the unsteady aerodynamics is the development of the dynamic stall phenomenon that may take place when the effective angle of attack increases further than the static stall angle. In Fig. 2.1(b), the normal force coefficient on an oscillating aerofoil describing an angle of attack that goes beyond the static stall angle is presented [1]. It is observed that under this unsteady condition, the force coefficient stalls at a larger angle of attack and a large hysteresis is described in the force coefficient during the downstroke motion of the aerofoil. More details of this phenomenon are included later in this section.

In vertical axis wind turbines, two main sources of unsteadiness are found, namely, the oscillating values in both the angle of attack and the incident velocity on the blades through one cycle of the VAWT rotor [2]. The aerodynamic investigations have proposed that the dynamic stall phenomenon is likely to take place at low tip speed ratios,

that is the ratio between the tangential speed of the blades and the free-stream velocity, and usually, where large amplitudes of the angle of attack are experienced [33]. In contrast, at high tip speed ratios, the absence of this phenomenon occurs, but the unsteady effect may take place, as explained above, for smaller amplitudes of the angle of attack under attached flows [30].

Despite that, the use of the available dynamic stall methods to predict the unsteady loads in VAWTs appears to be a good idea [48, 49], its efficiency or deficiency and the assumptions considered in the methods, remains without any solid supporting analysis due to the following three main issues.

(i) VAWTs suffer from a combined transient effect of the angle of attack and the incident velocity on the blades during one cycle of the rotation. The impact of these simultaneous mechanisms in the dynamic stall has been rarely investigated and this is attributed mainly to the complexity in replicating experimentally the time-varying incoming flows [50].

(ii) The dynamic stall has been demonstrated to depend on several variables, such as the frequency of oscillation, and the mean and amplitudes of the angles of oscillations, Reynolds number, Mach number, aerofoil profile and the movement pattern, i.e. the function described by the angle of attack. Also, many of the investigations on dynamic stall have used a sine function as the variation in time of the angle of attack. In addition, the typical angle of the attack described in a VAWT has been little investigated and these investigations have concentrated mainly on Reynolds number larger than 1 million. Therefore, the influence of the Reynolds number lower than one million on the dynamic stall remains unclear [1, 51].

(iii) There is a shortage of experimental data, including the unsteady loads on the VAWTs at both sides of the rotor and, under the dynamic stall and full attached regimes of operation. Thus, a more in-depth understanding of the unsteady aerodynamics on the VAWTs needs to be investigated in order to present a fair assessment of the application of dynamic stall methods to predict the VAWTs performance.

This thesis aims, in the first instance, to study and to analyse the dynamic stall phenomenon in vertical axis wind turbines and, later, with the knowledge gained, formulate a strategy to implement and improve the current dynamic stall methods to be

capable of considering the unsteady aerodynamics on both sides of the rotor and under both operating regimes, under the full-attached flow and dynamic stall conditions. The knowledge generated in this thesis and the devised formulation to apply the dynamic stall methods will encourage future works that will lead to the development of a fast unsteady tool applicable to the VAWTs analysis and design.

2.2 Aerodynamics on VAWTs

A top view of a VAWT with three blades is shown in Fig. 2.2 (a). The free-stream wind velocity, V_∞, is the undisturbed wind speed located before impacting the VAWT at the upstream zone of the rotor. The downstream zone of the rotor is the region of the rotor where the flow has been affected by the front zone of the VAWT rotor. In terms of the azimuthal angle (θ) which determines the position of one blade during its rotation, the upstream zone corresponds to $\theta = 0$ to $\theta = 180^\circ$ and the downstream zone corresponds to $\theta = 180$ to $\theta = 360^\circ$. The aerodynamic forces and the most relevant mathematical relations that govern the aerodynamic performance of a VAWT are illustrated in Fig. 2.2(b) and described as follows.

In a vertical axis wind turbine, the blades rotate about an axis with a rotational speed, ω, as indicated in Fig. 2.2(b). Each blade perceives an actual wind velocity (relative velocity) which is constantly changing in magnitude given by the following expression [2]:

$$V_{rel}(\theta) = V_\infty \sqrt{1 + 2\lambda \cos(\theta) + \lambda^2} \tag{2.1}$$

where λ is the tip speed ratio and is defined as the ratio of the tangential speed of the blades, ωR, and the free stream wind velocity, V_∞. The azimuthal position of the blades is calculated with the relation: $\theta = \omega t$, where t represents the time elapsed when the blade has passed the position $\theta = 0^\circ$ indicated in Fig. 2.2 (a).

The direction of the relative velocity is described by the angle of attack equation given by:

$$\alpha(\theta) = \phi - \beta \tag{2.2}$$

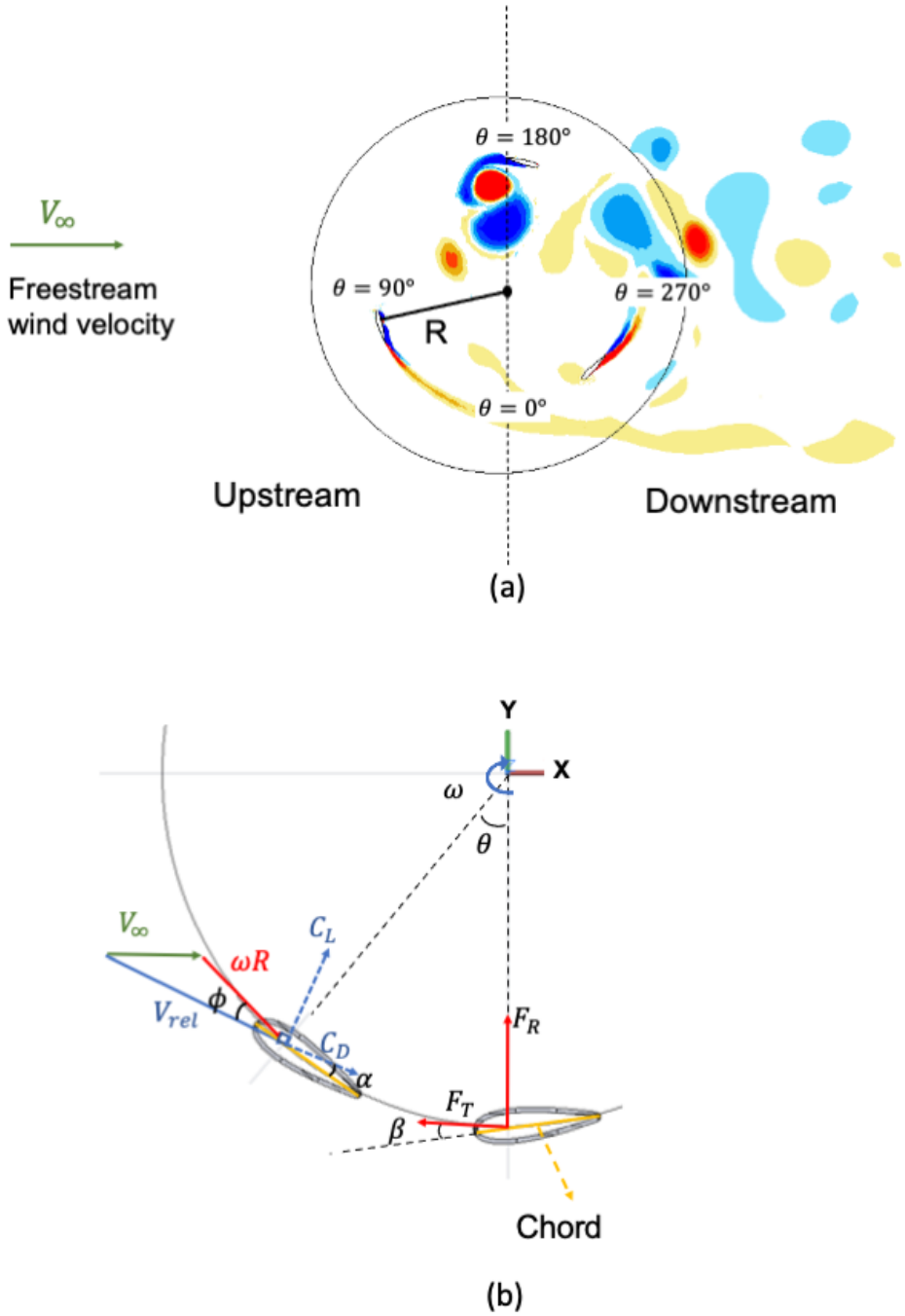

Figure 2.2: (a) A schematic representation of a three-bladed VAWT and its representative zones and, (b) a schematic representation of the aerodynamic forces generated during the rotation of the VAWT blade.

where β represents the pitch angle, and it is positive outwards from the circle described by the outer edge of the rotation of the blade, see Fig. 2.2. The path angle ϕ, is the angle between the tangential speed vector of the blade and the relative velocity and, is given by the following expression.

$$\phi(\theta) = \arctan(\frac{\sin(\theta)}{\lambda + \cos(\theta)}) \tag{2.3}$$

As was mentioned previously, the angle of attack is the angle between the relative velocity direction and the chord of the aerofoil. When the flow past the blades and the relative velocity impacts the aerofoil surface, thus the aerodynamic forces are generated and a tangential force (F_T) results, which finally produce the torque coefficient, C_Q, in the VAWT. Among the most relevant aerodynamic forces are the lift force coefficient, C_L, and the drag force coefficient, C_D. The lift force, L, is aerodynamic force that is perpendicular to the relative velocity and, in VAWTs the lift force coefficient is calculated with the next expression.

$$C_L = \frac{L}{1/2\rho A_b V_{rel}^2} \tag{2.4}$$

where, A_b represents the blade area and typically is the product of the chord length, c with the span-length of the blade, H. The drag force, D, is the aerodynamic force parallels to the relative velocity of the blades and the the drag force coefficient in the VAWT blade is calculated with the next expression:

$$C_D = \frac{D}{1/2\rho A_b V_{rel}^2} \tag{2.5}$$

Both equations of C_L and C_D are used with steady simulations but instead of the V_{rel} the constant incoming flow velocity is used. The tangential force, F_T and the radial force F_R result of the lift and drag aerodynamic forces generated when the flow past the blades. The F_T is tangential to the circle describe by the rotation of the blades and the radial force, F_R, is the resultant aerodynamic force along the radius.

Both equations (2.1) and (2.2) are theoretical expressions and may be modified by the curvature index, that represents the ratio between the chord (c) and the radius

of the turbine (R); the number of blades and the streamlines expansion due to the presence of the rotor [2, 52, 10, 53, 54].

The typical performance of a VAWT rotor is represented by its power coefficient, C_P, as a function of the tip speed ratio, λ, as illustrated in Fig. 2.3. The power coefficient is the coefficient between the power generated by the wind turbine and the available wind power and is given by the following expression:

$$C_P = \frac{P}{0.5\rho V_\infty^3 A} \tag{2.6}$$

where A represents the transversal area of the rotor that is being impacted on by the incoming flow and ρ represents the air density.

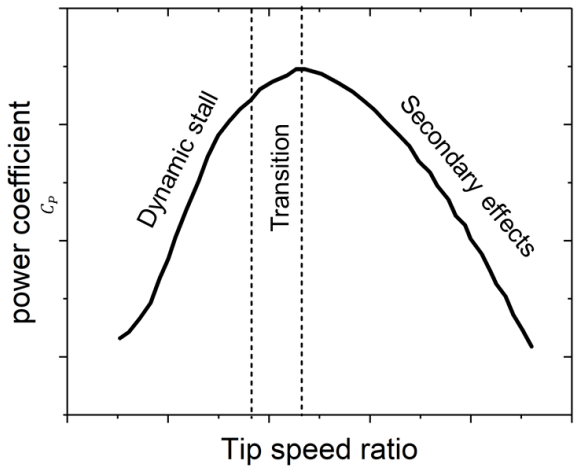

Figure 2.3: A typical power coefficient of a VAWT as a function of the tip speed ratio (the range of tip speed ratio might change accordingly to the VAWT design) [2].

As observed in Fig. 2.3, the power coefficient at low tip speed ratios is low and this is associated to the dynamic stall phenomenon [33, 55]. After an optimum value of C_P is reached , the power coefficient starts to decrease again and this is attributed to the low magnitude of the aerodynamic forces due to the decrease in the angle of attack and the secondary effects, such as the shaft, struts, etc. [2]. This typical curve of VAWTs is the result of the extensive experimental tests carried out by the Sandia Laboratories since 1968 using mainly the NACA0012 and a rotor with very low solidities [56, 57]. Most of

the theory resulting from these experimental tests has been included in Paraschivoiu in [2].

In the book by Paraschivoiu [2] several parameters that influence the VAWT performance have been investigated, namely, the rotational speed, Reynolds number, aerofoil, number of blades, the chord length, struts, shaft, etc. As a result, a method called the double multiple stream-tube theory (DMST) was developed that analyses the rotor in two main regions, the upstream and downstream regions. This method uses the momentum theory and blade element theory and considers the flow to be inviscid and steady.

In the mentioned work [2], some efforts were made to include dynamic stall methods to improve the power predictions but, despite that, the details of the efficiency/deficiency of the dynamic stall methods were not clearly discussed. This is attributed to the fact that dynamic stall remains to be not well understood under the VAWTs conditions and due to the several parameters that affect the VAWTs unsteady loads are not suficient to fully understand the dynamic stall in VAWTs and PIV visualization, for example, are also crucial [33, 58].

2.2.1 Instantaneous loads on VAWTs

In order to gain a more in-depth understanding of the VAWTs aerodynamics, the non-integrated forces such as the tangential force, the pressure coefficient, the skin friction and the torque coefficient are required to be investigated at each azimuthal position. In the last few years, due to the progress on the measurements techniques and materials science, more detailed experimental data on VAWTs are becoming available.

Recently, Li et al. [54, 32, 31] has performed the most extensive experimental test on VAWTs using the NACA0021 aerofoil. The angle of attack, relative velocity, the tangential and radial forces, torque coefficient at each azimuthal angle for two, three, four and five blades can be found. Although these detailed data is provided for a few tip speed ratios, the data includes important representative conditions under the dynamic stall and high tip speed ratios. Also, the pressure coefficient is provided for some azimuthal angles. In addition, the power coefficient as a function of the tip speed ratio can be found for a range of tip speed ratios, a different number of blades and several

pitch angles. In the above mentioned experimental test, pressure taps in the mid-span of the blades were employed (approximating the measurements to be two-dimensional) and, additionally, a six-component balance was used to take into account the 3D effect of the rotor.

Nguyen et al. [24] measured the radial force coefficient as a function of the azimuthal angles for VAWTs with a NACA0021 aerofoil and four tip speed ratios in the range [1.84-4.57]. It is mentioned that only the radial force coefficients were measured due to the stiffness of the blades that were sufficient to not disturb the measurements. CFD simulations were also validated with these experimental data and it was found that there was a good agreement between the numerical and experimental data; however, some differences at the downstream zone of the rotor were found.

Vittecoq and Laneville in [59] measured the radial force coefficients and tangential force coefficients for a two-bladed VAWTs with the NACA0018. The radial force coefficient was presented for a range of tip speed ratios [1.5-5] while the tangential force coefficient was presented for tip speed ratios of 2, 2.5 and 3. It is mentioned that, for the tangential force coefficient downstream, the signal presented some complexity that required further analysis.

Rossander et al. [60] measured the radial and tangential force coefficients using load cells at the hub of a three-bladed VAWTs using a NACA0021 aerofoil. The method to measure the tangential force coefficients was concluded to be unsuitable due to the large fluctuations observed in the forces attributed to the dynamic oscillations on the blades. However, the radial force coefficients were consistent with the numerical estimations.

Peng et al. [61] have also performed experimental tests to measure the tangential and radial force coefficients as a function of the azimuthal angle of a three-bladed turbine. It is mentioned that because of the larger magnitude on the radial forces coefficient compared with the tangential force, larger errors where expected in the tangential forces and thus corrections were applied. A two-component force sensor was connected directly at the top and the bottom of the axis of each blade that used the NACA0018 aerofoil.

In the revision of the above experimental investigations [24, 59, 60] difficulties in

the measuring of the tangential forces as a function of the azimuthal angle have been discussed. The magnitude of the tangential forces are smaller than the radial forces and hence, the fluctuations and the errors found in the tangential forces coefficients are larger than in the radial force coefficients. In the case of Li. et al. [54, 32, 31], they used the pressure measurements in the mid-span and the actual flow field around the blade is used. This avoids the problem found in the previous investigations that used cell-loads.

As has been explained previously, the experimental tests represent many challenges when measuring the forces produced by the blades on a VAWT. The tangential force coefficient is considered to be the most relevant to investigate the performance of the VAWTs since the torque produced by the blade is the product of the tangential force and the radius [24] but it is the most difficult to be obtained accurately in experimental investigations. Therefore, validated computational fluid dynamic techniques still represent a crucial tool in order to assist in the prediction of the tangential and radial forces coefficients on the blades, as well to better understand the flow field development upstream and downstream of the rotor.

Due to the small amount of data available for the forces as a function of the angles of attack, very few CFD investigations on VAWTs have been verified accurately both upstream and downstream of the rotor [62, 24]. As a result, no single investigation has included an analysis of the unsteady aerodynamic forces as a function of the azimuthal angle with the increase in the tip speed ratio. Rather than this, the integrated value of the power coefficient as a function of the tip speed ratio has been widely considered to investigate the influence of several parameters.

Rezaeiha et al. in [29] have proposed a CFD numerical strategy that claims to be highly accurate since the power coefficient (C_P) as a function of the tip speed ratio (λ) showed a good agreement with the experimental data. Nevertheless, the power coefficient, C_P, showed a good agreement for the tip speed ratios before the optimum C_P and disagreement after this point. Since no comparison with the azimuthal torque coefficient or other non-integrated forces were made, a deeper analysis as to where those differences are coming from, i.e. coming from the upstream, downstream regions or both cannot be discussed. Further investigations by Rezaeiha et al. [63, 64] evaluated

the influence of the Reynolds number, number of blades, solidity and pitch angle in the power performance of VAWTs.

This thesis aims to analyse the unsteady aerodynamics at both sides, upstream and downstream of a VAWT and take into account the tip speed ratios where the dynamic stall occurs as well as where non-stall conditions are present. This information is substantial and very important in order to much better assess the capabilities of the method to be used to predict the power coefficient of VAWTs.

2.2.2 Dynamic stall on VAWTs

The dynamic stall phenomena have been widely studied experimentally for several unsteady motions, namely: pitching, flapping, fluttering, wind velocity variation in [58, 35, 43, 44, 4, 45, 46, 65]. In addition, using Large Eddy Simulation techniques the dynamic stall phenomenon has been investigated using oscillating aerofoils in [66, 67, 68, 69] and ramp-up test in [70, 3, 71]. A similar topology of this mechanism has been found among all the motion patterns, including the VAWTs according to the experimental observations using PIV (particle image velocimetry) technique in [30, 72, 33, 73]. For the purpose of this thesis, the main parameters involved to describe this phenomenon are explained in the following paragraphs.

In an unsteady motion with a rapid increase in the angle of attack, $\alpha(t)$ that goes further than the static stall angle then the dynamic stall phenomenon follows the next stages:

- At the static stall angle, α_{ss}, the dynamic boundary layer experiences a delay in the reversal flow (backflow) compared with the static case. Additionally, the lift force coefficient increases its value following the same trend as if it remains attached. The state of the boundary layer at this point plays a vital role in determining the dynamic stall delay [74].

- If $\alpha(t)$ increases further than α_{ss} then the flow reversal from the aerofoil trailing edge (TE) moves towards the leading edge (LE) and the laminar bubble that is concentrated at the aerofoil LE experiences a maximum in the pressure coefficient (negative), and then a vortex is initiated and detaches from the LE.

This point is called the stall-onset angle α_{os} and determines the inception of the stalling process. Additionally, at this point, the lift coefficient deviates from its linear attached trend and increases in value (over-lift) due to the movement of the vortex downstream along the chord of the aerofoil. (It should be noted that the stall-onset mechanism depends on the aerofoil thickness [75, 70]).

- If the increase in $\alpha(t)$ is sufficient to allow the vortex to reach the trailing edge, then the lift force reaches its maximum value, this is characterized by a significant peak, and then a sudden loss in the lift is observed, this point is known as lift stall (L). Consequently, the pitching moment coefficient diverges to high negative values; this point is called the moment stall (M). Multiple vortex sheddings are possible if the aerofoil motion does not change direction and the angle of attack continues increasing.

- With the decrease of $\alpha(t)$, and a change in the motion direction of the aerofoil, a boundary layer reattachment can take place, and a large hysteresis in the unsteady loads is observed [46].

The stall-onset angle is a critical parameter in describing the dynamic stall process since it marks the inception of the leading edge vortex; thus the success of a dynamic stall method depends on the accurate prediction of the stall-onset angle [46]. Despite that, the available experimental and numerical investigations have focused on describing the topology of the dynamic stall phenomenon [43, 46, 44, 41, 76, 4] rather than understanding the factors that dictate the stall inception. Additionally, the Reynolds numbers under investigation have been larger than 1 million. Therefore, there is still a need on understanding which physical parameters affect the stall onset at lower values of Reynolds number in order to fully describe this phenomenon in the VAWTs when these devices operate at low wind speeds.

The ramp-up tests that have a constant pitch rate $\dot{\alpha} = C$, have demonstrated this parameter as being the most crucial parameter to define the stall-onset in the experimental test carried out in[77, 74, 78, 79, 80, 81, 82]. High-fidelity techniques such as the Large eddy simulations (LES) are able to provide more insights into the flow

physics of the dynamic stall phenomenon such as the investigations in [70, 3, 71]. For instance, Sharma et al. [3] presented the evolution of the pressure coefficient and the skin friction along the aerofoil surface for the NACA0015 at a Reynolds number of 2×10^5 for a constant pitch rate motion. As observed in Fig. 2.4(a), with the increase in the angle of attack the transition point of the boundary layer, identified by the boundary between the negative and positive skin friction, moves towards the leading edge. Around the angle of attack of 19.3° the laminar separation bubble (LSB) bursts and full stall occurs. Similarly, the negative pressure coefficient of the suction side of the aerofoil surface is analysed in Fig. 2.4(b). For this parameter, a more negative pressure coefficient occurs around the leading edge of the aerofoil with the increase of the angle of attack, and when the LSB bursts then, the pressure coefficient reaches its most negative magnitude.

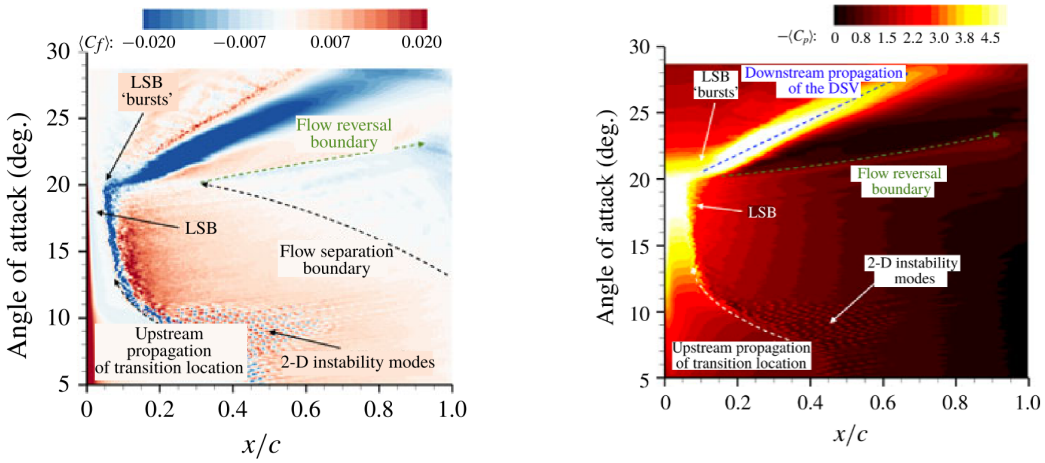

Figure 2.4: (a) Contours of spanwise-averaged skin friction coefficient (C_f) and (b) pressure coefficient on the suction side of the NACA0015 aerofoil through the constant pitch-rate motion at Re 2×10^5 and, using LES. [3]

To understand better the skin friction and pressure coefficient behaviour when the stall-onset is about to occur then five angles of attack are selected and included in Fig. 2.5 by Sharma et al. [3]. Fig. 2.5(a) shows that the pressure coefficient increases

its magnitude near the leading edge of the aerofoil with the increase in the angle of attack, at the angle of 19.3° a maximum peak in the pressure coefficient is observed and after this angle the pressure drops and this is due to the motion of the detached vortex that moves towards the trailing edge of the aerofoil with the further increase of the angle of attack. The skin friction reveals, in Fig. 2.5(b) that before the LSB burst, the transition point is about 25% of the chord length and the positive skin friction after the transition indicates a reattachment of the boundary layer as a turbulent boundary layer. With the increase in the angle of attack, the transition point moves towards the leading edge of the aerofoil and the skin friction indicates that the boundary layer loses its capabilities of reattachment with the increase in the angle of attack and after the angle of 19.3° the boundary layer stalls.

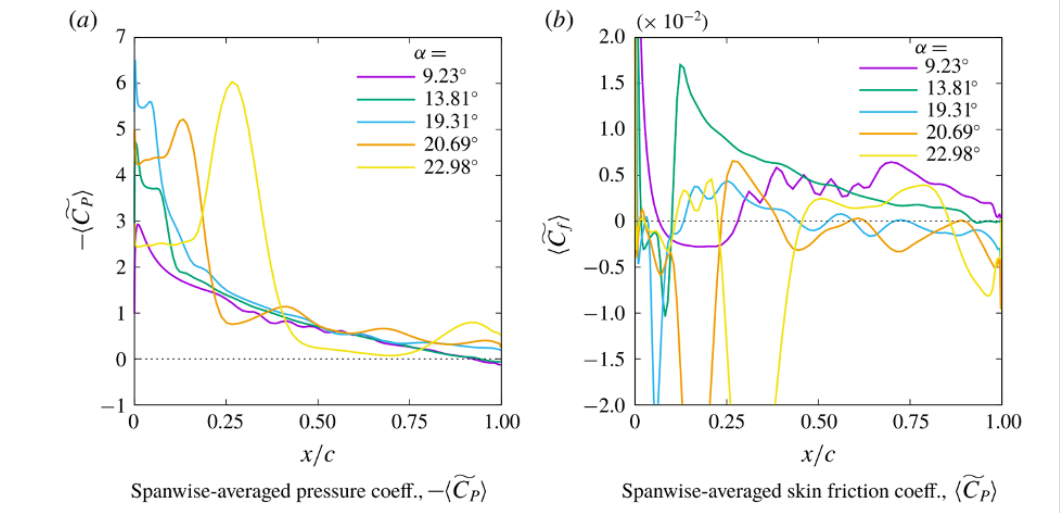

Figure 2.5: (a) Distributions of the pressure coefficient and, (b) the skin friction along the NACA0015 chord at five angle of attack during the pith up manoeuvre and at Re 2×10^5 using LES. [3]

In oscillating motions, where the pitch rate is a function given by $\dot{\alpha} = f(t)$, the variables that affect the inception point are less clear, since the amplitude and mean angle of oscillation and reduced frequency affect the angle of attack equation and hence the pitch rate function [65, 45, 36, 83].

Sheng et al. [65] evaluated the stall-onset angle of several oscillating aerofoils and they proposed, similar to the ramp-up tests, a non-dimensional parameter called the

equivalent reduced pitch rate that is the product of the amplitude and the reduced frequency. This equivalent reduced pitch rate was shown to be the most crucial parameter that defines the stall-onset in the oscillating motion. The same equivalent reduced pitch rate was used in [84] and a similar linear trend between the equivalent reduced pitch rate and the stall-onset angle was found.

More recently, Mulleners et al. [58] experimentally found for oscillating aerofoils that the non-dimensional pitch rate at the static-stall angle was the parameter that is the most critical factor in determining the stall-onset and the previous proposed equivalent reduced pitch rate in [65] did not show a clear relation with the stall-onset.

In the VAWT, when dynamic stall takes place, then this degrades its power coefficient and induces high structural loads on the rotor [2]. The vortex formation and its release to the wake characterize the dynamic stall on VAWTs. If the dynamic stall is severe, multiple vortices are released, and an additional decrease in the power coefficient is observed [85]. The generation of the vortices has been observed to be more prominent in the upstream section of the rotor but may appear downstream of the rotor [86, 55].

Thus, in order to improve the VAWTs performance and to regulate the dynamic stall that induces the undesired unsteady loads, determining the operational and physical parameters that control the stall-onset in the upstream region of the VAWTs rotor represents an essential task. Despite this importance, most of the investigations have been focused on describing the development of the dynamic stall phenomenon under some of the variables and, a very few investigations have paid attention to the stall-onset angle, the angle at which the vortex is released in the VAWTs.

Observations of the dynamic stall phenomenon using PIV techniques have been most studied by changing the tip speed ratio (TSR), but the dynamic stall has been observed at different TSRs values, and its influence remains unclear. For example, Fujisawa and Shubuya [33] observed the vortex formation for TSRs 1, 2 and 3; Brochier et al. [55] tested TSRs of 2.14 and 3.85, observing the dynamic stall for the lowest TSR. Simeira et al. [30] tested TSRs 2, 3 and 4 and the vortex formation was observed for TSRs 2 and 3; Laneville and Vittecoq [87] observed dynamic stall for TSRs less than 4. Moreover, Li et al. [73] observed dynamic stall for TSRs less than 1.8 and Edwards et

al. [88] observed the shedding vortex for TSRs from 2 to 4.

Recently, Bucher et al. [7] investigated the stall-onset angle using TSRs from 1 to 5, three Reynolds numbers (average) and three-chord lengths. It was concluded that the tip speed ratio alone is not sufficient to describe the stall-onset and the dynamic stall phenomenon. It is also recommended that more parameters, such as c/D, that relates the chord length and diameter needs more investigations.

In the VAWTs, the number of operating conditions that may affect the stall-onset angle is larger compared with the ramp-up and sine-pitching motions. For example, in the VAWTs the stall-onset can be affected by the tip speed ratio, pitch angle, rotational speed, Reynolds number and the constantly changing relative velocity. Thus, despite the efforts made by several authors, defining how these operating parameters affect the stall-onset angle results in a very complicated task when using a full wind turbine [7].

Now, the important research question is to know which variables and operating conditions affect the stall-onset in the VAWTs. Without answering this question, the possibilities to improve or assess a dynamic stall model are going to be minimal. Therefore, it is the main interest of this thesis to investigate how all the operating conditions present in the VAWTs affect its stall-onset angle, namely, tip speed ratio, pitch angle, rotational speed, Reynolds number and relative velocity. Since the experimental data to be used to assess the VAWTs in [31] is within the range of Reynolds number of $2-4\times10^5$, thus the stall-onset angle needs to be investigated within this range of Reynolds number. Therefore, this thesis investigates a range of Reynolds number that has not been previously investigated before (to the best of the knowledge of the author after an exhaustive literature review) and hence this thesis contributes with data that can be used for dynamic stall methods to accurately predict the unsteady forces at these Reynolds numbers.

2.3 Summary

In this chapter, it has been discussed the main characteristics of the unsteady aerodynamics, namely, the delay in the pressure response and the vortex formation at the

leading edge of the aerofoil causing the dynamic stall phenomenon.

Under the dynamic stall regime, it has been identified the existing gaps in the literature that remains unclear: how all the operating conditions of a VAWT affect the stall-onset angle. In addition, it has been identified as the need for understanding the stall-onset angle at Reynolds number lower than 1 million. At those low Reynolds numbers, the understanding of this phenomenon results crucial in order to improve the performance of VAWTs operating at low wind speeds and also, to improve the predicting methods of unsteady loads such as the dynamic stall models. This gaps in the literature are covered in Chapter 4.

This chapter also identified the existence of a severe shortage of experimental tests on the azimuthal force coefficient of VAWTs and thus encouraging the use of validated computational fluid dynamics in the prediction of the unsteady forces on VAWTs and to gain a much deeper insight into the aerodynamics. The assessment of the CFD simulations with experimental data consisting of azimuthal torque coefficient is presented in Chapter 3.

Moreover, it has been demonstrated the existence of a shortage in the details of the unsteady blades loads at upstream and downstream of the VAWTs. Then, investigating the aerodynamics characteristics of the aerofoils that are fundamental upstream and downstream of the rotor would reveal valuable information to improve the aerodynamic design of the aerofoils and the main aerodynamic characteristics that become more important with the increase of the tip speed ratio. This gaps in the literature are covered in Chapters 5 and 6.

Chapter 3

Methodology

3.1 Overview

As was mentioned in the previous chapter, there is a need for a full understanding of the unsteady aerodynamic of VAWTs in order to improve their performance and, to develop a fast engineering tool that is capable of predicting with accuracy the unsteady loads of the vertical axis wind turbines (VAWTs) under any operating regime, i.e., under the dynamic stall and full attached regimes. In order to bridge this gap in the literature then, a large analysis of the unsteady aerodynamics is carried out in this thesis. Starting with oscillating aerofoils to understand how the combined effect of the operating parameters in the VAWTs influence the stall-onset, followed by the CFD simulations of the full rotor under a wide range of tip speed ratios of operations and several aerofoils profiles and, last, using a dynamic stall-algorithm to obtain a more in-depth analysis of the aerodynamics of VAWTs under the dynamic stall and the unsteady attached regimes.

The steps that have been undertaken in this thesis and their corresponding method are presented schematically in Fig. 3.1 and described as following.

(i) The influence of the operating parameters on the stall-onset angle, namely, tip speed ratio, pitch angle and rotational speed is investigated by using an oscillating aerofoil describing the angle of attack on VAWTs with an incoming flow with a wind speed at a constant magnitude.

(ii) The influence of the relative velocity on the stall-onset angle is investigated using an oscillating aerofoil with an incoming flow with the fluctuating relative velocity found in VAWTs. These steps, (i) and (ii), used CFD simulations that were validated with experimental data of oscillatory aerofoils. More details of the employed CFD

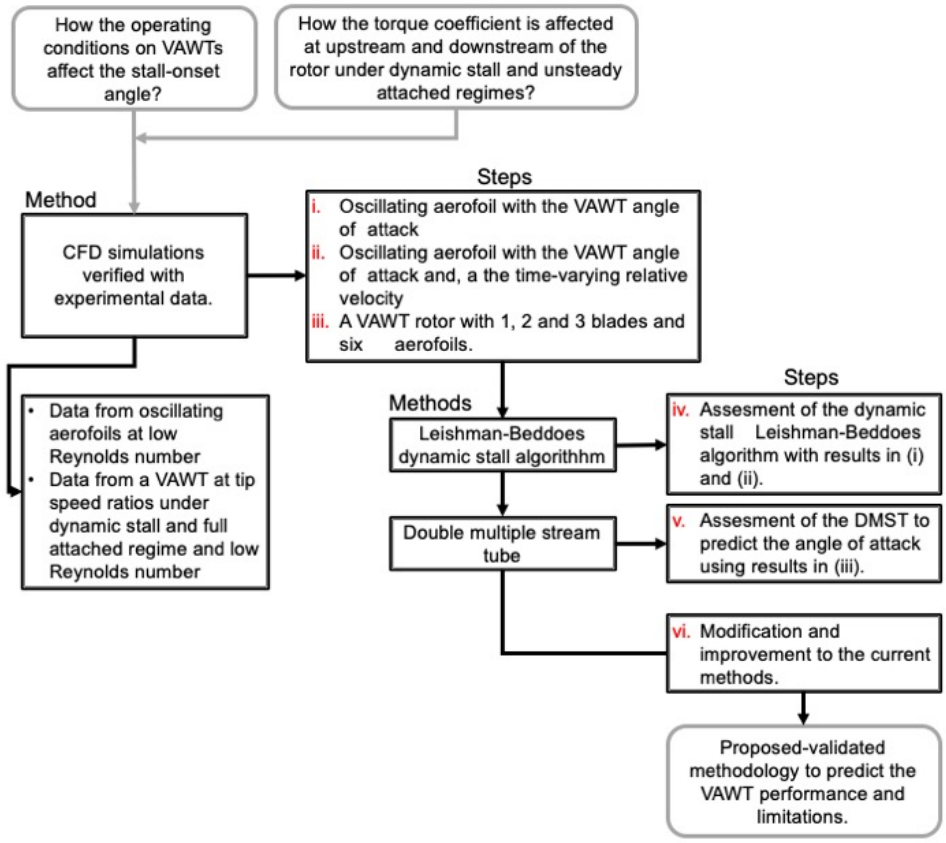

Figure 3.1: Schematic representation of the global methodology adopted in the thesis (philosophical methodology).

techniques are given in Section 3.2.2 and results are presented in Chapter 4.

(iii) Two-dimensional CFD simulations using one-bladed turbine were performed under a range of tip speed ratios of 2-5 and six aerofoils profiles were investigated. After that, the two-bladed turbine was investigated under a TSRs range 1.5-4, and also the six aerofoil profiles were analysed. Last, a three-bladed VAWTs was analysed at the range of TSRs 1.5-3.5 and again the six aerofoils were investigated. These simulations were enough to study the unsteady aerodynamics of VAWTs at both upstream

and downstream of the rotor and also, under both regimes of operation, the dynamic stall and unsteady full attached regime. The VAWTs CFD simulations were carefully verified with the available experimental data, i.e, the azimuthal torque coefficient as described in Section 3.2.3. Results of these simulations are included in Chapter 5.

With the gained understanding of the unsteady aerodynamics, thus the evaluation and improvement of the existing fast methods that are able to predict the torque coefficient of VAWTs under both regimes of operation are carried out following the next steps.

(iv) The dynamic stall Leishman-Beddoes is selected and evaluated by using the CFD simulations carried out in the step (i). This method is explained in Section 3.3 and more details of its performance and improvement are included in Chapter 6.

(v) The double multiple streamtube method is assessed in its accuracy to predict the torque coefficient at upstream and downstream of the rotor and also under the dynamic stall and the unsteady attached regimes. The results were included in Chapter 6.

(vi) A more in-depth analysis of the VAWTs aerodynamics has been performed by investigating the virtual incidence angle due to the curvature effects. This step uses the CFD simulations and it is assisted by a modifying the effective angle of attack into the Leishman-Beddoes model.

In the following section, the description of the methods used in this thesis are fully explained: The computational fluid dynamic techniques for the simulation using oscillating aerofoils and the CFD techniques for the VAWTs simulations; the Leishman-Beddoes model and, the Double multiple streamtube. A further discussion of the selection of these mentioned methods and their previous use in the reviewed literature to predict the VAWTs is also included.

3.2 Computational fluid dynamic simulations

This section describes the numerical techniques: (i) that have been used to investigated the stall-onset angle consisting of two-dimensional CFD simulations with an oscillating aerofoil describing the VAWT angle of attack and, (ii) the CFD numerical technique to investigate the VAWTs aerodynamics and its verification with experimental data.

3.2.1 Governing equations

Computational fluid dynamics (CFD) are based in the continuity, momentum and energy equations (the Navier-Stokes equations) to fully described the flow field around a body or system. For practical solution when the flow becomes turbulent, the instantaneous quantities are decomposed into a mean and fluctuating elements. These representations of the Navier-Stokes equations are called the Averaged Navier-Stokes equations (RANS) and for transient and incompressible flows (the cases investigated in this thesis) are represented by following expressions:

$$\rho(\frac{\partial U_i}{\partial t} + U_j \frac{\partial U_i}{\partial x_j}) = -\frac{\partial P}{\partial x_i} + \frac{\partial}{\partial x_j}(\mu \frac{\partial U_i}{\partial x_j} - \rho\overline{u_i' u_j'}) + \rho F_i \tag{3.1}$$

$$\frac{\partial U_i}{\partial x_i} = 0 \tag{3.2}$$

Eq.(3.1) represents the momentum equation and Eq.(3.2) represents the continuity equation. The decomposition of the instantaneous velocity adds new unknown variables into the momentum equation. The term, $(\rho\overline{u_i' u_j'})$ is known as the Reynolds stress (also called apparent stress) and its modelling is the purpose of the turbulence models.

The turbulence model solves a different number of transport equations to obtain the Reynolds stress tensor. Most of the available turbulence model in Fluent are base in the eddy viscosity concept and solves one, two, three or Four transport equations. The number of transport equations to solve increases the computational time of the simulations.

The Shear Stress Transport model, SST, uses the two-equation model $\kappa - \omega$ (turbulent kinetic energy-specific dissipation rate) to solve the flow within the boundary layer and the model $\kappa - \varepsilon$ (turbulent kinetic energy-turbulent dissipation rate) in the free-stream flow. This model is one of the most used in aerodynamic flows and takes into account within the turbulent viscosity the turbulent shear stress.

In order to predict the transition of the laminar to turbulent flow, the model Transitional SST has been proposed (also known as the $\gamma - Re_\theta$ transition model). This model is a further development of the SST model and solves two additional transport equations: for the intermittency, γ, and the momentum-thickness, Re_θ. A variation

of the Transitional SST is the intermittency model, γ transition, and it solves one transport equation for the turbulence intermittency γ, but ignores the solution of the momentum-thickness, Re_θ. This turbulent model, the intermittency transition model, reduces the computational effort by solving one transport equation instead of two and, can be applied for surfaces moving regarding a coordinate system.

The transport equation of the intermittency is given by following expression:

$$\frac{\partial(\rho\gamma)}{\partial t} + \frac{\partial(\rho U_j \gamma)}{\partial x_j}) = P_\gamma - E_\gamma + \frac{\partial}{\partial x_j}[(\mu + \frac{\mu_t}{\sigma_\gamma})\frac{\partial \gamma}{\partial x_j}] \tag{3.3}$$

the transition source terms, P_γ and E_γ are similar in formulation for the Transitional model. This model uses the same transport equation for ω than the SST model and the intermittency is only included in the production term of the κ transport equation as follows [89]:

$$\frac{\partial(\rho\kappa)}{\partial t} + \frac{\partial(\rho U_j \kappa)}{\partial x_j}) = \gamma_{eff} P_\kappa - D^*_\kappa + \frac{\partial}{\partial x_j}[(\mu + \frac{\mu_t}{\sigma_\kappa})\frac{\partial \kappa}{\partial x_j}] \tag{3.4}$$

where, $D^*_\kappa = min[max(\gamma_{eff}, 0.1), 0.1]D_\kappa$. D_κ is the destruction term and P_κ is the production term of the original SST model and γ_{eff} is the effective intermittency. The intermittency function, for a laminar flow, takes a value of 0 and a value of 1 for a fully turbulent flow. Observing the Eq.(3.4), while γ increases from zero to 1 within the boundary layer, the production term, P_κ, turns on and the eddy viscosity starts to increase [90]. Much more details of this model may be found in [89] and the Ansys Fluent guide user.

This Section 3.2.1 employs the symbols most widely used to represent the mathematical expression of the governing equations and more in-depth details are maybe found in [91]. Only for this Section 3.2.1, the variable P means pressure and F represents the external forces.

3.2.2 Simulations for oscillating simulations

This section presents the numerical settings and the verification carried out for the oscillating aerofoils simulations. The present two-dimensional CFD technique was carefully validated against experimental data. The available experimental data consists

of the normal force coefficient of an oscillating NACA0012 aerofoil with the Reynolds number 1.35×10^5 (chord-based), a chord (c) of 15 cm and a reduced frequency of 0.1 [4]. The intensity of the turbulence was 0.08%, similar to the experimental conditions of the wind tunnel test case. This experimental data is selected since VAWTs for urban environments can experience a Reynolds number as low as 1×10^5 [92, 93] and this is the main interest of this investigation. Also, several numerical investigations of this case have been performed in order to determine a numerical strategy that considers the mesh, time and domain independence for oscillating aerofoils at low Reynolds numbers [94, 68, 83, 69]

Numerical settings

In the present simulations, the turbulent transitional model $\kappa\omega - SST - \gamma$ was selected due to the Reynolds number being studied, namely $0.8 - 3.3 \times 10^5$, where the boundary layer flow transition is likely to occur and a transitional model is recommended at such Reynolds numbers [95, 96, 97]. A discussion of the influence of the turbulence models of this experimental case has been made in [97] and the use of a transitional model is recommended.

Among the pressure-based velocity coupling schemes available in Fluent: SIMPLE, SIMPLEC, PISO and Coupled, the first three used the segregated algorithm and Coupled uses the pressure-based coupled solver. The Coupled scheme uses an implicit time integration that is unconditionally stable regarding the time step. Despite that, since each time step requires a convergence criterion and hence several iterations to obtain this convergence, the non-linearities associated to the discretized equations may produce a large change in the quantities calculate at each iteration and produce slow convergence or divergence. To solve this, the coupled algorithm, introduces the under-relaxation factor, a, for the momentum and pressure variables to reduce the changes in these quantities during each iteration. The CFL number in the coupled algorithm, is a solution parameter and, in terms of under-relaxation factor is written as:

$$\frac{1-a}{a} = \frac{1}{CFL} \tag{3.5}$$

As consequence, large CFL numbers are possible to be employed for this implicit scheme and this can lead to faster convergence. This algorithm uses an algebraic multigrid method (AMG) that has the capabilities to detect divergence within an iteration, automatically reduces the CFL number. This coupled algorithm has demonstrated to be efficient with coarse time steps and coarse meshes. More in-depth detail may be found in the Fluent users guide and in [98]. Explicit time integration is only available for the density-based solver and the time step is restricted to the stability condition given by the Courant-Friedrichs-Lewy conditions with a suggested Courant number of 1.

The default CFL in the coupled algorithm is 200 but a reduction to 10-50 is recommended if there are difficulties with convergence, thus a CFL=10 was selected. A full convergence criterion with a relative residual less than 1×10^{-5} was used with 100 iterations per time step. At least four oscillating cycles were performed for each simulation before collecting the results, and in most cases, a convergence in the lift force coefficient was achieved after the second cycle. This agrees with the statistical convergence observed by Geng. et al. [97]. A second-order discretization (spatial and temporal) and a hybrid initialization was set up in all the simulations.

Mesh domain and boundary conditions

In the experimental data, a closed wind tunnel was used with the walls allocated to be three times the chord-length of the aerofoil from the centre of the pitching motion. Thus, to be consistent with the experimental test conditions, non-slip conditions were applied for the upper and lower bounds of the domain with an original distance of 3 times the chord-length. Moreover, due to the interest in studying aerofoils in an open environment, then the distance of the upper and lower boundaries from the pitching position of the aerofoils (1/4 c) was increased to 3, 10, 15 and 20 times the characteristic length, c, in order to find a domain with no influence on the forces on the aerofoil. The influence of this distance is observed in the resulting lift coefficient and very similar results were obtained using distances of 10, 15 and 20 c. Therefore, 15c was selected as the distance from the pitching point to the boundaries (lower and upper), and this was enough to avoid the influence of the upper and lower boundaries. The pressure outlet

was set to be $45c$ from the pitching point of the oscillating aerofoil, and the velocity inlet was set to be $15c$ from the oscillating point. Both distances are considered to be large enough to allow the development of the wake and within the recommendations of several investigations [94, 69].

The aerofoil profile was set as non-slip conditions and due to the importance of solving the viscous layer, then 60 layers were collocated around the aerofoil and the y+ in the boundary layer was less than 1.2.

In the mesh topology, two domains were used: a rotating domain with an unstructured mesh as illustrated in Fig 3.2(a), and a stationary domain consisting of a structured mesh, Fig. 3.2(b). The interface between the rotating zone (denoted with triangles) and the stationary domain (quadrilaterals) is shown in Fig.3.2 (c). In order to reduce the interpolation error during the motion, both domains contain in the interface the same number of nodes, thus the element size in the contact region was of the same length. For the rotating zone, a hard face sizing method was used and at the contact interface for both domains, the stationary and the rotating domains, a hard edge sizing method was used. This guarantees the very similar size elements in the interface zone, that reduces the interpolation error, and also agrees with the user guide in Fluent and other reported strategies of meshing at the interface zone [51].

A mesh independence analysis with four grids with the parameters as given in Table 3.1 was performed. The number of nodes around the aerofoil investigated was 500, 1000, 2000 and 4000; however, no large impact was found in the force coefficients observed in Fig. 3.3(a) within this range of nodes, and therefore 1000 nodes were selected for the final settings.

Table 3.1: Characteristics of the evaluated meshes for CFD technique employed for the oscillating aerofoils.

Parameter	G1	G2	G3	G4
Nodes on aerofoil	500	1000	2000	4000
Total mesh elements	140000	200000	300000	500000

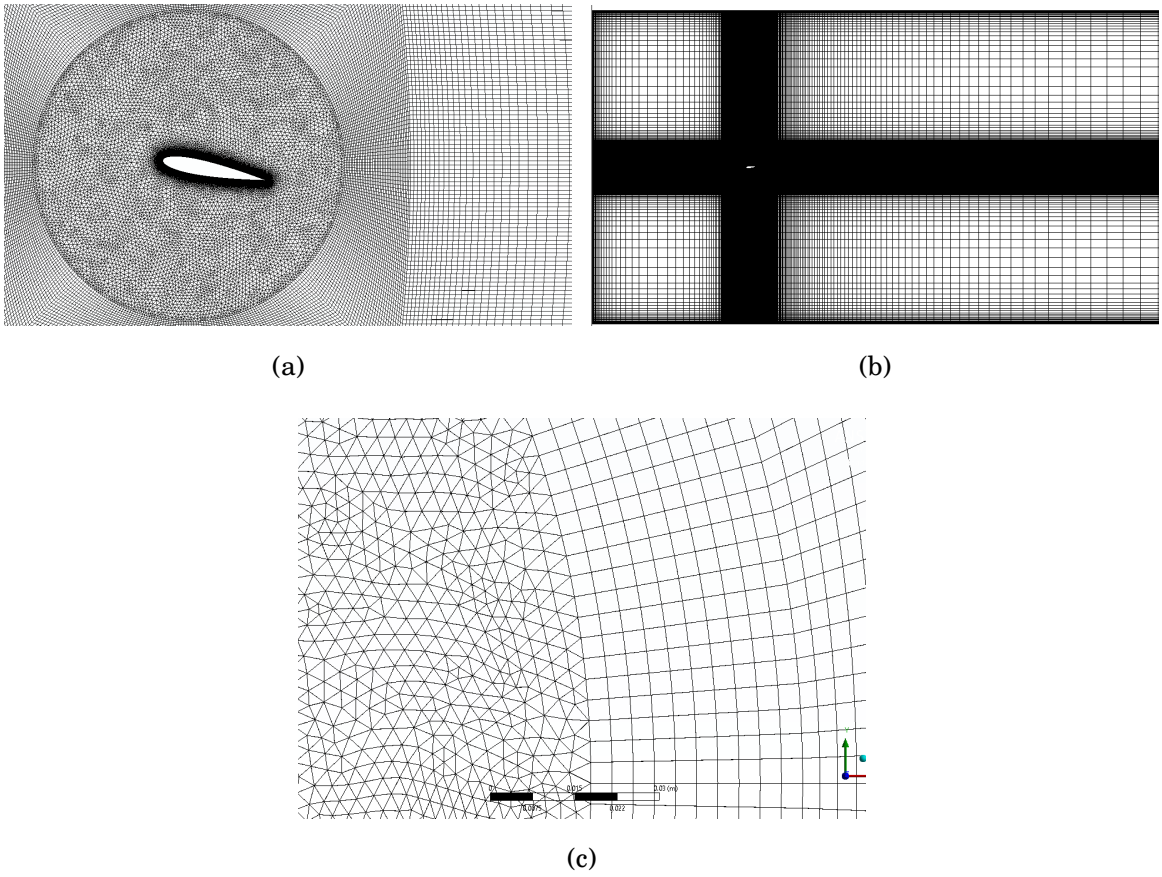

(a) (b)

(c)

Figure 3.2: Mesh topology for the CFD technique applied to the oscillating aerofoil. (a) The rotating region with an aerofoil with 1000 nodes along its surface, (b) the stationary domain and, (c) the interface between the rotating and the stationary domain zones.

Time step analysis

A time step independence study was conducted with a non-dimensional time constant ($\tau = t/T$) of 0.001, 0.0005 and 0.00025. These time steps correspond to a step increment of 0.1, 0.05 and 0.025 degrees in the angle of attack, respectively. Similar results were obtained for the lift force coefficient, as observed in Fig. 3.3(b), for all the time steps studied and therefore, $\tau = 0.0005$ was selected.

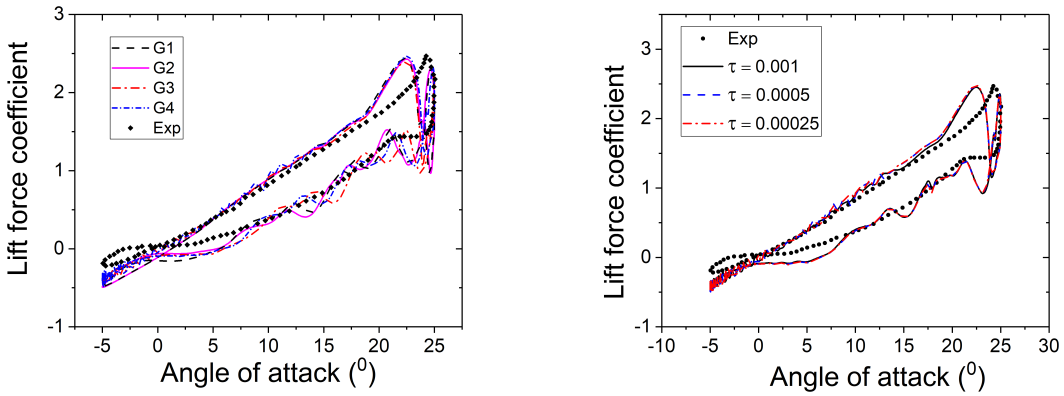

Figure 3.3: (a) Mesh independence study, and (b) time step independence study for the CFD simulation of an oscillating NACA 0012 aerofoil.

Numerical verification

The present URANS simulations were validated against the URANS simulation performed by Geng et al. [69], and two Large Eddy Simulations (LES) carried out by Geng et al. [69] and Kim et al. [68], and a comparison among these four simulations is shown in Fig. 3.4(a). Very good agreement in the prediction of the lift force coefficient, C_L, was observed among both 2D CFD simulations and the LES simulations. For all the numerical simulations, 2D CFD and LES, the linear region of variation of the lift force coefficient with angle of attack is in very good agreement with the experimental data. Further, the deviation in C_L appears once the vortex has been released and it can be concluded that the stall-onset angle may be predicted with the same accuracy for all the numerical techniques compared in Fig. 3.4 (a). Unfortunately, a significant C_L peak was observed in the experimental data and this is not captured by any of the numerical simulations. Since this peak indicates that a vortex is located at the mid-chord of the aerofoil, thus, the accuracy in predicting the stall-onset angle is not affected.

Further, to demonstrate the accuracy of the present numerical methodology to capture the stall-onset angle, a second validation is performed by using the experimental data in [5] consisting of a NACA0015 aerofoil that describes the same motion as the

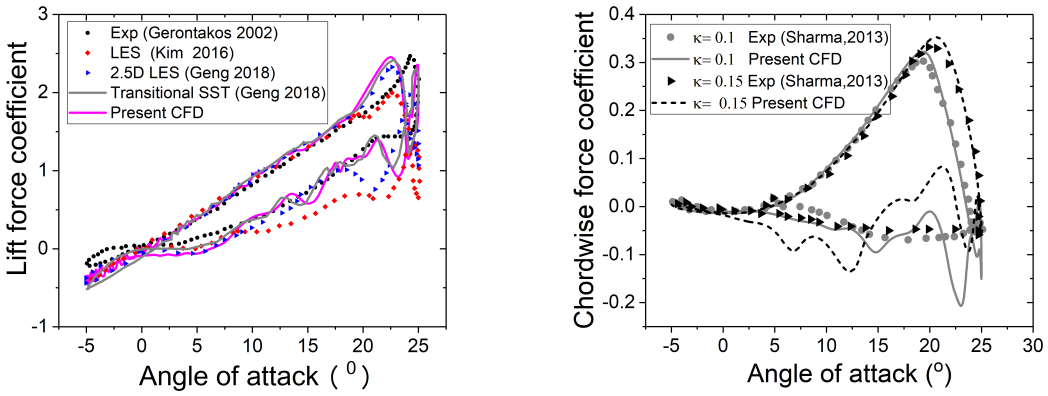

(a) (b)

Figure 3.4: (a) The lift coefficient as a function of the angle of attack of the oscillating aerofoil NACA0012 at Re 1.35×10^5 predicted with the present CFD technique and the comparison with the experimental data [4]. (b) Chordwise force coefficient of the oscillating NACA0015 as a function of the angle of attack predicted with the present CFD technique and compared with experimental data with the same characteristics at Re 2×10^5 [5].

previous experimental case, i.e. $\alpha(t) = 10 + 15 \sin \omega t$ at Re 2×10^5. The advantage of this second case is the available data of the chordwise force coefficient. The numerical predictions of the stall-onset angle are obtained for the reduced frequency values of $\kappa = 0.1$ and $\kappa = 0.15$ and these are included in Fig. 3.4 (b). Excellent agreement was observed in the prediction of the peak in the chordwise force coefficient. Hence, the present numerical simulations, since they capture with an excellent agreement the chordwise force coefficient with the experimental data are considered accurate enough to investigate the stall-onset angle.

Static simulation

Due to the interest in evaluating the static stall angle for three Reynolds numbers, namely, 0.8, 2 and 3.3 $\times 10^5$, static simulations were performed by using the same mesh characteristics as those employed in the unsteady simulations. The number of iterations used was 10000 to ensure a full stabilization of the lift force coefficient and

then, the static stall angle obtained for the NACA0015 aerofoil was: 10°, 13°, 14° for the Reynolds numbers 0.8, 2 and 3.3 $\times 10^5$, respectively. The Reynolds number was changed by varying the incoming flow to 8, 20 and 33 m/s. Same static CFD numerical technique was applied later for the NACA0018 and NACA0021 at the corresponding Reynolds number investigated in Table 6.1.

3.2.3 CFD technique for VAWT simulations

This section describes the numerical strategy adopted for the CFD simulations of the VAWTs performed in Chapter 5. It includes the numerical settings, the domain, mesh and time step independency analysis. Moreover, this section includes the verification of the proposed-final numerical settings with experimental data.

Introduction

Among the different techniques to investigate the VAWTs aerodynamics namely, the experimental tests, Large-eddy simulations and URANS CFD simulations, the last is the most suitable for the objectives of this thesis. URANS computational fluid dynamics has become the technique used most extensively to investigate the aerodynamics of VAWTs in the last few years. Thus, the literature dedicated to the numerical strategy to perform the CFD simulation of VAWTs is extensive [63, 99, 100]. In summary, the numerical strategies presented in previous investigations take into account the influence of several parameters such as: the time step, the number of elements around the aerofoil, the most appropriate turbulence model, the number of revolutions to obtain convergence in the torque coefficient, the domain dimensions, the number of blades etc.

Despite the several numerical strategies found in the literature, this section attempts to cover a gap in the literature that has not been observed before. It analysis the capabilities of the two-dimensional CFD simulations to predict accurately the upstream and downstream torque coefficient of a VAWT. Experimental torque coefficient for a two-bladed VAWT has been employed and three different tip speed ratios (TSRs) have been verified. At a tip speed ratio (TSR) located in the dynamic stall region of a

VAWT curve performance, a TSR located at the optimum torque coefficient and, a TSR under a fully attached flow regime.

Description of the experimental VAWT data

The available experimental data in [31] contain the azimuthal torque coefficient as a function of the azimuthal angle, $C_Q(\theta)$ for the VAWT with the characteristics included in Table 3.2. This data was obtained by using the pressure coefficient measured by 32 pressure taps located at the mid-span of the straight blade with the NACA0021 aerofoil. A total of 10 000 samples were collected at three different tip speed ratios with a sampling frequency of 1250 Hz, thus the pressure coefficient data were averaged and used to calculate the torque coefficient at each 5° azimuthal angle during one cycle, i.e. one wind turbine revolution.

Table 3.2: Geometrical characteristics of the VAWT used as a reference case for the CFD verifications.

N_b	2	Aerofoil	NACA0021
R	1 m	H	1.2 m
D_s	0.216 m	c	0.265m
β	6°	U_∞	8 m/s

The explained experimental data in [31] allows a comparison with the two dimensional CFD simulations since the pressure coefficient at the mid-span has only a minor influence of the 3D effects regarding the torque-meter data that include all the tip losses. As mentioned in the introduction, most of the CFD simulations of VAWTs have relied on the average power coefficient and here, the azimuthal torque coefficient at different TSRs are used since they allow much more insight into the performance of the CFD simulations. The three tested TSRs were, one low TSR, 1.38, where the turbine exhibits low performance and dynamic stall. Secondly, at the optimum TSR 2.19 and one at a high TSR of 2.58 where the power coefficient decreases again and usually the blades are far away from the dynamic stall condition.

From the CFD simulations, the torque coefficient as a function of the azimuthal angle, $C_Q(\theta)$ is obtained following next expression:

$$C_Q(\theta) = \frac{Q(\theta)}{0.5\rho D V_\infty^2 R} \tag{3.6}$$

where $Q(\theta)$ represent the blade momentum from the rotation centre of the blades and this is obtained using the monitor tools during the set-up of the solution.

Numerical Settings

For the present CFD simulations, the turbulent model selected was the γ transitional, i.e, the $\kappa - \omega$ SST with intermittency. A transitional model was selected since the accurate prediction of the pressure due to the presence of the laminar separated bubble (LSB) near the leading edge of the aerofoil is critical in capturing better the inception of the dynamic stall phenomenon [95, 101] and the dynamic stall is likely to occur in VAWTs at low TSRs. The importance of using a transitional model to better predict the stall inception has been addressed by Ekaterinares and Platzer [95] and a transitional turbulence model has been also recommended for the investigation of VAWTs in [102].

The CFD simulations were performed by using the commercial software Ansys Fluent 17.2. A pressure-based solver was selected as the solution method with a Coupled scheme. Some of the advantages of the coupled algorithm are its ability to automatically decrease the Courant Number if divergence is detected within a time step and, its fast convergence when employing a coarse mesh and coarse time steps [62]. A CFL of 10 and a full criterion for convergence of 1×10^{-5} with 100 iterations per time step were selected. Also, a total of 20 revolutions were performed for all the simulations as recommended in recent guidelines for VAWT simulations [62, 102]. A second-order discretization (temporal and spatial) and hybrid initialization was set-up for all the simulations. The fluid selected was the air with a density of 1.225 kg/m^3.

Mesh domain and boundary conditions

The computational domain is schematically presented in Fig.3.5, and it consists of two zones: one rotating zone and one stationary zone with an unstructured and structured

mesh, respectively. The rotating zone was moved using the mesh motion condition and by varying the rotational velocity accordingly to next expression:

$$\omega = \frac{\lambda V_\infty}{R} \tag{3.7}$$

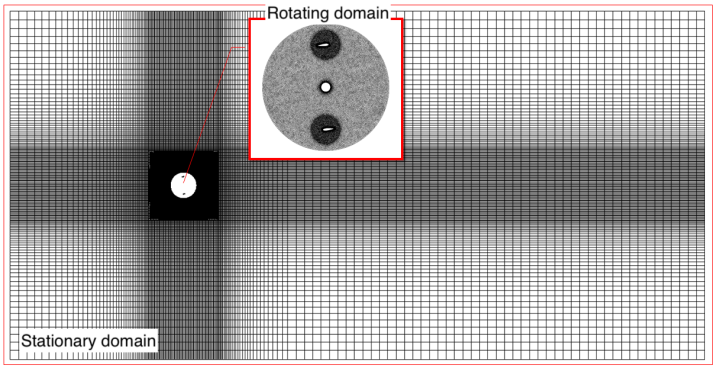

Figure 3.5: Mesh topology of the stationary and the rotating grid zones used in the VAWT simulations.

The boundary conditions were defined as a velocity inlet, pressure outlet and symmetry for the upper and lower boundaries as indicated in Fig.3.6. The aerofoils, which represent the blades, were considered as non-slip boundary conditions.

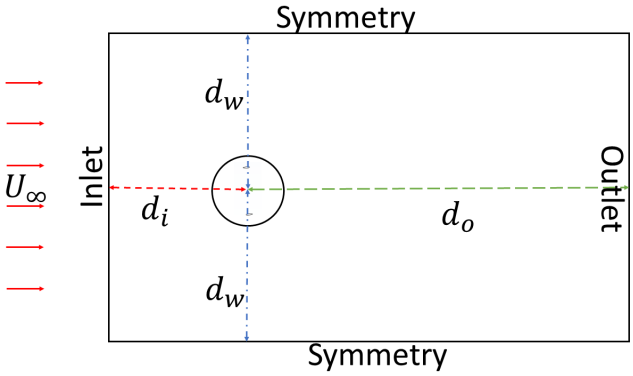

Figure 3.6: Schematic representation of the CFD domain used for the VAWTs simulations (not scale) and the boundary conditions.

In order to define the distance from the inlet to the turbine centre, d_i, the extent

of the upper and lower symmetry boundaries from the turbine centre, d_w and then an independence analysis was performed with the d_i and d_o values of 5, 7.5, 10 and 20 diameters as indicated in Fig. 3.7. 10 times the diameter, 10D, was considered to be far enough away to avoid the blockage effect and minimize any effect on the power coefficient. The distance from the turbine centre to the outlet, d_o, was maintained at a value of 30 times the diameter, and this is within the recommended value to ensure good development of the wake that is independent of the TSR and the solidity. These values are within the recommended values in the guidelines for CFD simulations of VAWTs [62, 102].

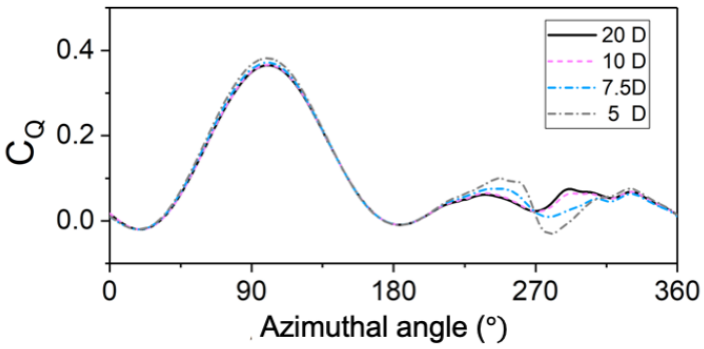

Figure 3.7: Influence of the upper and lower domain boundaries in the torque coefficient predicted at the 20th cycle for a $\lambda = 2.19$.

A mesh independence analysis for the tip speed ratio of 2.19 was carried out in order to determine the optimum number of elements around the aerofoil. The number of elements of each mesh evaluated are included in Table 3.3. The prediction of the torque coefficient as a function of azimuthal angle in the 20th revolution using these different grids is included in Fig. 3.8. For this tip speed ratio of 2.19, the Mesh1 produces a $y^+ < 2.2$; the Mesh2 a $y^+ < 1$ and the Mesh3 a $y^+ < 0.5$. The analysis shows a negligible influence of the mesh in the prediction of the azimuthal torque coefficient. The current results agree with Rezaeiha et al. [6] investigation, where three grids with the y^+ as indicated in Fig. 3.9 for a two-bladed VAWT at a tip speed ratio of 4.5 were tested and the torque coefficient was very similar for all the grids. The negligible

influence of the mesh in the present CFD simulations is attributed to the fact that the γ transition model predicts similar results as long as the y^+ is lower than 5 accordingly the Fluent user guide.

Table 3.3: Characteristics of the evaluated meshes for the CFD technique employed for the VAWT simulations.

Parameter	Mesh1	Mesh2	Mesh3
Nodes on aerofoil	500	1000	2000
Total mesh elements	140000	230000	550000

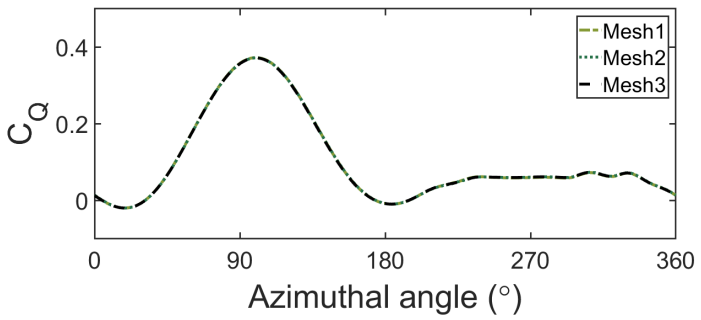

Figure 3.8: Torque coefficient as a function of the azimuthal angle predicted with the different grids presented in Table 3.3 in the 20th revolution and a tip speed ratio of $\lambda = 2.19$. An azimuthal increment of $0.25°$ was employed.

To carried out the further CFD simulations for the VAWTs, the Mesh2 with 1000 elements around the aerofoils was selected. The most important factor for the selection of the mesh was the computational time: Mesh 1 requires 22:15:10 CPU hours; Mesh2 requires 25:44:55 CPU hours and, Mesh 3 54:00:26 hours. Therefore, the Mesh2 results in the most convenient mesh to be used for further simulations to be performed in Chapter 5. The number of elements around the aerofoils is within the range recommended in [62].

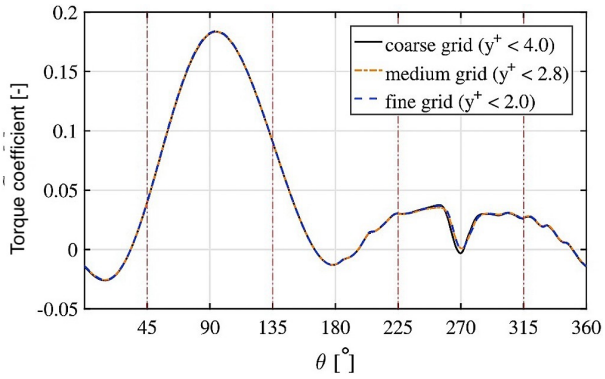

Figure 3.9: Prediction of the instantaneous torque coefficient in [6] for the last revolution versus azimuth angle for different grids in last revolution for a tip speed ratio of $\lambda = 4.5$.

Time independence analysis

In this section, a time independence analysis was performed in terms of the azimuthal angle step, $\Delta\theta$. The time step, Δt, is related with the azimuthal angle by the next expression:

$$\omega = \frac{\Delta\theta}{\Delta t} \tag{3.8}$$

Since the rotational speed, ω, depends on the tip speed ratio according to Eq. 3.7, then, it affects the time step value and thus, the azimuthal increment is more representative parameter to perform the time step analysis.

Figure 3.10 presents the prediction of the torque coefficient using four azimuthal angles increment: 0.05, 0.1, 0.25 and 0.5°. The case analyzed correspond to a two-bladed VAWT at a tip speed ratio of 2.19. It is observed that the difference in the torque coefficient is almost negligible among the four azimuthal increments. Therefore, a time step corresponding to an azimuthal increment of 0.25° was selected for all the simulations and this value is within the recommendations in several investigations [62, 103] where the impact of the tip speed ratio and the number is blades in the selection of the azimuthal increment was analyzed.

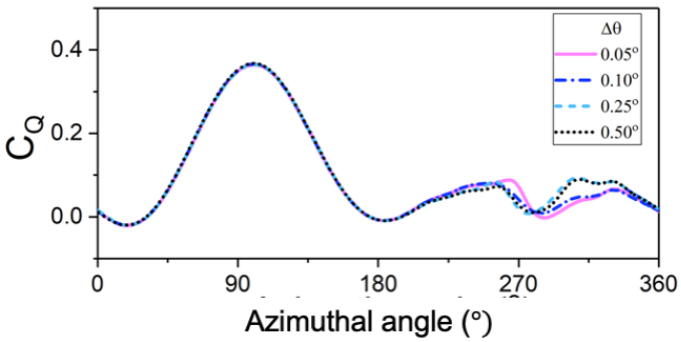

Figure 3.10: Torque coefficient as a function of the azimuthal angle predicted with different time steps at the 20th cycle. The tip speed ratio is $\lambda = 2.19$ and the Mesh2 with 1000 element around the blades was employed.

Effectiveness of the numerical simulations

The numerical settings, the mesh and the azimuthal increment selected in previous sections have been verified with the experimental VAWT described in Table 3.2 for three tip speed ratios. The tip speed ratios investigated were 2.58, 2.19 and 1.38.

The results have revealed that for high TSR of 2.58, the present CFD simulations can capture, with a very good agreement, both the contribution of the torque coefficient in the upstream and downstream regions of the rotor, see Fig. Fig. 3.11(a). The average torque coefficient predicted by the CFD simulations was 0.16 and this value is in very good agreement with the experimental value of 0.17. Similar results were found with the prediction at the optimum TSR 2.19, see Fig. 3.11(b), and the average torque coefficient of 0.18 was obtained with the CFD simulation and this is in very good agreement to the value of 0.19 for the experimental data.

For the very low TSR of 1.38, vortex shedding was observed upstream of the rotor and these vortexes were released downstream of the rotor. The multiple vortex shedding is observed in Fig. 3.12(c) and additionally to the vortex formed on the blade, the shaft also produced vortex formation released at downstream of the rotor. The upstream contribution of the torque coefficient at this low tip speed ratio was predicted with good agreement, nevertheless, the downstream instantaneous torque coefficient

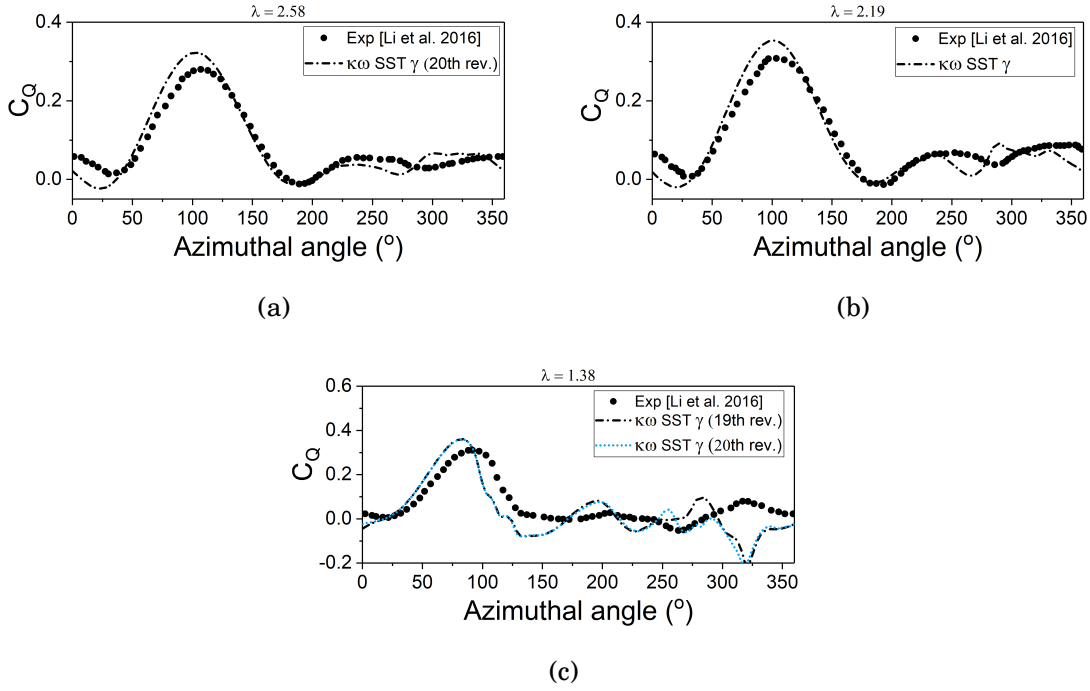

Figure 3.11: Prediction of the instantaneous torque coefficient at the 20th revolution for (a) TSR 2.58, (b) TSR 2.19 and, (c) TSR 1.38 for a two-bladed VAWT.

oscillates in value during all the revolutions, see for example the revolution numbers 19 and 20 in Fig. 3.11(c). This oscillation was attributed to two main effects; namely, the blade interaction with its detached separated vortex at the leading edge of the aerofoil and the vortices formed by the shaft (with $D = 216$ mm) that were fluctuating in the direction related to the Von Karman effect. Thus, when the wind turbine blade passes $\theta = 270°$, behind the shaft, in some revolutions the blade interacts with the vortex that is generated by the shaft and then the torque coefficient is reduced as indicated in Fig. 3.11(c) in the 20th cycle. The experimental average torque coefficient at TSR=1.38 was predicted to be 0.12 and with the CFD predicts oscillations in the range 0.076-0.107.

For the tip speed ratios of 2.58 and 2.19, Fig. 3.12(a-b), the influence of the vortex shedding due to the shaft in the torque coefficient at downstream was minimal. Additionally, in practical situations, the diameter of the shaft is smaller, thus the shaft is not considered in the subsequence simulations. Twenty revolutions were employed in

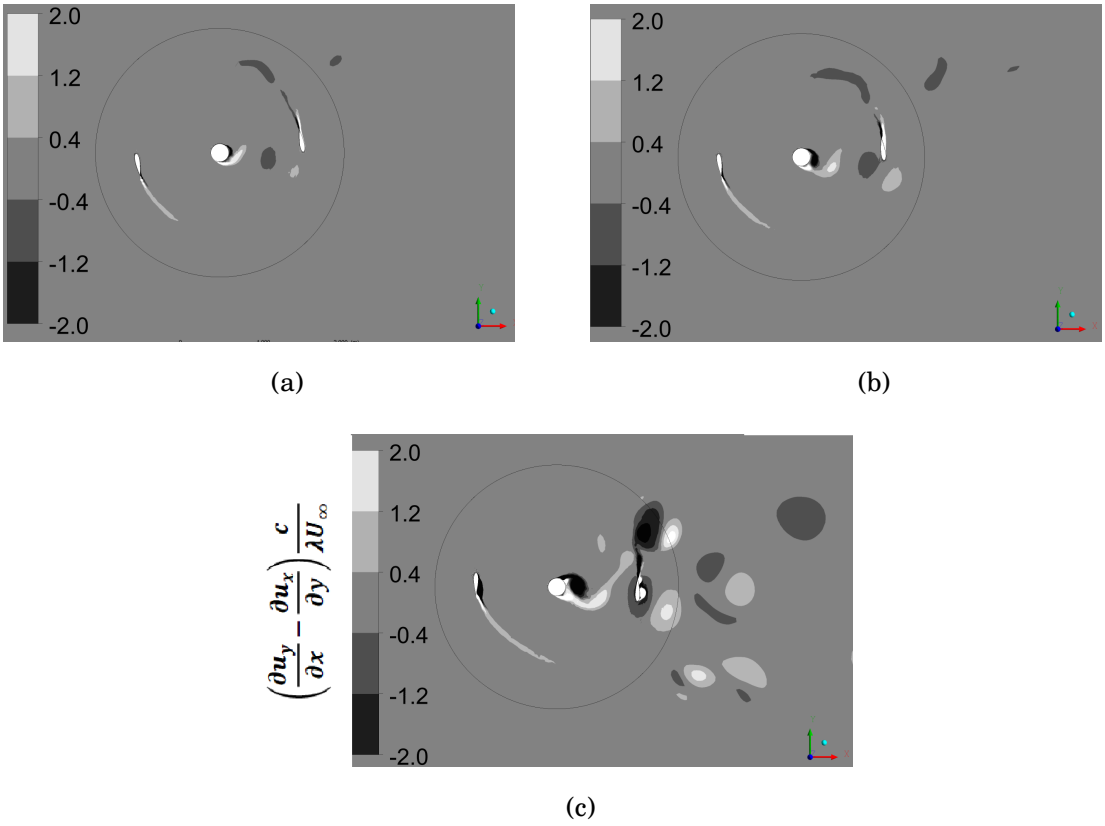

Figure 3.12: Vorticity contours for a two-bladed VAWTs at (a) λ= 2.58, (b) λ= 2.19 and, (c) $\lambda = 1.38$

order to secure the convergence of the torque coefficient, and this is the recommended value given in [103].

3.3 Dynamic stall method

The dynamic stall behaviour depends on several parameters. The most studied are as follows: the reduced frequency, the amplitude of the oscillation, mean angle of oscillation, Reynolds number, Mach number, pattern of the angle of attack, and the aerofoil shape. Due to all these parameters, reproducing the unsteady forces accurately represents a significant challenge for the dynamic stall models. Among the several existing dynamic stall models, one of the most used dynamic stall algorithms is the Leishman-Beddoes (LB) model. This model considers most of the physical aspect of the dynamic

stall phenomenon described in Section 2.2.2

The objective of the LB dynamic stall model is to compute the normal (C_N) and the chordwise force coefficient (C_C) over an aerofoil undergoing unsteady conditions. To compute such forces the original LB modules represented in Fig. 3.13. The full algorithm of this original LB dynamic stall is included in Section A and a summary is described as following:

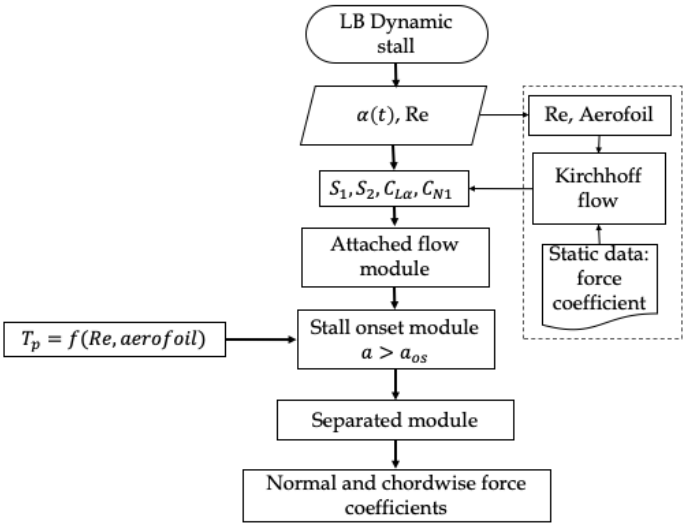

Figure 3.13: Schematic representation of the Leishman-Beddoes algorithm.

- A fully unsteady attached flow regime. Within this module of the LB algorithm, the time lag in the force responses are computed using the Equation included in Section A.1. To compute the unsteady forces under a full attached regime the most substantial parameter is the the slope of the lift force coefficient under static conditions, $C_{L\alpha}$ and obtained as described in Section 6.2.2.

- The stall-onset module is able to predict the instance when the leading edge (LE) pressure collapse and the vortex is shedded downstream from the LE towards the trailing edge of the aerofoil. To compute this lag in the pressure response a series of deficiency functions are applied to the normal force coefficient as described in Section A.2 and also analysed in Section 6.2.2

- The unsteady separated flow. This module is able to compute the non-linear unsteady forces due to the vortex movement downstream along the aerofoil surface as well as the loads due to the trailing edge separation. See more details in Section A.3

The Leishman-Beddoes dynamic stall model has been widely tested to predict the unsteady forces for oscillating aerofoils at Reynolds number larger than one million. It requires the history of the angle of attack, $\alpha(t)$ and the Reynolds number as the main first initial input. Immediately, the algorithm calls for the parameters S_1, S_2, $C_{L\alpha}$, α_1, C_{N1} which are empirical parameters obtained by applying the Kirchhoff flow equation to the static force coefficients data from a specific aerofoil and Reynolds number. These parameters are crucial to predict accurately the unsteady forces under the dynamic stall and fully attached regimes. Since most of the existing investigations have focused on Reynolds larger as one million, then, there is an urgent need of assessing the pertinence of the Kirchhoff flow model at lower Reynolds number. Therefore, this Kirchhoff flow model is analysed in detail in Chapter 6.

Among the three modules of the LB-algorithm, the most critical one is the stall-onset module. This module requires to predict the delay in the stall angle and, in order to accurately predict this point, requires of a time delay constant T_p, that represent the lag in the pressure coefficient regarding the static conditions. Two major issues are found within this point: (i) stall-onset angle remains unclear for the VAWTs and this is addressed in Chapter 4 and, (ii) the time delay constant requires for the LB-algorithm remains unclear and very little studied at the Reynolds numbers of interest lower than one million. Therefore, the time delays constants and the assessment of the LB dynamic stall at low Reynolds number is carried out in Chapter 6.

3.4 Double multiple streamtube theory

Due to the role that wind turbine technology plays now in the production of electricity and the need to improve the designs in order to increase the power generation, several attempts have been made to develop an aerodynamic model that is capable of predicting the power coefficient of a VAWT [104, 105]. One of the most used models is the

Double Multiple Streamtube Theory (DMST) proposed by Parashivoiu [2]. This method takes into account the geometry of the wind turbine and others secondary effects, such as the streamtube expansion, when computing the power coefficient. This author validated his method with few wind turbines that used two or three blades and TSRs with a value larger than two. The dynamic stall models, such as Gormont, MIT and indicial methods, were included in the analysis and a good agreement with the cases evaluated was found. Other authors have used the DMST combined with dynamic stall models in order to take into account the unsteady aerodynamics [53, 106, 107] and among the tested models the Leishman-Beddoes (LB) has demonstrated a better response when computing the normal and tangential forces. Due to the early limitations in the available experimental data, the validations were restricted to only a few cases, and the influence of the dynamic stall over the power coefficient for conditions of low TSRs is still not well understood.

The original DMST method proposed by Parashivoiu analyses the unsteady loads of the rotor by dividing the rotor in N_{th} number of elements and proposed the interference factors for both section of the rotor: at upstream and downstream of the rotor.

The expression to estimated the interference factor at upstream of the rotor, u takes into account the geometry of the rotor and some secondary effects and is calculated by follows:

$$u(\theta) = KK_0\eta/[KK_0\eta + \int_{\theta-\frac{\Delta\theta}{2}}^{\theta+\frac{\Delta\theta}{2}} f(\theta)d\theta] \tag{3.9}$$

where K is the geometrical parameter of the rotor, $K_0 = \sin(\theta + \Delta\theta/2) - \sin(\theta - \Delta\theta/2)$ and the function $f(\theta)$ is given by next equation:

$$f(\theta) = \frac{V_{rel}}{V_\infty}[C_R\cos(\theta) + C_T\sin(\theta)] \tag{3.10}$$

The interference factor for the upstream section, u, is calculated iteratively at each i element and when convergence is reached, this value is used as an input to estimated the interference factor at downstream zone of the rotor, u'. The radial force coefficient, $C_R(\theta)$ and the tangential force coefficient $C_T(\theta)$ are obtained using the static values of the lift and drag forces.

The theoretical equations of the relative velocity, Eq.(2.1) and the angle of attack,

Eq.(2.2) introduces the interference factor by using the following expressions:

$$V_{rel}(\theta) = V(1 + 2X_r \cos(\theta) + X_r^2)^{1/2} \tag{3.11}$$

where, the local tip speed ratio $X_r = \omega R/V$ and V is called the induced velocity and is given by:

$$V = u/V_\infty \tag{3.12}$$

The path angle including the interference factor reads:

$$\phi(\theta) = \arctan(\frac{\sin(\theta)}{X_r + \cos(\theta)}) \tag{3.13}$$

and the angle of attack is estimated by using Eq.(2.2). Equations (3.11-3.13) applies similarly to the downstream section. More details maybe found in [108].

Finally, the torque coefficient at each azimuthal angle is predicted as follows:

$$C_Q(\theta) = (C_L \sin(\phi) - C_D \sin(\phi)) \frac{2c}{R} \left(\frac{V_{rel}}{V_\infty} \right)^2 \tag{3.14}$$

The upstream ($C_{Q,up}$) and dowsntream ($C_{Q,dw}$) torque contributions were calculating following the expressions:

$$C_{Q,up} = \frac{N_b}{2\pi} \int_0^\pi C_Q(\theta) d\theta \tag{3.15}$$

$$C_{Q,dw} = \frac{N_b}{2\pi} \int_\pi^{2\pi} C_Q(\theta) d\theta \tag{3.16}$$

where, N_b represents the number of blades.

The total torque coefficient results in the expression:

$$C_{Q,T} = C_{Q,up} + C_{Q,dw} \tag{3.17}$$

The torque coefficient produced by the blades, is the tangential force, F_T times the radius, by using the definition of moment, where a moment is represented by $M = rxF$. In the vertical axis wind turbines, the tangential force is calculated by:

$$F_T = F_L sin(\phi) - F_D cos(\phi) \tag{3.18}$$

where F_L and F_D represent the lift and drag forces on the blades. In the investigated cases where, $\beta = 0^\circ$ and the path angle results in $\phi = \alpha$. Therefore, dividing F_T by the actual V_{rel} kinetic energy, a tangential force coefficient is given by:

$$C_T = C_L \sin(\alpha) - C_D \cos(\alpha) \tag{3.19}$$

3.5 Summary

This Chapter has described the methodology followed in the thesis to understand the aerodynamics in the VAWTs in order to bridge the gaps found in the literature as described in Chapter 2. The methods that have been employed along the Chapters are described and consisting of: two-dimensional CFD simulations for oscillating aerofoils; two-dimensional CFD simulations for VAWTs; the dynamic stall Leishman-Beddoes algorithm and, the double multiple streamtube model.

Some of the important outcomes in the present Chapter are described as follows:

(i) A verified CFD technique that is accurate enough to compute the stall-onset angle is described. The CFD numerical techniques agree with the available data for two oscillatory aerofoils, the NACA0012 and the NACA0015 at low Reynolds number, 1.35×10^5 and 2.0×10^5 respectively. These good results provide the confidence to investigate in detail the stall-onset angle in Chapter 4.

(ii) The CFD numerical technique for the VAWTs is described as well as the available data to verify this numerical technique. The description of the six aerofoils under investigation, namely, the NACA0021, NACA0018, NACA0015, NACA0012 and the cambered S1210 and NACA2418 is included.

(iii) The effectiveness analysis of the CFD simulations has demonstrated that the current CFD simulations are able to predict accurately both the upstream and downstream aerodynamics of the VAWTs.

(iv) The Leishman-Beddoes model has been identified as the most pertinent dynamic stall model to predict the unsteady loads for the VAWTs. Its algorithm has been explained and the critical sections of this algorithm that requires a more in-depth discussion to be applied in the prediction of the unsteady loads of VAWTs are defined: the

time-delay constant to predict the stall-onset at Reynolds number lower than one million and the assessment of Kirchhoff flow model to predict the obtained the empirical parameters from a specific aerofoil. These two critical points are further discussed in Chapter 6.

(v) The double multiple stream-tube has been identified as the most used fast tool to predict the VAWTs performance but still need an assessment of its capabilities to predict the upstream and downstream torque contribution under the full-unsteady attached regime. A further discussion is included in Chapter 7.

Chapter 4

The stall onset angle

4.1 Overview

The stall-onset is the most critical parameter to describe the development of the dynamic stall; it marks the inception of the vortex at leading of the aerofoil. In the VAWTs, this parameter has been very little evaluated as explained in Section 2.2.2 and, the effect of the relative velocity, pitch angle, the tip speed ratio, rotational speed and Reynolds number remains unclear. This chapter presents the analysis of the several operating parameters that dictate the final value of the stall-onset angle. Additionally, the range of Reynolds number investigated, $0.8 - 3.3 \times 10^5$, has not been previously studied and this range of Re are very important for the understanding of the dynamic stall phenomenon of VAWTs operating at low wind speeds.

4.2 Methodology

The two-dimensional CFD numerical technique for an oscillating aerofoil explained in Section 3.2.2 was used in this Chapter. The present simulations agree very well with the experimental data employed. In order to evaluate the effect of the operating conditions on the stall-onset angle, then two approaches were used.

First, an incoming wind flow U with a constant magnitude (depending on the chord-based Reynolds number under evaluation) past an oscillating aerofoil, as illustrated in Fig. 4.1. The oscillating aerofoil describes a motion with the angle of attack $\alpha(t)$ for a VAWTs given by Eq.(2.2) [2]. For this oscillating aerofoil β positive is indicated in Fig. 4.1. The angle of attack represents the angle between the aerofoil-chord and the incoming wind flow U aligned all the time to the x-axis.

The value of ωt from 0 to π represents the upstream zone of the rotor, and from π

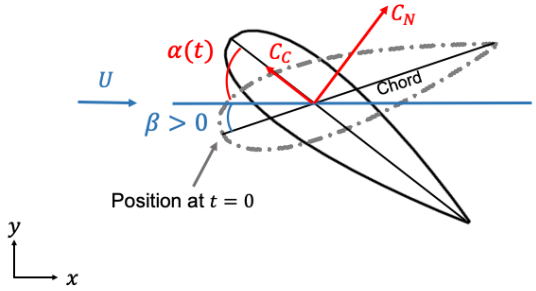

Figure 4.1: Sketch of an oscillating aerofoil with the VAWT angle of attack $\alpha(t)$ and an incoming flow (U). U can take a constant magnitude or a time-varying magnitude given by the relative velocity equation.

to 2π the downstream zone. Positive angles of attack are associated with the upstream zone of the rotor and negative angles with the downstream zone.

In order to replicate the angle of attack motion given by Eq. (2.2) in the CFD simulations, a user defined function (UDF) was employed to control the pitching rate of the rotating mesh domain (mesh domain explained in Section 3.2.2) according to the equation:

$$\dot{\alpha}(t) = \omega \frac{(1+\lambda\cos(\omega t))}{(1+2\lambda\cos(\omega t)+\lambda^2)} \tag{4.1}$$

(i) Using this first approach, at a constant Reynolds number, the influence of the tip speed ratio (λ), pitch angle (β) and the angular velocity (ω) on the stall-onset angle were investigated. The rotational speed for these oscillating aerofoils was expressed in terms of the non-dimensional parameter called the reduced frequency (κ), as $\omega = 2\kappa U_{ref}/c$. U_{ref} represents the actual wind speed that impacts the aerofoil. This analysis was performed for a Reynolds number base on the chord of 2×10^5. The chord length was 0.15 cm and the constant incoming wind flow had a magnitude $U_{ref} = 20\ m/s$.

The CFD simulations performed for the oscillating aerofoils and the variables used in each case investigated at a constant Reynolds number are included in Table 4.1.

Table 4.1 indicates, for example for cases 1 and 2, the same tip speed ratio and pitch angle were used in the simulation and it only changes the reduced frequency, allowing

then, the observation of the reduced frequency influence in the stall-onset angle. Also, the cases 10 and 11 have the same tip speed ratio and pitch angle. Similarly, to investigate the influence of the tip speed ratio, cases 3, 4 and 7 keep constant the values of the reduced frequency and the pitch angle, as a consequence, the influence of the tip speed ratio was able to be analysed. Finally, the cases 5-9 maintain the same reduced frequency and tip speed ratio, thus the influence of the pitch angle was observed with these simulations. Results are presented in the following paragraphs.

Table 4.1: The values of κ, λ, β used in the CFD simulations of the oscillating aerofoils at the Re 2×10^5. The predicted stall-onset angle, α_{os} explained in Section 4.2.1 is also included.

Simulation	κ	λ	β	α_{os} (°)
Case1	0.02	3	-11	14.700
Case 2	0.04	3	-11	16.230
Case 3	0.06	3	0	16.560
Case 4	0.06	2.37	0	17.681
Case 5	0.06	2	10	17.250
Case 6	0.06	2	5	18.040
Case 7	0.06	2	0	18.400
Case 8	0.06	2	-5	18.597
Case 9	0.06	2	-10	18.798
Case 10	0.06	2	-11	18.820
Case 11	0.09	2	-11	20.760

The range of tip speed ratios investigated, [2-3], are typically found to be small enough to allow the presence of dynamic stall in VAWTs. Additionally, the values of κ tested are in the range of the average reduced frequency ($c/2R$), between 0.025 and 0.1828, as found in VAWTs [56, 109, 110].

(ii) The non-dimensional pitch rate parameter, q, that is formulated by Daley et al. [82] is given as:

$$q = \dot{\alpha} c / (2U_{ref}) \tag{4.2}$$

It is necessary to emphasize that the pitch rate $\dot{\alpha}$ and the velocity changes constantly in VAWTs, thus, the non-dimensional pitch rate q uses the values of the pitch rate and the relative velocity at a specific time, t, as input values corresponding to $\dot{\alpha}$ and U_{ref} respectively. The expression in Eq.(4.2) is also used to calculate the non-dimensional pitch rate in the ramp-up motion, but because the pitch rate $\dot{\alpha}$ has a constant value then q is easily calculated.

In the second approach, the incoming wind flow U, as represented in Fig. 4.1, was a time-depend function given by the relative velocity Eq. (2.1) of VAWTs. For this approach, a user defined function was implemented to vary the incoming flow (inlet velocity) according to Eq. (2.1) and at the same time the pithing rate according to Eq. (2.2). In order to have a single value of the non-dimensional pitch rate using Eq. (4.2) then, the pitch rate, $\dot{\alpha}$ and U_{ref} uses the value of the Eq. (2.2) and Eq. (2.1), respectively, at the instant of time t when the angle of attack approaches the static stall angle.

(iii) The constantly changing relative velocity described by the Eq. (2.1), has been investigated in order to assess its influence on the stall-onset and to compared the existing difference on the stall-onset angle when using a constant-average relative velocity. The average relative velocity, ωR or λV_{∞}, that is an approximated average of the Eq. (2.1) in one revolution, is typically used in VAWTs in order to simplify the analysis [30, 48]. Thus, it is interesting to investigate if a difference exists when using the actual relative velocity rather than its average value.

4.2.1 Stall-onset estimation

As mentioned previously, there are several techniques to identify the stall-onset angle. In this Chapter, the stall-onset angle, α_{os}, is calculated as the angle where a maximum value in the chordwise force coefficient is observed. This criterion is also recommended in [45, 44, 111].

The chordwise force coefficient, C_c, for an oscillating aerofoil is represented in Fig. 4.1 and is described as follows:

$$C_c = C_L \sin(\alpha) - C_D \cos(\alpha) \tag{4.3}$$

Due to the prominent influence of the dynamic stall in the upstream zone of the VAWT, [86, 55], i.e. from $\omega t = 0 - \pi$, in this chapter we focus on evaluating the stall-onset angle in this range of angle of attack.

4.3 Influence of κ, λ and β at constant Reynolds number

The analysis of the influence of the reduced frequency (κ), tip speed ratio (λ) and pitch angle (β) on the stall-onset angle by using the first approach for a constant Reynolds number has shown the following results:

(i) With the increase in the reduced frequency (κ), the calculated stall-onset angle (α_{os}) increases. For example, in the simulation with a reduced frequency of $\kappa = 0.09$, the stall-onset angle was $\alpha_{os} = 20.60^{\circ}$. Decreasing the reduced frequency to $\kappa = 0.06$ produced the stall-onset angle $\alpha_{os} = 18.79^{\circ}$. For both values of κ the tip speed ratio was $\lambda = 2$ and the pitch angle was $\beta = -11^{\circ}$.

The delay in the stall conditions with the increase in the reduced frequency is also observed in the comparison of the pressure coefficient (C_p) and skin friction (C_{fx}) curves including in Fig. 4.2(a-b). The skin friction at the Reynolds number 2×10^5 for two dynamic cases with reduced frequencies $\kappa = 0.09$ and $\kappa = 0.06$, and one static simulation were computed at the angle of attack of 13°. At the static condition, the aerofoil stalls at 13° and thus a high negative pressure coefficient is observed close to the aerofoil leading edge. This is a critical point where a laminar separation bubble (LSB) concentrated at the LE collapsed [44]. For the unsteady simulations, this high minimum pressure is not reached, suggesting a delay in the pressure collapsed for the reduced frequency $\kappa = 0.06$ and a further delay for the reduced frequency $\kappa = 0.09$.

Another interesting characteristic that confirms the delay in the stall is recognized by observing the skin friction (C_{fx}), as plotted in Fig. 4.2(b). The closer the laminar separation bubble (LSB) to the aerofoil leading-edge indicates an earlier collapse of the pressure coefficient and, an earlier separation of the boundary layer occurs. The region occupied by the LSB is exemplified for the static case in Fig. 4.2(b) by circular and triangular symbols; at these two points the skin friction experiences a zero value. The LSB region for the unsteady cases with a reduced frequency $\kappa = 0.06$ is closer

to the leading edge of the aerofoil compared for the case with the reduced frequency $\kappa = 0.09$.

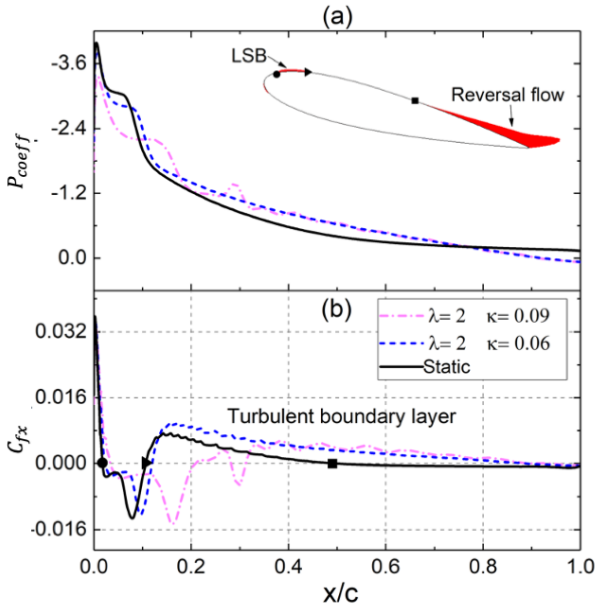

Figure 4.2: (a) Pressure coefficient, and (b) skin friction along the chord of an oscillating aerofoil at the angle of attack 13°. ● Laminar boundary layer separation, ► Reattachment of LSB, ■ Start of reversal flow in the turbulence boundary layer at TE.

Moreover, the point where the turbulent boundary layer (formed after the reattachment of the LSB) experience $C_{fx} = 0$ is an additional parameter of reference to evaluate the magnitude of the delay in the stall-onset angle; closer is this point to the LE, then the sooner stall occurs. For the static case, the turbulent boundary layer experiencies $C_{fx} = 0$ at 50 % of the chord, this point is indicated with a square in Fig 4.2 (b). For the unsteady cases with $\kappa = 0.06$ and $\kappa = 0.09$ the turbulent boundary layer with $C_{fx} = 0$ is located at 95% and 97 % from the LE. More details on the pressure coefficient and skin friction behaviours under unsteady conditions are described by Ekaterinaris & Platzer [95].

The increase of the stall-onset angle with the reduced frequency is confirmed by comparing the calculated stall-onset angle, α_{os}, for another two dynamic simulations with $\kappa = 0.02$ and $\kappa = 0.04$ using both a tip speed ratio of $\lambda = 3$ and a pitch angle of

$\beta = -11^{\circ}$ at Re 2×10^5. The stall-onset angle, α_{os}, results in 14.70° and 16.22° for the reduced frequencies $\kappa = 0.02$ and 0.04, respectively.

(ii) The influence analysis of the tip speed ratio (λ) has shown that with a decrease in λ the stall-onset angle (α_{os}) grows. For the tip speed ratios investigated with values 2, 2.37 and 3, the computed α_{os} were 18.82°, 17.68° and 16.56°, respectively. The skin friction for these dynamic cases is illustrated in Fig. 4.3 (a) and it was revealed that the lower is λ then more is the delay in the stall-onset angle. For example, the position of the laminar bubble (first two locations with $C_{fx} = 0$), is closer to the leading edge aerofoil for $\lambda = 3$, followed by $\lambda = 2.37$ and finally $\lambda = 2$. Moreover, the point where the turbulent boundary layer experiences $C_{fx} = 0$, which indicates the start of reverse flow, is located at 84 % from the aerofoil LE for $\lambda = 3$, at 86 % for $\lambda = 2.37$ and 88% for $\lambda = 2$. Therefore, this indicates that the tip speed ratio $\lambda = 2$ presents the largest delay in the stall conditions. Compared with the location of the LSB in the skin friction between the two values of the reduced frequency in Fig. 4.2(b), the effect on the skin friction due to the tip speed ratio in Fig.4.3(a) is minimal.

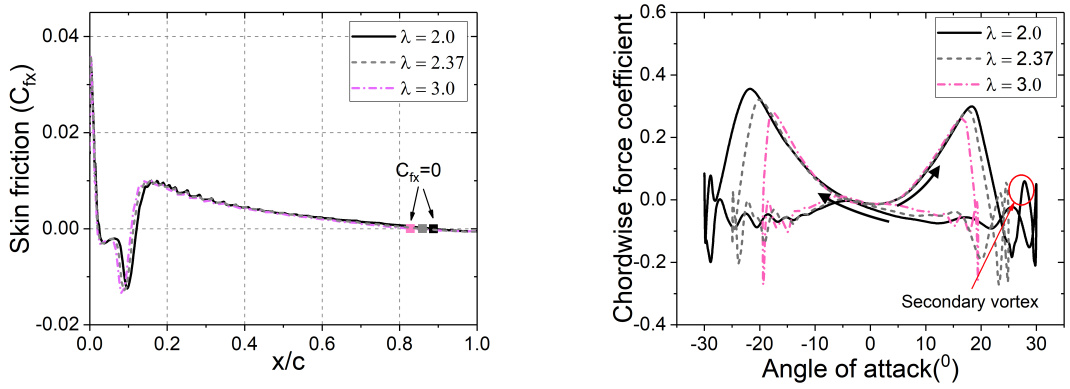

(a) (b)

Figure 4.3: (a) Skin friction, and (b) chordwise force coefficient, as a function of the angle of attack for λ= 3, 2.37 and 2 with values of $\kappa = 0.06$, $\beta = 0$ and $Re = 2 \times 10^5$. Arrows indicate the direction in the angle of attack with the motion of the aerofoil.

The tip speed ratio plays a key role that is extremely important for the VAWT

operation; it substantially influences the maximum angle of oscillation (α_{max}). Larger is the difference between the stall-onset and the maximum angle of oscillation, ($\alpha_{max} - \alpha_{os}$), then secondary vortices are more likely to occur and thus deeper stall conditions are observed.

For the tip speed ratio $\lambda = 2$, this difference, $\alpha_{max} - \alpha_{os}$, is 11.6°. This allows the release into the wake of the primary vortex formed at the leading edge (LEV), a shear layer vortex (that if formed at the TE, and is opposite in direction to the LEV) and the formation of a secondary vortex, as indicated in Fig. 4.4(a). The secondary vortex is also observed in the chordwise force coefficient, C_C, included in Fig. 4.3(b) where the second peak in C_c is identified.

In the case of $\lambda = 3$, the difference between α_{max} and α_{os} is 3.44° and hence, a primary vortex is released and the shear layer vortex is formed; there is no indication of a secondary vortex in the chordwise force coefficient in Fig. 4.3(b), neither in Fig. 4.4(b). More details on the deep stall conditions can be found in [46].

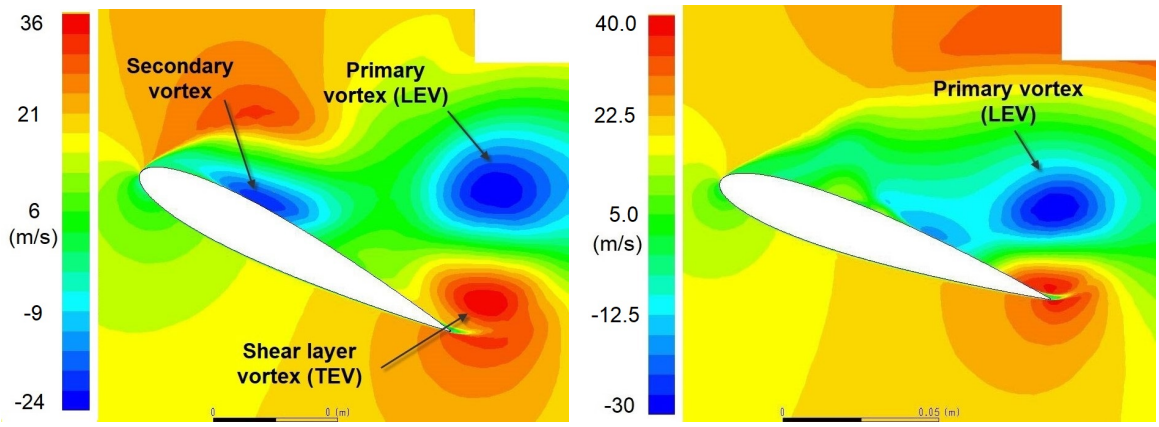

(a) (b)

Figure 4.4: The x-component velocity contour for the oscillating NACA0015 with (a) $\lambda = 2$ at $\alpha = 26.8^\circ$, and (b) $\lambda = 3$ at $\alpha = 20^\circ$ at $Re = 2 \times 10^5$.

(iii) The changes in the values of the pitch angle (β) produce an increase in the stall-onset angle if β increases the maximum angle of attack. For example, the stall-onset angle using $\beta = 10^\circ$ was $\alpha_{os} = 17.25^\circ$ and when using $\beta = -10^\circ$ was $\alpha_{os} = 18.79^\circ$.

The corresponding maximum angle of attack (α_{max}) for both pitch angles was 20° for $\beta = 10°$ and α_{max}=40° for $\beta = -10°$. The maximum angle of attack, α_{max}, is calculated by performing a mathematical analysis of Eq.(2.2) that results in the expression $\alpha_{max} = \arctan([\lambda^2 - 1]^{-1/2}) - \beta$. Thus, the maximum angle of attack could be calculated using the corresponding pitch angle, a reduced frequency $\kappa = 0.06$ and, a tip speed ratio of $\lambda = 2$.

In Fig. 4.5(a), the skin friction for five values of β are plotted. It is observed that more positive is β thus closer is the laminar bubble to the leading edge and thus the stall occurs at a lower angle of attack. Additionally, the turbulent boundary layer point with $C_{fx} = 0$ has progressed closest to the LE for the most positive β value of 10° (Fig. 4.5(a)). Nevertheless, in general, the difference among the skin frictions curves for the range of pitch angles tested [-10° to 10°] are minimal and the overall variation in α_{os} due to the influence of the pitch angle (β) is less than 1.54°. The impact of the pitch angle on the stall-onset angle, compared with the tip speed ratio and the reduced frequency is the lowest.

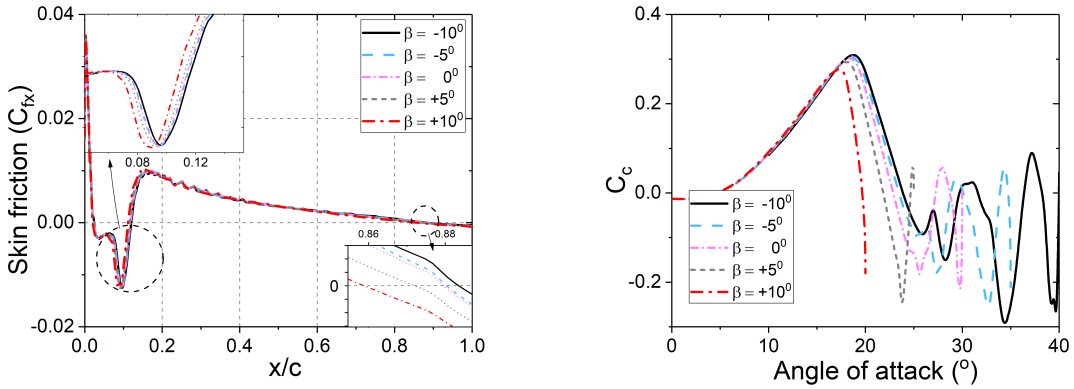

(a) (b)

Figure 4.5: (a) Skin friction along the non-dimensional chord length, and (b) chordwise force coefficient for several values of β at $Re = 2 \times 10^5$.

Similar to the tip speed ratio, the pitch angle also influences the maximum angle of attack. Thus, the severity in the stall conditions may be affected by changing the pitch

angle. In Fig. 4.5(b) the chordwise force coefficient for the five values of β are plotted. With a more positive β value as explained in the previous paragraph, a slight decrease in α_{os} is observed but also a decrease in the maximum angle of oscillation. Thus, as observed in Fig. 4.5(b) for the most positive β value there is no indication of secondary vortices. On the contrary, with the most negative β value, despite experiences the larger stall-onset angle, it also produces a very large maximum angle of attack that causes two secondary peaks in the chordwise force as observed in Fig. 4.5(b). Those peaks in C_C indicate the formation of multiple secondary vortices and therefore, the largest severity in the stall conditions.

4.3.1 Stall onset as a function of κ, λ and β

The simulation cases in Table 4.1 have assisted in investigating the influence of each variable on the stall-onset angle: the increase of the reduced frequency increases the stall-onset angle; the increase of the tip speed ratio decreases the stall-onset angle and, the increase of the pitch angle then a small decrease in the stall-onset is observed, see the previous Section 4.3. In order to observe the behaviour of the stall-onset for all the simulations as a function of a single variable, then, the predicted α_{os} for the simulations given in Table 4.1 are plotted as a function of the reduced frequency (κ), the tip speed ratio (λ) and the pitch angle (β) in Fig. 4.6 (a-c).

The analysis of the stall-onset, α_{os}, as a function of the reduced frequency, κ, in Fig.4.6(a) shows that with the increase of κ the stall-onset angle trends to a linear increment. Nevertheless, at the value of $\kappa = 0.06$, the cases from 3 to 10 despite having the same reduced frequency do not report the same α_{os} and, on the contrary, the stall-onset angles vary between 16° and 19° due to influences of the other two quantities. Fig. 4.6(b), which reports the α_{os} as a function of the tip speed ratio, λ, shows that for the simulations with the same $\lambda = 2$ the stall-onset angle varies between 18 and 21° and for $\lambda = 3$, α_{os} is between 14 and 17°. The Fig. 4.6(c) shows a large variation in the stall-onset angle for a given pitch angle. Although on the increase of the pitch angle a small decrease in the stall-onset is observed, the influence of the other two quantities shows a significantly larger influence on the stall-onset. These results confirm the suggested conclusions by Bucher at al. [7], which stated that the single parameter of the

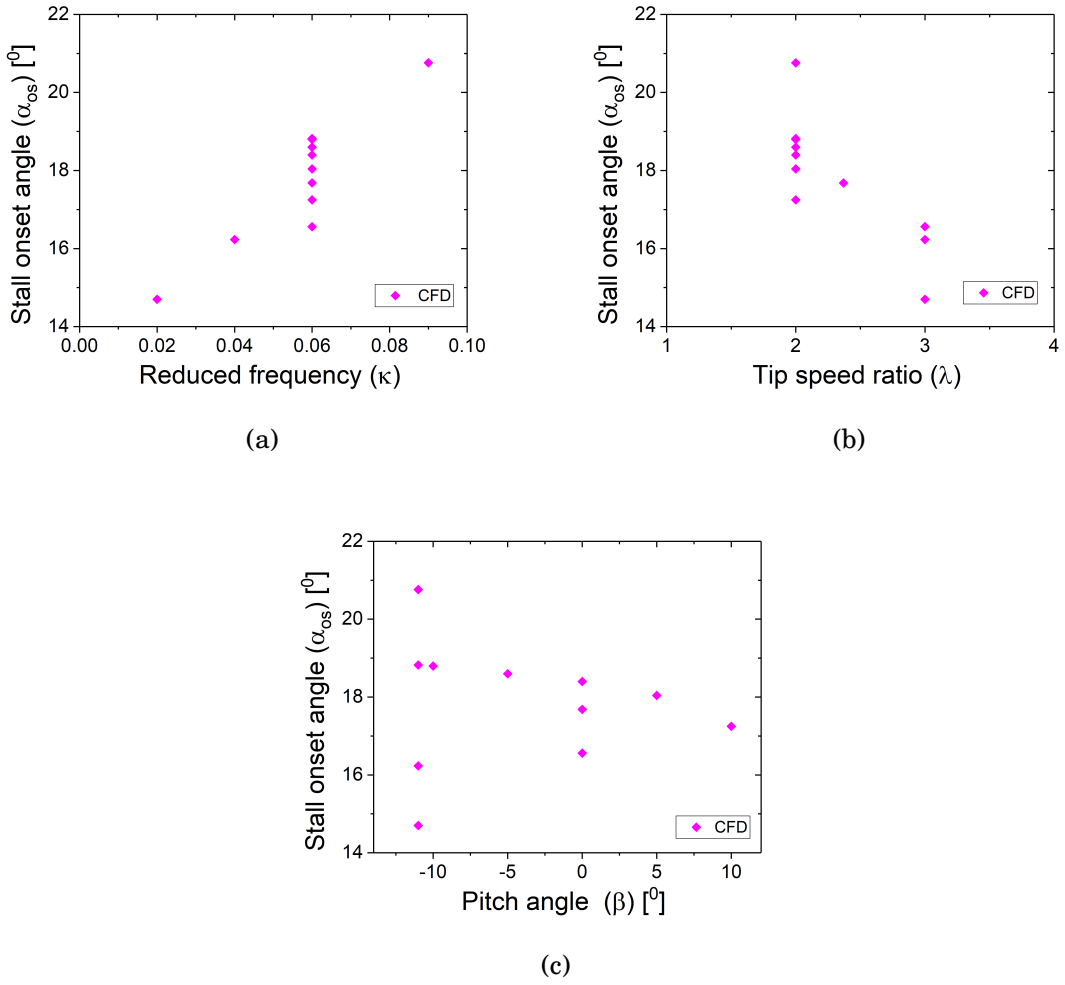

Figure 4.6: The predicted stall-onset angle for the simulations performed for all the cases in Table 4.1 and described as a function of the (a) reduced frequency, (b) tip speed ratio and, (c) pitch angle.

tip speed ratio is not enough to define both, the stall-inception and the dynamic stall range of operation in a VAWT. The Bucher et al. experimental tests were performed at Re=70,000 and are included in Fig. 4.7. This shows an agreement with the presented CFD results in Fig. 4.6(b) that takes into account, in addition to the tip speed ratio and reduced frequency investigated by Bucher at al.[7], the pitch angle.

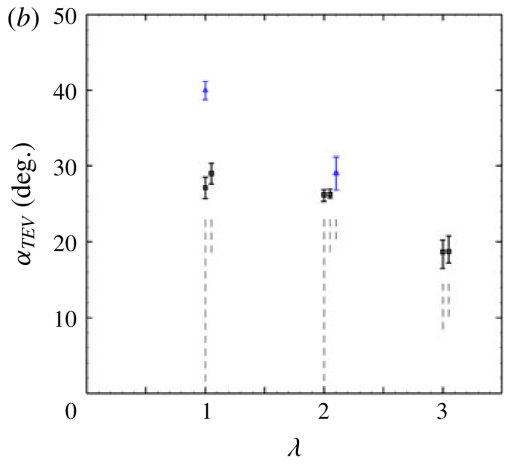

Figure 4.7: Results from Buchner et al. [7] of the trailing edge vortex formation at the leading edge of the aerofoil (TEV) as a function of the tip speed ratio investigated using a VAWT rotor with $\beta = 0^{\circ}$ and wind tunnel test. A black dot correspond to the parameter $K_c = c/2R$ with a value of 0.10 and blue for 0.15.

4.4 Non-dimensional pitch rate and Reynolds number effect

In this section, the stall-onset angle is evaluated as a function of the non-dimensional pitch rate, q, given by Eq. (4.2). This parameter involves the pitch rate, $\dot{\alpha}$, given by Eq. (4.1). Because $\dot{\alpha}$ is a time-dependent function, its value is evaluated at the instance when the angle of attack approaches the static stall angle. Three Reynolds number (based on the chord length) were evaluated by changing the magnitude of the incoming flow U_{ref} to 8, 20 and 33 m/s and obtaining the Reynolds number of 0.8, 2.0 and 3.3×10^5, respectively.

The analysis has revealed that the stall-onset angle, α_{os} increases linearly with the increase of the non-dimensional pitch rate, q, for all the Reynolds numbers tested, see Fig.4.8(a). Further, at the same q with the increase of the Reynolds number an increase in the stall-onset angle is observed.

The increase in the dynamic stall-onset angle, α_{os}, due to the increase of the Reynolds number is consistent with the increase in the static stall angle that has been studied experimentally in several investigations [75]. Also, Fig. 4.8(a) includes the stall-onset angle predicted by Sharma et al. [3] for a constant non-dimensional pitch rate, $q = 0.25$,

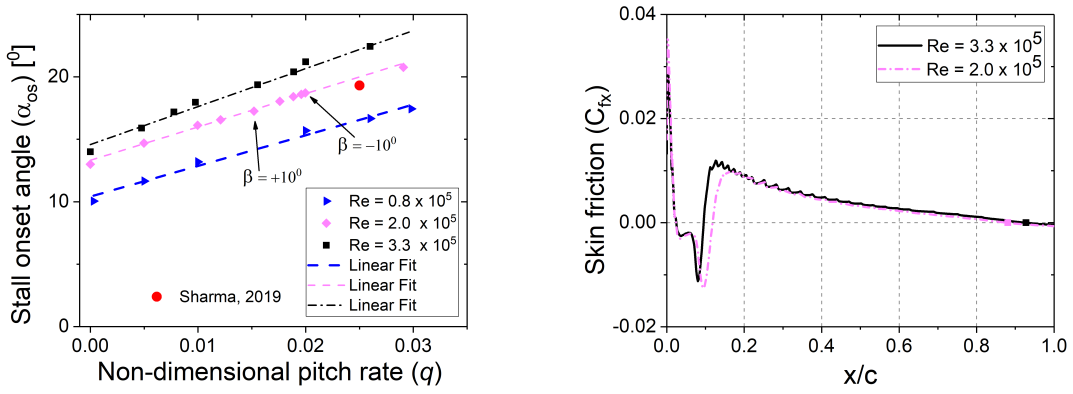

(a) (b)

Figure 4.8: (a) Stall-onset angle as a function of the non-dimensional pitch rate and Reynolds number for the NACA0015 aerofoil. The red dot corresponds to the α_{os} predicted with LES for a $q = 0.25$ in [3] and, (b) Skin friction along the non-dimensional chord length for two Reynolds numbers at $\alpha = 13°$.

a Re 2×10^5 and using the NACA0015. The predicted α_{os} with those LES is very similar to the α_{os} predicted with the present CFD RANS technique. Thus, this comparison suggests a good prediction of the stall-onset angle and supports the idea that the non-dimensional pitch rate, q is the parameter that need further analysis in the VAWTs.

The increase of α_{os} due to the increase in the Reynolds number is explained by the increase in the momentum exchange of the air particles from the outer boundary layer to the inner boundary layer of the aerofoil. Thus, improving the ability of the boundary layer to flow against the adverse pressure gradients and, as a consequence, longer is the time the boundary layer remains attached to the aerofoil surface.

The skin friction at the same angle of attack for two dynamic cases at two Reynolds number, Re, and with the same q are compared in Fig. 4.8(b). The region that encloses the air bubble, due to the laminar layer separation, is reduced at the highest Re as observed in Fig. 4.8(b) and the reattachment point as a turbulent boundary layer, occurs at an earlier distance from the leading edge of the aerofoil at Re$= 3.3 \times 10^5$. Additionally, at the same angle of attack, the turbulent boundary layer depicts a more positive skin friction coefficient and the point where $C_{fx} = 0$ occurs later along the chord

for Re$= 3.3 \times 10^5$. Thus, this indicated the boundary layer persists being attached at a larger angle of attack before separation occurs with an increase in the Reynolds number [112, 113].

Surprisingly, at the same Reynolds number, two dynamic simulations with different values of the tip speed ratio, reduced frequency and pitch angle that present similar values of non-dimensional pitch rate predict the stall-onset angles, α_{os}, with very similar values. For example, a simulation with tip speed ratio $\lambda = 2$, reduced frequency $\kappa = 0.09$ and pitch angle $\beta = -11^\circ$ produces a stall-onset $\alpha_{os} = 18.37^\circ$; for a second simulation with $\lambda = 1.5$, $\kappa = 0.075$ and $\beta = -13^\circ$ the predicted α_{os} is 18.32°.

For the mentioned-above two cases with a similar non-dimensional pitch rate, the pressure coefficient peaks due to the laminar separation bubbles are very similar, as shown in Fig. 4.9(a). Further, for these same dynamic cases, their skin friction values with $C_{fx} = 0$ are encountered at similar locations along the chord, thus indicating laminar separation bubbles with the same size for both dynamic cases, see Fig. 4.9(b). Also, the turbulent boundary layer achieves $C_{fx} = 0$ at the same chord locations. Therefore, present results suggest the non-dimensional pitch rate value when approaches to the static stall angle is the most important parameter that defines the stall-onset angle in the VAWT motion. Therefore, the effect of the tip speed ratio, reduced frequency and pitch angle on the non-dimensional pitch rate (q) requires more attention when the stall-onset angle is being predicted in the VAWTs.

The positive effect of non-dimensional pitch rate, q, on the stall-onset angle has been supporting by analysing the simulations presented in Section 4.3. It has been observed that the reduced frequency (κ) in the dynamic simulations increases the non-dimensional pitch rate (q) from 0.018 to 0.029 for the reduced frequencies of $\kappa = 0.06$ and $\kappa = 0.09$ respectively. Thus, the stall-onset angle increases. In the case of the tip speed ratio (λ), the decrease in λ increases the q values: for $\lambda = 2$, 2.37 and 3, the values of q were 0.018, 0.016 and 0.0121 respectively, and the stall-onset angle decreases in value. Similarly, the pitch angle β that increases the q values increases the stall-onset angle, see Table 4.2. The increase in the stall-onset angle due to the increase of q due to the changes in the pitch angles are marked with arrows in Fig. 4.8 (a). Therefore, it is confirmed that anytime the operating parameters, individually or

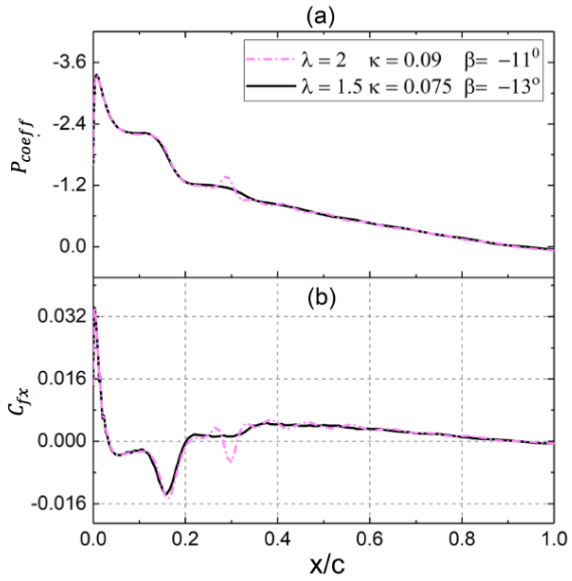

Figure 4.9: (a) Pressure coefficient and, (b) skin friction for two simulations with closed non-dimensional pitch rate value at $\alpha = 13°$.

combined, increase the non-dimensional pitch rate, then, an increase in the stall-onset angle is also observed.

Table 4.2: The instantaneous non-dimensional pitch rate calculated at α_{ss} for simulations with a constant $kappa = 0.06$ and different pitch angles and, their predicted stall-onset angle

β (°)	-10	-5	0	5	10
q	0.0199	0.0196	0.0188	0.0176	0.0152
α_{os} (°)	18.79	18.59	18.40	18.04	17.25
α_{max} (°)	40	35	30	25	20

4.5 Effect of the relative velocity on the stall-onset angle

In the previous sections, it was found that the stall-onset angle depends on the non-dimensional pitch rate and Reynolds number. In a VAWT with a constantly changing

relative velocity, a fluctuation in both the non-dimensional pitch rate and Reynolds number occurs and this fluctuation increases in amplitude by decreasing the tip speed ratio. Therefore, the effect of the fluctuating relative velocity is investigated by using a time-varying incoming flow as given by Eq.(2.1) and described in the second approach in Section 4.2(iii).

The fluctuation in the Reynolds number gives rise to the interest in investigating whether or not a difference on the stall-onset angle exists if using an average of the fluctuating relative velocity, $V_{mean} \approx \lambda V_\infty$, instead of the actual fluctuating relative velocity. Two cases are being analysed using the fluctuating relative velocity described in Eq. (2.1). First, using a tip speed ratio $\lambda = 2$ and $V_\infty = 10\ m/s$ and, second, using a tip speed ratio $\lambda = 3$ and $V_\infty = 20/3\ m/s$. For both cases, $\kappa = 0.06$ and $\beta = 0^\circ$ were employed.

The analysis shows that the tip speed ratio $\lambda = 2$ produces a Reynolds number that fluctuates in the range $1 - 3 \times 10^5$ and $\lambda = 3$ produces Reynolds number in the range $1.4 - 2.6 \times 10^5$. These two cases with a fluctuating velocity maintain a similar average relative velocity, $\lambda V_\infty = 20\ m/s$, thus resulting in the same average Reynolds number 2×10^5. In Table 4.3, the predicted stall-onset angle, α_{os}, for $\lambda = 2$ and 3, with a fluctuating velocity V_{rel} and a constant wind velocity V_{mean}, is presented. The stall-onset angle, α_{os} is included for the positive angles of attack (upstream zone of the rotor) and the negative angles of attack (downstream zone). In addition, the non-dimensional pitch rate (q) and the instantaneous velocity (V_{ins}) when the angle of attack approaches 13° are included for all the cases investigated in the upstream and downstream zones.

For the case (i) with $\lambda = 2$, the stall-onset angle predicted using a fluctuating wind velocity results in $\alpha_{os} = 18.37^\circ$ for the upstream zone of the rotor, and this is very similar to $\alpha_{os} = 18.32^\circ$ when using the average wind velocity, V_{mean}. For all the cases, the non-dimensional pitch rate (q) and Reynolds number are evaluated at the instant the angle of attack is $\alpha = 13^\circ$ [1].

For the incoming flow using the V_{rel} equation, the wind velocity calculated at $\alpha = 13^\circ$ is $V_{inst} = 28.41$ m/s and $q = 0.013$; on the other hand, for the constant incoming wind velocity of 20 m/s case, the non-dimensional pitch rate is $q = 0.018$. Since q is larger for

[1] Despite the Reynolds number fluctuation can change α_{ss}, this fluctuation is very small, and the variation in q is negligible

Table 4.3: Main characteristics of the stall onset for the two cases studied and evaluated upstream (up) and downstream (dw) of the rotor.

	Case (*i*) (λ=2)		Case (*ii*) (λ=3)	
Parameter	$V_{rel}(t)$	V_{mean}	$V_{rel}(t)$	V_{mean}
α_{os} (°) [upstream]	18.37	18.32	16.31	16.56
q [upstream]	0.013	0.0189	0.01	0.012
$V_{ins}(m/s)$ [upstream]	28.41	20.00	24.30	20.00
α_{os} (°) [downstream]	23.97	21.80	18.14	17.63
q [downstream]	0.096	0.050	0.027	0.020
$V_{ins}(m/s)$ [downstream]	10.55	20	14.57	20

the constant wind velocity case, then it is expected to have a larger α_{os}, as explained in the previous section and illustrated in Fig. 4.8(a), but this is not observed because of the change in the Reynolds number. The Reynolds number has resulted in $Re = 2.8 \times 10^5$ for the incoming flow with the V_{rel} equation, and in contrast to the effect on q, the incoming flow with the constant wind velocity produces a $Re = 2 \times 10^5$ that is lower than the fluctuating velocity case.

For the case (ii) with $\lambda = 3$, similar results were obtained. The stall-onset angle α_{os} produced by both incoming flow conditions were very close in value; the calculated α_{os} with the fluctuating wind velocity was 16.31° and using a constant wind velocity, $\alpha_{os} = 16.56^\circ$. The relative velocity again increases the actual wind velocity during the upstroke motion of the aerofoil, being $V_{ins} = 24.30$ m/s and q reduces its value to 0.01. Then, the increase in the Reynolds number, $Re = 2.4 \times 10^5$ increases α_{os}, see Table 4.3. On the other hand, the constant wind velocity produces $q = 0.012$ that is larger than in the V_{rel} of the incoming flow, but the Reynolds number is 2×10^5, slightly lower than the V_{rel} case; thus, both incoming flow conditions, the constant-average and the time-varying velocities predict similar stall-onset angles.

Present results suggest that for the upstream zone of the rotor, despite the fluctuations in both, the Reynolds number and the non-dimensional pitch rate (due to the

relative velocity fluctuation), the use of average relative velocity, λV_∞ gives a good approach to the stall-onset angle.

Moreover, for the negative angles of attack (downstream zone of the VAWT rotor), and at a tip speed ratio of $\lambda = 2$, it is observed in Fig. 4.10 that the stall-onset angle, α_{os}, increases to 23.97° when using the V_{rel} as the incoming flow. This increase is due to the large increase in non-dimensional pitch rate, q, as a result of the very low wind speed V_{ins} of 10.55 m/s, see Table 4.3. Using the average relative velocity V_{mean}, the stall-onset angle was 21.80° and $q = 0.50$, and this non-dimensional pitch rate has half the value compared to that of the non-dimensional pitch rate when using V_{rel}.

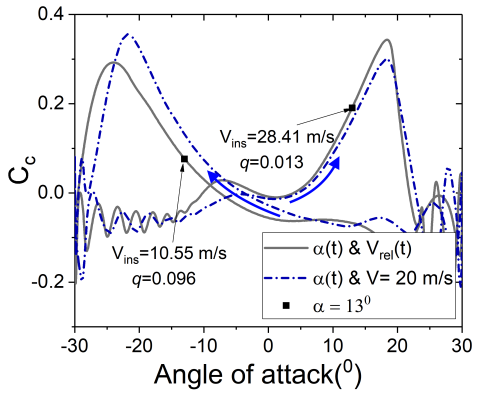

Figure 4.10: Chordwise force coefficient for $\lambda = 2$ using an incoming flow with: a constant velocity and with time-varying velocity given by the relative velocity Eq. (2.1). Arrows indicate the direction in the angle of attack with the motion.

This difference on the non-dimensional pitch rate and in the Reynolds number between the use of the V_{rel} incoming flow and the average value $V_\infty\lambda$ in the downstream region of the rotor is larger than in the upstream region of the rotor. Therefore, these findings suggest the use of an average relative velocity downstream is less convenient when evaluating the stall-onset angle in VAWTs.

Additionally, the computed chordwise force coefficients for the negative angles of attack, in Fig. 4.10, do not show a secondary peak after the stall-onset angle when compared with the constant velocity case of 20 m/s. The absence of a secondary C_C peak suggests that the dynamic stall phenomenon is less severe downstream than upstream

due the higher values of the non-dimensional pitch rate $q = 0.093$. Thus, this explained why the vortex shedding in the experimental tests (in previous investigations) has been observed to be more frequent upstream of the VAWT rotor (positive angles of attack) than in the downstream of the rotor.

4.6 Discussion

The analysis of the operating parameters that affect the stall-onset angle in VAWTs carried out in the present investigation has revealed important findings for the applications in VAWTs and for the applications in dynamic stall algorithms.

The increase in the reduced frequency, κ, increases the stall-onset angle and delay the separation of the boundary layer to larger angles of attack. This delay in the separation of the boundary layer is in agreement with previous investigations on the reduced frequency that have used the ramp-up and sine-pitching motion and have focused mainly on the lift stall (L) rather than the stall-onset angle [45, 74, 78]). The present findings explain why other authors that have studied the full rotor have found that an increment in the average reduced frequency ($c/2R$) may reduce the deep dynamic stall conditions to light stall or even non-stall at the same tip speed ratio [29].

The tip speed ratio and the pitch angle influence the magnitude of stall-onset angle. Nevertheless, their main role consists of defining the maximum angle of attack. When the maximum angle of attack is further increased to be larger than the stall-onset angle, deeper stall conditions are likely to occur. Hence, this means the several vortices formed upstream of the VAWT rotor can be released downstream and hence, reduce the power contribution of the VAWT in this latter zone. Thus, using the pitch angle as a strategy to control the maximum angle of attack can reduce the stalling degree conditions upstream of the rotor. Nevertheless, the tip speed ratio needs to be considered in order to select the most appropriate pitch angle, since both of them influence the maximum angle of attack and the stall-onset angle.

The pitch angle (β) evaluated here can be seen as being equivalent to the mean angle of oscillation from the sine-pitching motion. In previous investigations using the sine-pitching motions, instead of the VAWT angle of attack given by Eq. (2.2),

a parameter called the equivalent reduced pitch rate has been proposed to evaluate the stall-onset angle [65, 84]. Nevertheless, in those studies, an independence of the mean angle of oscillation with the stall-onset angle was suggested while in this thesis, the pitch angle influences the stall-onset angle. Thus, the changes in the stall-onset with different β values explains why changing the pitch angle in the VAWTs blades changes the azimuthal angle where stall occurs and affects the severity of the stalling conditions [6].

The most interesting finding of this work is the influence of the typical parameters of VAWTs, namely, the tip speed ratio (λ), reduced frequency (κ) and pitch angle (β) on the investigated non-dimensional pitch rate (q) when the angle of attack approaches the static stall value. The larger is the non-dimensional pitch rate, then the larger is the stall-onset angle.

The positive effect of the non-dimensional pitch rate to delay the stall and calculated here using the VAWTs equations agrees with the effect of the non-dimensional pitch rate calculated with the ramp-up motion in some previous investigations. For example, using a ramp-up motion, the increase in the constant non-dimensional pitch rate produces an increase in the stall point (stall-onset or lift stall) [77, 74, 78, 82]. In addition, the non-dimensional pitch rate, as calculated for the sine-pitching motion in [58], has been shown to have a positive effect, namely increasing the stall-onset angle.

The confirmation of the equivalence among the non-dimensional pitch rates corresponding to the angle of attack of VAWTs, the sine-pitching and ramp-up motions are very important investigations that require much more exploration.

The increase in the stall-onset angle due to the increase in the Reynolds number observed in this Chapter using the VAWT angle of attack agrees with the results of the ramp-up tests performed by Choudhry et al. [74] where the lift-stall angle (L) as a function of the non-dimensional pitch rate was investigated at three Reynolds numbers.

The stall-onset angle as a function of the non-dimensional pitch rate, q, has not been well investigated at low Reynolds numbers, such as the requirement of VAWTs to operate at low wind speeds. Therefore, the obtained results for the stall-onset angle calculated in this chapter, as a function of the non-dimensional pitch-rate at differ-

ent Reynolds number, results in an essential tool in predicting the stall-onset angle for VAWTs. Also, this is very useful data that should be incorporated into the semi-empirical dynamic stall methods [41, 46, 65].

Semi-empirical dynamic stall methods use a time-delay constant that defines the linear relation of the stall-onset as a function of the non-dimensional pitch rate. This time delay constant depends on the Reynolds number and has been evaluated before mostly for Reynolds number as large as 1 million [114, 48, 115]. Therefore, the present results can be integrated into some of the dynamic stall models, such as the Leishman-Beddoes, to predict the unsteady loads in applications with a range of operation of the Reynolds number $0.8 - 3.3 \times 10^5$.

Overall, the present analysis has revealed that the combined effect of the tip speed ratio, reduced frequency and pitch angle on the non-dimensional pitch rate is an essential factor that dictates the level of delay in the stall conditions. Thus, this effect explains why it has been not possible in the previous studies to define a range of tip speed ratios where the dynamic stall occurs in VAWTs: the resulting non-dimensional pitch rate can increase or decrease according to the combined effect of the tip speed ratio, reduced frequency, pitch angle and relative velocity.

In VAWT analyses, it is very common to use the average of the fluctuating relative velocity to investigate its aerodynamics instead of using the actual fluctuating relative velocity. The findings of this Chapter have shown that in the upstream region of the rotor, the stall-onset angle is not significantly affected when an average the relative velocity, rather than the actual relative velocity is employed. In contrast, in the downstream region of the rotor, where the low magnitudes of the relative velocity produce high values of the non-dimensional pitch rate and low Reynolds numbers, the prediction of the stall-onset angle using an average of the relative velocity instead of the actual relative velocity may have a significant impact.

In this Chapter, a single blade using the angle of attack and relative velocity equations of a VAWT has been used to investigate the stall-onset angle. Although these equations can be modified by using the full rotor due to the number of blades or the curvature effects, the effect of the non-dimensional pitch rate and Reynolds number on the stall-onset angle are likely to still valid.

4.7 Summary

The critical analysis of the variables that may affect the stall-onset performed in this Chapter have revealed some interesting results:

(i) The non-dimensional pitch rate and the Reynolds number are the primary parameters that affect the stall-onset angle in the VAWTs. The non-dimensional pitch rate is the result of the combined effect of all the operating parameters such as the tip speed ratio, pitch angle, angular velocity, incoming wind flow and relative velocity. Additionally, the stall-onset angle presents similar values when using an average velocity of the rotor and the actual relative velocity at the upstream zone of the rotor. On the contrary, at downstream of the rotor the stall-onset angle differs when using the actual relative velocity instead using the average velocity of the rotor. The present findings guide the verification procedure of the dynamic stall model (in Chapter 6) in order to consider the actual dynamic stall mechanism of the flow in the VAWTs.

(ii) The linear increase of the stall-onset angle with the non-dimensional pitch rate has been observed for the range of Reynolds number investigated here, namely, $0.8 - 3.3 \times 10^5$. These relations are fundamental to predict the time-delay constant at several Reynolds number as described in Chapter 6 and these time-delay constants are essential for an accurate prediction of the stall-onset for any dynamic stall method.

Chapter 5

Unsteady aerodynamics both upstream and downstream of VAWTs

5.1 Overview

In this Chapter, the VAWTs simulations have performed using six aerofoils, NACA0012, NACA0015, NACA0018, NACA0021, S1210 and NACA2418 with a different number of blades and several tip speed ratios. These simulations are carried out in order to gain a better understanding of the aerodynamics in the VAWTs and its influence in the torque contribution at upstream and downstream of the rotor. The information generated, namely, the torque coefficient at each azimuthal angle is used in Chapter 6 to assess the dynamic stall method and the double multiple streamtube theory. The main novelty of this chapter is the identification of the downstream zone of the rotor has being the zone which causes a decrease in the total torque coefficient that becomes more relevant with the increase of the tip speed ratio. The aerodynamics characteristics of the aerofoil profile that dictates the amount of torque produced at upstream and downstream of the rotor are deeply analysed. The present analysis, based on 132 CFD simulations, gives enough details that lead to the definition of strategies to improve the performance on VAWTs.

5.2 Methodology

To investigate both contributions to the total torque coefficient, from the upstream and downstream zones of the rotor, thus, a total of 132 VAWTs simulations were performed and are represented schematically in Fig. 5.1. The geometrical configurations of the VAWTs consist of 18 different rotors: at each configuration of VAWT with one, two and

three blades, as represented in Fig. 5.1, six aerofoils shapes where tested. Thus, each of these 18 rotor designs where simulating at several tip speed ratios.

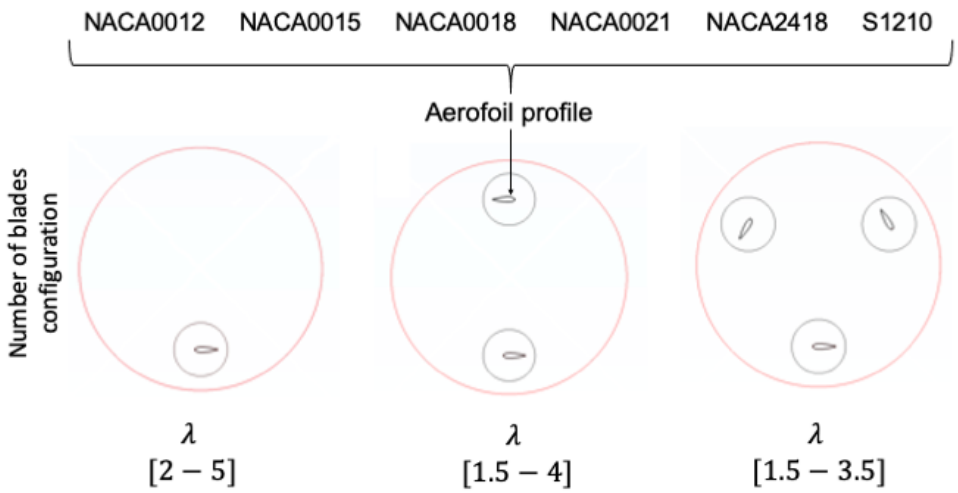

Figure 5.1: Schematic representation of the VAWT CFD simulations investigated in this Chapter. For each blade configuration, 6 aerofoils were employed. The range of tip speed ratio this 18 configurations is included accordingly the number of blades.

5.2.1 Numerical settings

The CFD simulations perform in this Chapter 5 for the vertical axis wind turbines use the numerical settings explained in detailed in Section 3.2.3. Consult that section for more details of the boundary conditions, domain, mesh and time step analysis. A summary of the final numerical setting for the simulation performing in this Chapter is addresed in Table 5.1

5.3 Operating regimes on VAWTs

A typical performance curve of a VAWTs describes almost a normal distribution in the power coefficient as a function of the tip speed ratio; this is similar to the power curve observed in Fig. 2.3. The region corresponding to the tip speed ratios before the optimum operating conditions are frequently related to the presence of the dynamic

Table 5.1: Summary of the numerical setting to perform the CFD simulations of the VAWTs.

Software	Fluent 17.2	**Solution method**	Pressure-velocity coupling
Scheme	Coupled	**CFL**	10
Azimuthal increment	$\Delta\theta = 0.25^{\circ}$	**No. of cycles**	20
Domain boundary conditions	Velocity inlet, Pressure outlet, Upper and lower symmetry	**Aerofoil boundary condition**	non-slip
No. elements around aerofoil	1000	**Chord length**	0.265m
Fluid	Air	**Mesh motion (ω)**	Eq. (3.7)
Radius	1m	**Pitch angle**	0°

stall phenomenon. After the optimum operating conditions, the dynamic stall has no longer any influence, and the VAWTs blades operate under unsteady full attached flow and this region is called, throughout this paper, as the high tip speed ratio regime. More information about these regimes in VAWTs may be found in [2].

The integrated torque coefficient during one cycle as a function of the tip speed ratio for a VAWT using the NACA0012 aerofoil is presented in Fig. 5.2. It is observed that with the increase in the number of blades the optimum torque coefficient is shifted to smaller tip speed ratios. In addition, after an optimum value of the torque coefficient occurs, then with a further increase in the tip speed ratio, the total torque coefficient decreases for all the number of blades investigated. To gain much more detail about the causes of this effect, then, the torque coefficient as a function of the azimuthal angle is evaluated next.

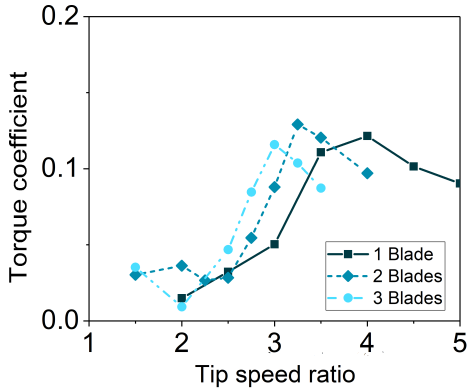

Figure 5.2: The total torque coefficient of as a function of the tip speed ratio for a VAWTs using the NACA0012 and a constant free-stream wind speed of 8 m/s.

The azimuthal torque coefficient, $C_Q(\theta)$, for the one-bladed VAWT with the NACA0012 and the lift and drag force coefficients are presented in Fig. 5.3 (a-c). For the tip speed ratios $\lambda \leq 3.5$, a loss in C_Q has been identified upstream of the rotor. The loss in C_Q is marked with a square in Fig. 5.3(a) and this suggests that the dynamic stall phenomenon has taken place. Interestingly, these tip speed ratios occur before the optimum torque coefficient (total) observed at $\lambda = 4$ in Fig. 5.2 for the one-blade VAWT.

The analysis of the lift and drag force coefficients for $\lambda \leq 3.5$ in Fig. 5.3 (b-c) shows clearly the presence of the dynamic stall phenomenon. For the upstream section of the rotor, from 0 to 180°, deep stall conditions are observed, i.e. a large hysteresis is experienced in the lift and drag force coefficients as shown for the tip speed ratios of 2 and 2.5. Despite the hysteresis being small for the tip speed ratios of 3 and 3.5, this indicates that the dynamic stall phenomenon still influences the unsteady loads, and usually this is called light dynamic stall.

At the downstream section of the rotor, from 180 to 360°, the sudden loss in the torque coefficient is no longer observed at any tip speed ratio as well as the loss in the force coefficients. Nevertheless, the presence of a slight hysteresis in both the lift and the drag force coefficients indicate the influence of the dynamic stall as a light stall condition for the tip speed ratios of 2 and 2.5. Thus, it may be concluded that the dynamic stall phenomenon is less severe downstream of the rotor and upstream of

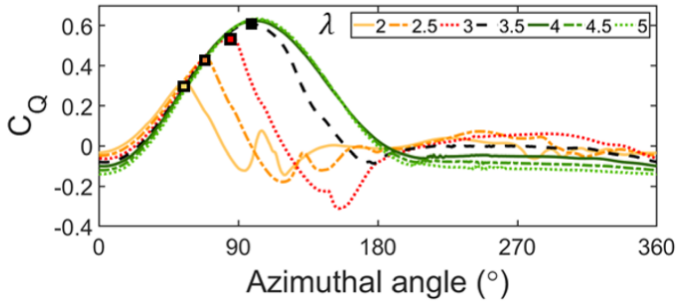

(a)

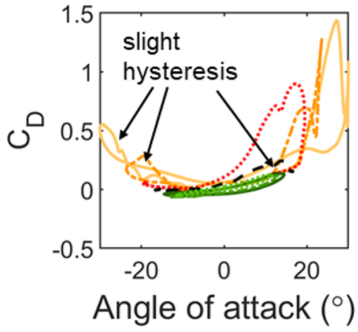

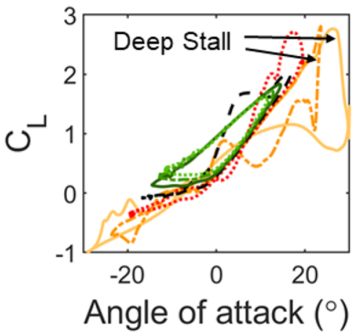

(b) (c)

Figure 5.3: (a) Azimuthal torque coefficient in one revolution at several tip speed ratios of the one- bladed NACA0012 aerofoil, (b) drag force coefficient, and (c) lift force coefficient as a function of the angle of attack for several tip speed ratios for the one-bladed NACA0012 aerofoil.

the rotor it takes place for a wider range of tip speed ratios, i.e. for a range of [2-3.5] upstream and [2-2.5] downstream of the rotor.

Following the analysis of the torque coefficient in Fig. 5.3(a), it is observed that after the tip speed ratio of 4 (at the optimum torque coefficient in Fig. 5.2), there is no indication of a loss in the torque coefficient or in the lift and drag force coefficients in Fig. 5.3(b-c). This is an indication of a fully attached regime.

Figure 5.2 includes the total torque coefficient as a function of the tip speed ratio and this shows that the optimum C_Q occurs at a tip speed ratio of 3.5 and 3 for the

two-bladed and three-bladed turbines, respectively. Similar to the analysis of the one-bladed turbine, the azimuthal torque coefficient is presented for two and three-bladed VAWTs in Fig. 5.4 and is compared with the total torque coefficient in Fig. 5.2. The azimuthal torque coefficient upstream shows the loss at $\lambda < 3.5$ for the two-bladed turbine, and for the three-bladed turbine, this loss in the torque coefficient is observed at $\lambda < 3$.

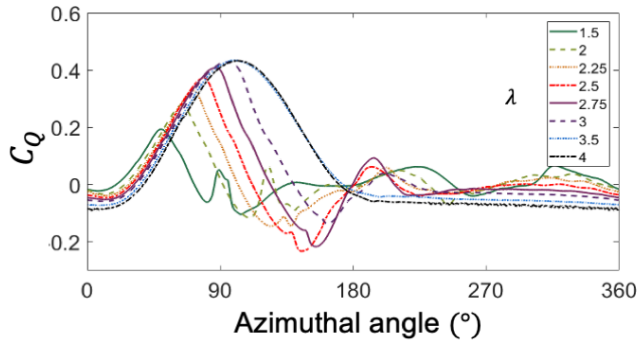

(a)

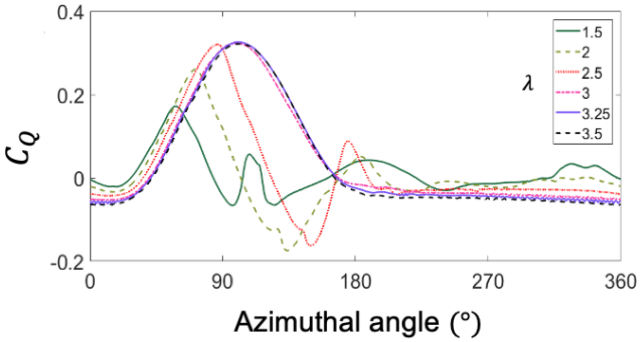

(b)

Figure 5.4: Azimuthal torque coefficient at several tip speed ratios for a VAWTs using the NACA0012 aerofoil and with the number of blades (a) two, and (b) three.

In general, it can be concluded that a dynamic stall regime takes place at the tip speed ratios before an optimum value on the total torque coefficient and after this value, a fully attached flow regime is experienced, where a decrease in the total torque

coefficient is observed for all the number of blades investigated.

5.4 *Influence of the aerofoil on the upstream and downstream torque contributions*

The analysis of the upstream torque contributions for the six aerofoils presented in Fig.5.5 (a-c) shows that the S1210 is the aerofoil with the largest torque coefficient for the different number of blades investigated on the upstream side of the turbine. Further, the differences of the C_Q for the S1210 with the C_Q of the symmetrical aerofoils increases with the increase in the tip speed ratio. The next best torque coefficient upstream is produced by the cambered NACA2418. Subsequently, the torque contributions upstream were observed, in decreasing order, for the symmetrical aerofoils NACA0021 and NACA0018, then NACA0015 and last the NACA0012. The torque coefficient using the S1210 aerofoil increases by up to 70% compared with the symmetrical aerofoils torque coefficient for the one bladed-turbine and at a tip speed ratio $\lambda = 5$; also, the S1210 increase in C_Q for the two and three-bladed turbines was 62% (at $\lambda = 4$) and 56% (at $\lambda = 4$), respectively.

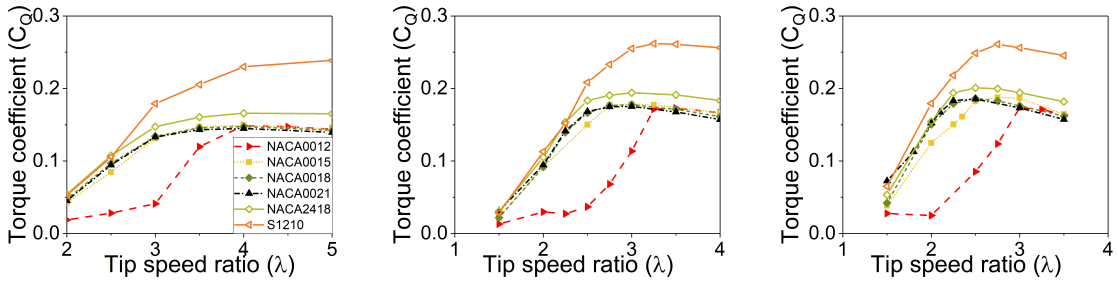

Figure 5.5: Upstream torque coefficient, $C_{Q,up}$, of six aerofoils for a VAWT with (a) one blade, (b) two blades and, (c) three blades.

Following the upstream analysis, all the aerofoils show an increase in the torque coefficient, C_Q, with the increase in the tip speed ratio, λ, approaching to a maximum C_Q value, that barely decreases in magnitude with a further increase in the tip speed

ratio. For instance, the NACA0012 for the two-bladed turbine (Fig. 5.5b) starts with a very poor torque coefficient at the lowest tip speed ratio $\lambda = 1.5$; while increasing λ the torque coefficient increases and reaches a maximum torque coefficient $C_Q = 0.17$ at $\lambda = 3$ and, after this tip speed ratio the magnitude of torque coefficient decreases by only 3%. A similar behaviour in the torque coefficient upstream is observed for the other cases investigated. Upstream, the NACA012 aerofoil is the aerofoil with the poorest torque coefficient at small tip speed ratios, λ. Nevertheless, when this aerofoil reaches its optimum torque coefficient at $\lambda = 4$, 3.5 and 3, for one, two and three-bladed VAWT, respectively, then it produces a better torque coefficient than the other aerofoils.

In the analysis of the downstream torque coefficients, see Fig. 5.6(a-c), it has been observed that the cambered S1210 aerofoil produces the more negative torque coefficient, followed by another cambered aerofoil, the NACA2418. In none of the number of blades investigated does the S1210 aerofoil produce a positive torque in the downstream region. While the NACA2418 produces a small positive torque coefficient at low tip speed ratios, such as $\lambda = 2.5$ for the one-bladed turbine and, at $\lambda = 1.5$ for the three-bladed turbine. The torque coefficient for the symmetrical and cambered aerofoils becomes more negative with the increase in the tip speed ratio.

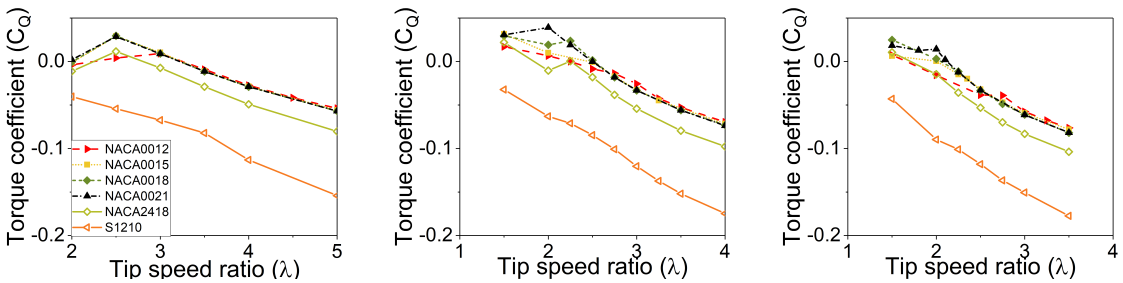

Figure 5.6: Downstream torque coefficient, $C_{Q,dw}$, of six aerofoils for a VAWT with (a) one blade, (b) two blades and, (c) three blades.

Further, at the downstream analysis of the rotor, all the symmetrical aerofoils except the NACA0021, present a smaller and negative torque coefficient for all the tip

speed ratios and solidities in comparison with the cambered aerofoils. In addition, the symmetrical aerofoils, in general, produce a positive torque coefficient at small tip speed ratios. For instance, for the one-bladed turbine at the tip speed ratio $\lambda < 3$, for the two-bladed turbine at $\lambda = 2.25$ and the three-bladed turbine at $\lambda < 2$. After a negative torque coefficient is observed, an increase in the tip speed ratio results in an increase in the negative torque coefficient for all the aerofoils. Despite the NACA0021 producing the best torque coefficient at the smaller tip speed ratios, with a further increase in the tip speed ratio the NACA0012 aerofoil becomes the aerofoil with the least negative torque coefficient as observed at the tip speed ratio $\lambda = 2.75$ for the three-bladed turbine in Fig. 5.6(c).

The addition of the upstream and downstream torque contributions are observed in the total torque coefficient, $C_{Q,T}$ in Fig. 5.7(a-c). All the aerofoils describe a torque coefficient curve that, in general, starts at low tip speed ratios with a poor torque generation, reaches an optimum torque coefficient and then the torque coefficient starts to decrease.

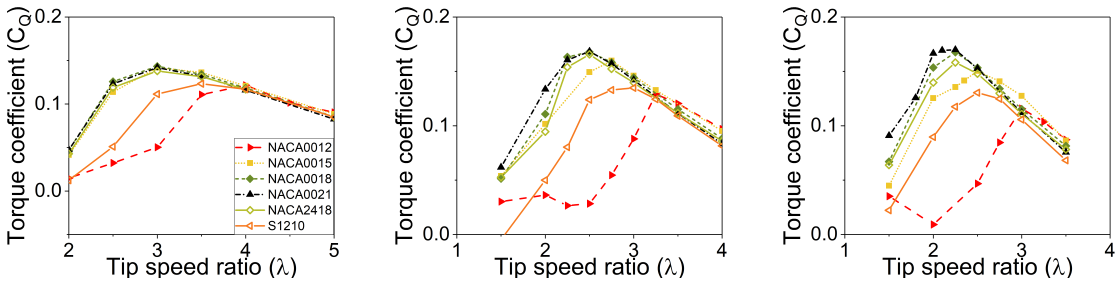

Figure 5.7: Total torque coefficient, $C_{Q,T}$, , as a function of the tip speed ratio for the six aerofoils for a VAWT with (a) one blade, (b) two blades and, (c) three blades.

The downstream torque coefficient plays a significant role in defining the total torque coefficient, mainly after the optimum torque coefficient is observed in Fig. 5.6 for all the number of blades. In other words, while in the upstream contributions to the torque coefficient approaches an optimum value that barely change with the increase in the tip speed ratio, the addition of the downstream contribution produces a reduced

total torque with the increase in the tip speed ratio. The aerofoils with the most effect on the total torque coefficient have been the cambered aerofoils, and this is due to the large negative torque coefficient downstream of the rotor.

Despite the very good performance upstream of the S1210 aerofoil, its high negative $C_{Q,dw}$ contribution has dramatically affected its total torque coefficient for all the number of blades investigated. As a result, the S1210 torque coefficient is observed to be lower than the total torque coefficient produced by the aerofoils NACA0021, NACA0018, NACA0015 and NACA2418. The cambered NACA2418 aerofoil, similarly, presented a good upstream torque coefficient, nevertheless downstream its negative impact was smaller than that of the S1210, and thus produced a similar total torque coefficient as the symmetrical NACA0018 for all the solidities evaluated.

Moreover, the analysis of the total torque coefficients shows each aerofoil has its own optimum tip speed ratio and torque coefficient magnitude. This influence of the aerofoil becomes more evident with the increase in the number of blades. For instance, for the one-bladed turbine, see Fig.5.7(a), the NACA0015, NACA0018 and NACA0021 aerofoils have an optimum tip speed ratio $\lambda = 3$; for the three-bladed turbine, the NACA0021 and NACA0018 produced a maximum torque coefficient at $\lambda = 2.25$ and the NACA0015 at $\lambda = 2.5$.

The NACA0021 was the aerofoil with the best total torque coefficients of all the aerofoils and the number of blades evaluated. The difference with the other aerofoils before its optimum torque coefficient (low tips speed ratios) is attributed to the fact that the NACA0021 presents some positive torque coefficients upstream at low tip speed ratios; thus, despite having very similar upstream torque contributions with other aerofoils, the downstream contribution results are beneficial for the overall torque coefficients.

At high tip speed ratios, after the optimum torque coefficient, the NACA0012 aerofoil shows the largest torque coefficient (despite being a small increase), followed by the NACA0015, NACA0018, NACA2418, NACA0021 and last is the S1210 aerofoil for all the number of blades investigated. This better performance of the NACA0012 at large tip speed ratio is attributed to its better downstream contributions than the other aerofoils as explained previously in this section.

In order to understand the influence of the aerofoil profile on the power coefficient, C_P, this parameter is included in Fig. 5.8(a-c). The analysis of C_P has revealed that at the optimum operating conditions, the magnitude of the power coefficient is very similar among the symmetrical aerofoils. For the one-bladed turbine, the optimum power coefficient was $C_P = 0.47$, and this was obtained for a tip speed ratio $\lambda = 3.5$ for the NACA0021 and NACA0018; the NACA0015 aerofoil shows an optimum $C_P = 0.48$ at $\lambda = 4$ and the NACA0012 aerofoil produced an optimum $C_P = 0.49$ at $\lambda = 4$. For the two-bladed turbine, the NACA0012 shows an optimum power coefficient $C_P = 0.42$ at the tip speed ratio $\lambda = 3.5$; the NACA0015 aerofoil produces $C_P = 0.44$ at $\lambda = 3$ and NACA0018, NACA0021 produces $C_P = 0.44$ at $\lambda = 2.75$. Moreover, for the three-bladed turbine, an optimum power coefficient $C_P = 0.38$ at the tip speed ratio $\lambda = 2.5$ was obtained for the NACA0021 and NACA0018; the NACA0015 produced $C_P = 0.38$ at the tip speed ratio $\lambda = 2.75$ and the NACA0012 shows $C_P = 0.35$ at the tip speed ratio $\lambda = 3$.

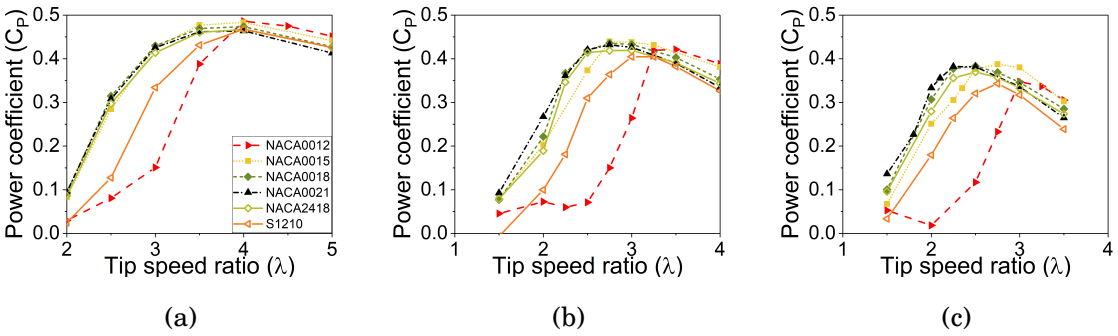

Figure 5.8: Power coefficient as a function of the tip speed ratio for the six aerofoils for the six aerofoils for a VAWT with (a) one blade, (b) two blades and, (c) three blades.

Despite a similar optimum power coefficient among the aerofoils, at low tip speed ratios, the influence of the aerofoil shape on the power coefficient magnitude becomes substantial. In contrast, at high tip speed ratios, the influence of the aerofoil profile is minor and the thinner aerofoil NACA0012 produces the best power coefficient; this is followed by the NACA0015, NACA0018, NACA2418, NACA0021 and last S1210.

5.4.1 Dynamic stall regime

The dynamic stall phenomenon has been shown to play the most important role in the poor torque coefficient that is observed at low tip speed ratios before an optimum total torque coefficient is observed as explained above. The most quantifiable parameter in the dynamic stall phenomenon is the stall-inception, and thus this parameter is analysed here. This stall-inception point represents the moment when the bubble that occurs near the leading edge of the aerofoil collapses and a vortex near the leading edge starts to move downstream along the aerofoil chord. This moment can be recognized by the moment when a minimum pressure coefficient is reached [95, 46]. In addition, the stall-inception instance is the most critical parameter that describes the dynamic stall process as discussed in Chapter 4. The pressure coefficient is calculated as follows:

$$P_{coeff} = \frac{P_s - P_\infty}{1/2\ \rho V_{rel}^2} \tag{5.1}$$

To understand the importance of the stall-inception (θ_{in}), the three-bladed VAWT at the tip speed ratio 1.5 was selected for a rigorous analysis. This case has been selected since the three-bladed turbine represents the most practical design. For the six aerofoils, upstream of the rotor, the calculated azimuthal angle where a minimum in the pressure coefficient is observed is included in Table 5.2 . Also, the azimuthal torque coefficient for the same case is included in 5.9 for the six aerofoils as a piece of complementary information in order to better understand the dynamic stall regime.

Table 5.2: Azimuthal angle with a minimum in the pressure coefficient and azimuthal angle with a maximum in the torque coefficient for the six aerofoils of a 3 bladed-turbine and $\lambda = 1.5$

.

	NACA0021	NACA0018	NACA0015	NACA0012	NACA2418	S1210
θ_{max} (°)	76.88	76.77	66.50	58.75	75.76	75.76
θ_{in} (°)	78.87	77.91	65.51	56.53	75.64	74.68

The azimuthal angle corresponding to the stall-inception point (θ_{in}), see Table 5.9, shows the largest delay in the inception angle being produce by the NACA0021 and the second was the NACA0018 aerofoil with $\theta_{in} = 78.87°$ and $\theta_{in} = 77.91°$, respectively.

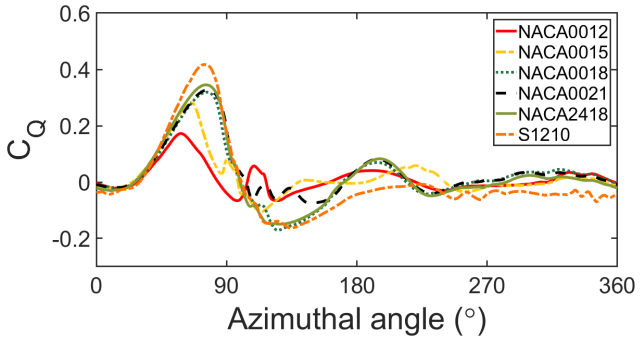

(a)

Figure 5.9: Instantaneous torque coefficient for a three blades turbine and a tip speed ratio 1.5

The aerofoils, NACA2418 and S1210, produce a stall-inception at the azimuthal angle $\theta_{in} = 75.64°$ and $\theta_{in} = 74.68°$, respectively. The smaller stall-inceptions are shown by the NACA0015 with $\theta_{in} = 65.51°$ and the last by the NACA0012 aerofoil with $\theta_{in} = 56.53°$. An interesting observation was that the stall-inception angles were located at very similar azimuthal angles where the torque coefficient presents a maximum value, θ_{max} before there is a sudden loss in $C_Q(\theta)$ occurs.

Upstream, the four aerofoils, NACA0021, NACA0018, NACA2418 and S1210 with similar stall-inception angles show a loss in the torque coefficient in Fig. 5.9 at similar azimuthal angles but the magnitude of the azimuthal torque coefficient is different. As observed previously in the torque coefficient analysis upstream of the rotor in Fig. 5.5, the largest torque coefficient was observed for the S1210 and NACA2418. This torque coefficient produced by the S1210 and 2418 aerofoils upstream is explained due to the high lift force, C_L at positive angles of attack for these aerofoils that influence the tangential force coefficient produced by the blades according to Eq. (3.19).

In Fig. 5.10 (a-c), the coefficients of the static lift, drag and tangential force generated for the investigated aerofoils are compared in the range of angle of attack (AOA) experienced by the turbine. The S1210 aerofoil presents the largest lift force coefficient, C_L. The NACA2418 shows a minor increase in C_L in regards to the symmetrical aerofoil NACA0018 at positive angles of attack. The chordwise force coefficient, C_C that

relates the lift and drag force coefficients according to Eq.(4.3), allows a better understanding of the aerofoil influence. The S1210 aerofoil presents the largest chordwise force coefficient at positive angles of attack, followed by the NACA2418 and the last are the symmetrical NACA aerofoils.

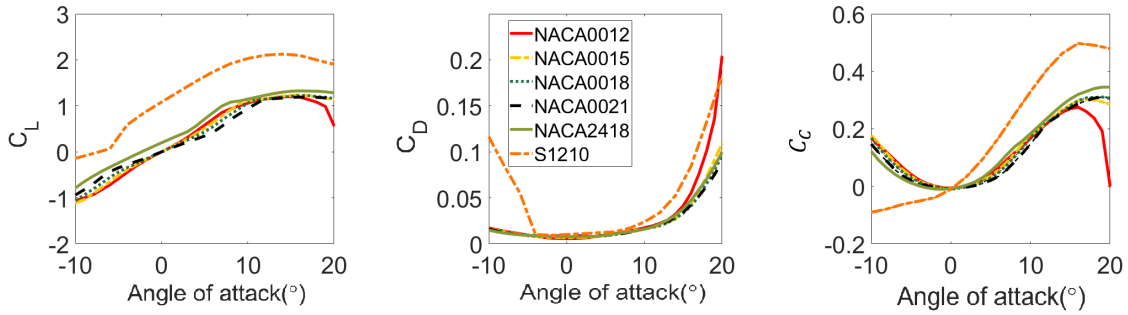

(a) (b) (c)

Figure 5.10: Static force coefficient as a function of the angle of attack for the six aerofoils calculated by using Xfoil at Reynolds number of 5×10^5 (a) Lift force coefficient (C_L), (b) drag force coefficient (C_D), and (c) chordwise force coefficient (C_C)

Despite the symmetrical aerofoils show similar static tangential force coefficient in Fig. 5.10(c), the dynamic stall-inception point occurs earlier for the NACA0012, followed by the NACA0015 and later by the NACA0018 and NACA0021. Consequently, this explained the sooner loss in C_Q for the NACA0012 at the upstream according to Fig. 5.9 and also explained why the NACA0012 exhibits the poorest torque coefficient in Fig. 5.5(c).

The present results suggest that under dynamic stall conditions, the primary parameter that controls the torque coefficient is the stall-inception; larger is this angle, then larger is the torque contribution upstream. In addition, if the aerofoil exhibits a high tangential force, i.e. high lift/drag ratio, then there is observed to be an improvement in the torque coefficient upstream, such as in the S1210 that presents a similar stall-inception as the NACA0018 and NACA0021 but with a larger upstream torque coefficient.

The dynamic stall upstream of the rotor produces a vortex released by the blades

at downstream of the rotor and this induces high disturbances to the flow field downstream of the blade. The flow field at downstream of the rotor is also affected by the blockage effect due to the number of blades and the tip speed ratio. To visualize the vortex formation on the blades, then the vorticity contours become much more useful in the understanding of the dynamic stall phenomenon and this is presented in Fig. 5.11.

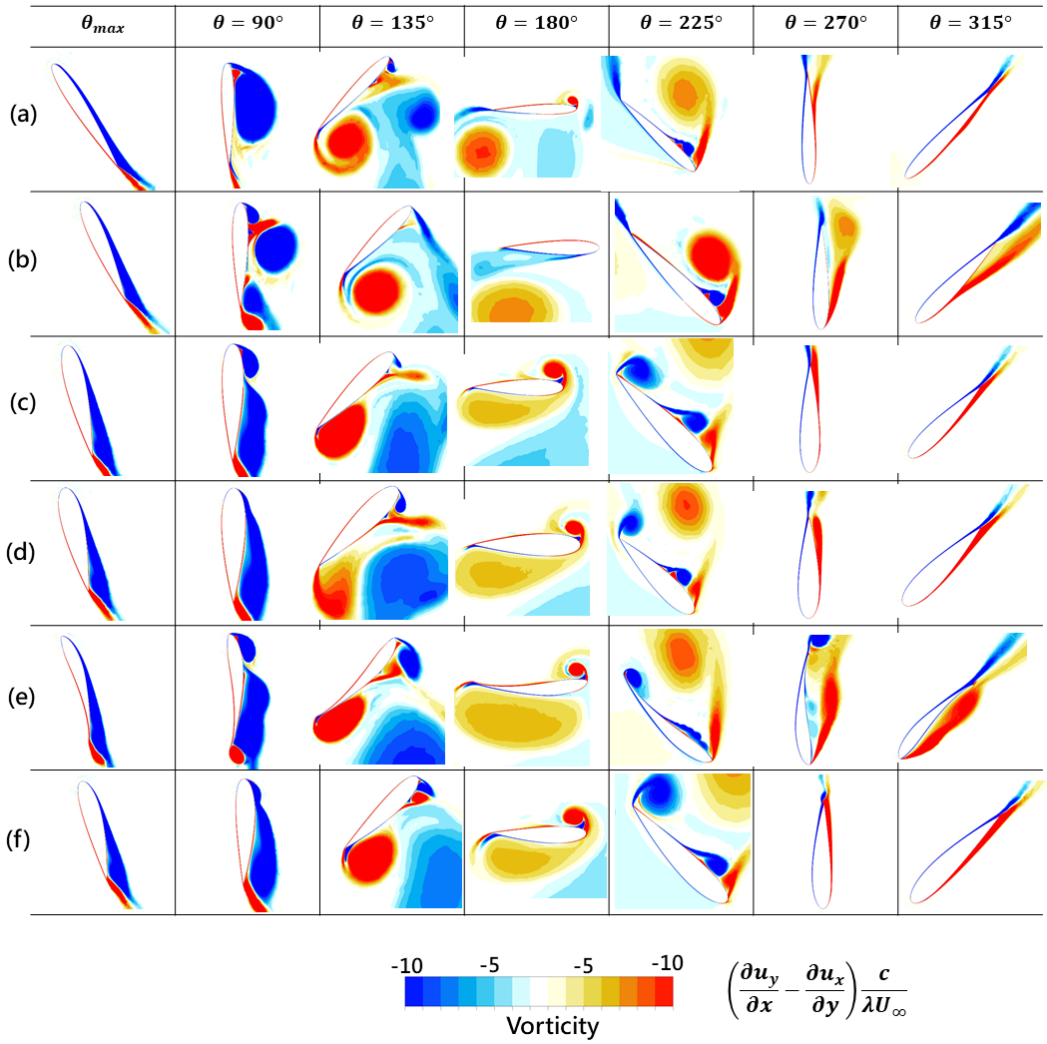

Figure 5.11: Vorticity contours of the flow field around the blade of a three-bladed turbine at $\lambda = 1.5$ in the downstream region of the rotor of the three-bladed turbine: (a) NACA0012, (b) NACA0015, (c) NACA0018, (d) NACA0021, (e) S1210 and (f) NACA2418.

Figure 5.11 illustrated the instants when the blades are located downstream of the rotor at three azimuthal angles, $\theta = 225^\circ$, $\theta = 270^\circ$ and $\theta = 315^\circ$ At the azimuthal angle $\theta = 225^\circ$ the S1210 aerofoil presents the largest separation. A separated boundary layer is indicative of a loss in lift force coefficient and an increase in the drag force coefficient [44], and this agrees with the force coefficient observation in Fig. 5.10 at the negative angles of attack for the S1210, where low C_L and large C_D are observed. In addition, at the azimuthal angles $\theta = 270^\circ$ and $\theta = 315^\circ$ the S1210 aerofoil presents the largest separation. Then, this suggests that the cambered S1210 does not have the same beneficial characteristics observed at positive (upstream) AOA when it is at negative angles of attack (downstream), and this is the reason why its total torque coefficient for all the range of tip speed ratios and solidities investigated did not performed better than the NACA0021 and NACA0018 aerofoils.

The vorticity contours illustrated in Fig. 5.11, indicate that at the azimuthal angle $\theta = 225^\circ$ the NACA0021, NACA0018 and NACA2418 show the presence of two small vortices (opposite in the rotational direction) attached to the surface of the leading edge of the aerofoil. Moreover, at $\theta = 270^\circ$ and $\theta = 315^\circ$, the aerofoils NACA0021 and NACA0018 show the most extended attached flows on the surface of the aerofoil. Therefore, as in the upstream region, the symmetrical aerofoils NACA0021 and NACA0018 have the largest delay in the dynamic stall, and downstream it has still the capabilities to maintain their boundary layers to be attached. The cambered NACA2418 shows that it has as good stalling capabilities downstream as upstream, and overall its torque coefficient remains similar to the NACA0018.

The NACA0012 aerofoil under dynamic conditions is the worst of the aerofoils investigated because the stall occurs too early upstream, and hence the secondary vortex (the peak in the torque coefficient at $\theta = 100^\circ$ in Fig. 5.11) is released downstream of the VAWT, and as a results the torque contribution downstream is minimal. Therefore, aerofoils in which the stall-inception occurs earlier are not recommended at low tip speed ratios since the dynamic stall upstream and downstream are stronger.

5.4.2 *Fully unsteady attached regime*

The regime called fully unsteady attached regime has been observed to be located after a maximum in the total torque coefficient is experienced. The optimum torque coefficient takes place at different tip speed ratios and depends on the aerofoil profile and the number of blades, hence, the range of tip speed ratios under a fully attached regime (high tip speed ratio) also depends on the number of blades and the aerofoil profile. In this section, two cases with all the aerofoils behaving under the fully attached regime are exemplified. Fig. 5.12(a) includes the azimuthal torque coefficient for a two-bladed turbine at a tip speed ratio $\lambda = 4$ and 5.12(b) includes the azimuthal torque coefficient for a three-bladed turbine at $\lambda = 3.5$.

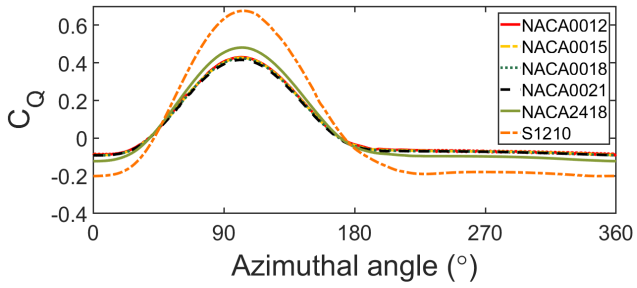

(a)

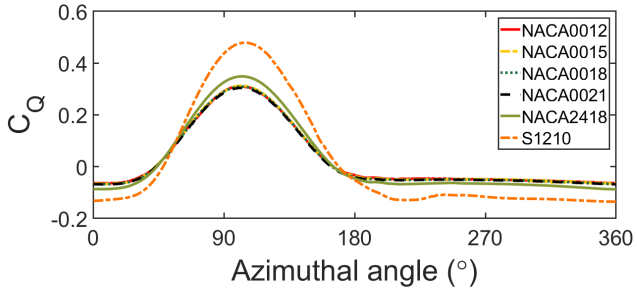

(b)

Figure 5.12: Azimuthal torque coefficient for the six aerofoils with (a) two blades and a tip speed ratio 4, and (b) three-blades and tip speed ratio 3.5

It is observed in Fig. 5.12(a-b) that the S1210 (cambered 6%) aerofoil produces a large torque coefficient upstream but also the largest negative torque coefficient down-

stream for both number of blades. The NACA2418 (cambered 2%) improved the torque coefficient upstream compared with the symmetrical NACA0018 but also produced a more negative torque coefficient downtream than the NACA0018 aerofoil. Therefore its total torque coefficient is very similar to the symmetrical aerofoil.

Under this high tip speed ratio regime, the total torque coefficient depends on the lift and drag force coefficients generated for each aerofoil under the attached flow. Despite the upstream contributions producing a positive torque coefficient for all the aerofoils, under this regime, the negative torque coefficient produced by all the aerofoils downstream is the factor that is more detrimental to the total torque coefficient and this becomes worst with the further increase in the tip speed ratio. The downstream torque coefficients previously presented in Fig. 5.6, shows that the aerofoil NACA0012 has the least negative torque contribution with the increase in the tip speed ratio.

In order to gain more details to understand the poor torque coefficient at downstream of the rotor, the deficit in the velocity is analysed in Fig. 5.13. Fig. 5.13 (b-d) shows the velocity distribution downstream of the rotor at a distance of one diameter from the rotation centre. It can be seen that the wind speed decreases dramatically when increasing the tip speed ratio. For a three-bladed turbine at a tip speed ratio $\lambda = 1.5$, it is known that the dynamic stall phenomenon is severe, despite that the deficit in the downstream velocity (V/V_∞), see Fig. 5.13(b), is less severe than the deficit for the tip speed ratio $\lambda = 3.5$ where the non-stall conditions are present, see Fig. 5.13(b) and (c). This deficit is explained by the appearance of the blades as a solid disk when rotating fast, thus the interference factor increases and this leads to a dramatic reduction in the magnitude of the velocities. Fig. 5.13(d) compares the velocity deficit, (V/V_∞) for a three-bladed turbine with the NACA0021 at a tip speed ratio with a dynamic stall ($\lambda = 1.5$), at the optimum torque coefficient ($\lambda = 2.25$) and two tip speed ratios far away from that of the dynamic stall ($\lambda = 2.5$ and $\lambda = 3.5$). At the optimum torque coefficient, it is observed that the velocity downstream decays by more than 75% and similar decays are observed at higher values of λ.

Therefore, under the high tip speed ratios, in addition to the decrease in the angle of attack due to the increase in the blade speed, the interference factor may cause a further decrease in the angle of attack, in the relative velocity and then in the Reynolds

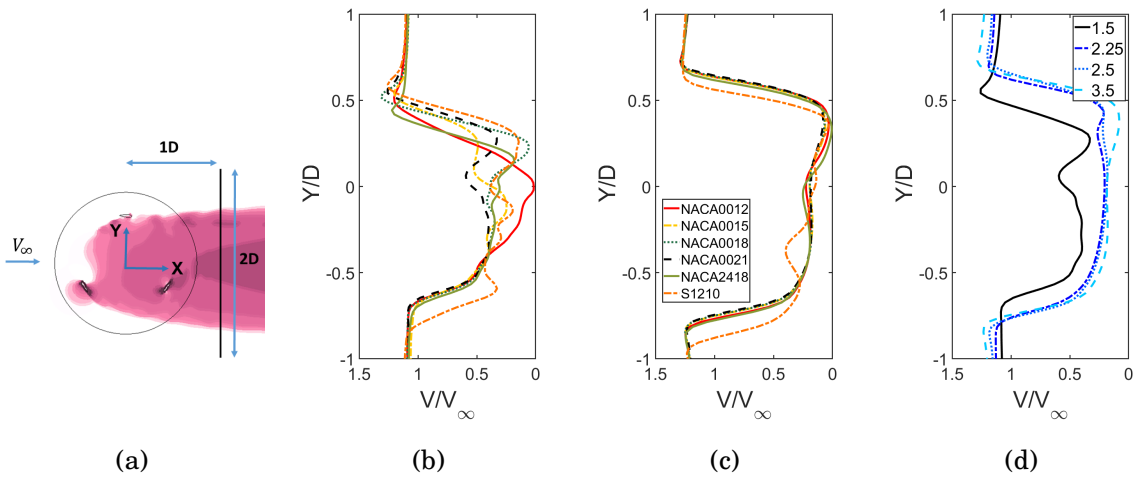

Figure 5.13: (a) Diagram representation along the vertical line where the velocity was collected for a three-bladed VAWT; Non-dimensional velocity V/V_∞ for the six aerofoils at (b) $\lambda = 1.5$, (c) $\lambda = 3.5$, and (d) Non-dimensional velocity for the NACA0021 aerofoil at four tip speed ratios.

numbers. The reduction of the angle of attack in the downstream of the rotor due to the increase of the number of blades has been observed in [93]. The deficit in the downstream velocities are further explained in Chapter 7 in order to understand the effect of the number of blades and tip speed ratio in the reduction of the torque coefficient at downstream of the rotor.

At high TSRs, the blade AOA tends to be small in the downstream region as explained previously. At small AOA, $\sin -\alpha \approx -\alpha$ and, $\cos(-\alpha) \approx 1$, hence the tangential force coefficient approximates to $C_T \approx \alpha C_L - C_{DO}$. Therefore, the smaller the angle of attack, the drag coefficient of the aerofoils at around zero angles of attack becomes more important, and this means the thinner the aerofoil then the smaller the drag coefficient at zero angle of attack. This explains why the NACA0012 aerofoil is the aerofoil with the least negative torque coefficient with the increase in the tip speed ratio downstream of the rotor.

The case of the cambered aerofoil S1210 that presents some small positive lift force coefficients at negative angles of attack and an increase in the drag coefficient at these negative angles of attack (see Fig. 5.10), the first term αC_L becomes negative and this

may increase the negative magnitude in the torque coefficient downstream. This is also confirmed in Fig. 5.10 (c) where the chordwise force coefficient for the six aerofoils is compared at negative angles of attack, the worst tangential force is observed with the S1210 and the best for the NACA0012.

5.5 Discussion

The present analysis in the VAWTs including a combination of different number of blades, 4 symmetrical aerofoils and two cambered aerofoils, and a wide range of tip speed ratios has highlighted the most beneficial aerodynamic characteristics of the aerofoil profiles at different tip speed ratios. In addition, the analysis gives a basis to re-think the design of aerofoils that are applicable for VAWTs.

From the results of this chapter the most interesting finding is the role of the downstream torque contribution in the total torque coefficient. All the aerofoils, and all the number of blades investigated here found with the increase of the tip speed ratio a more negative torque that overall, causes a reduction on the VAWT performance and, overcomes the positive torque coefficient produced at upstream of the rotor for all the aerofoils. Therefore, despite some aerofoils produced very good lift/drag relation at positive angles of attack, at negative angles of attack the poor relation lift/drag impact negatively in the performance of the VAWT. As a result, more attention is required at negative angles of attack in order to obtain an aerofoil profile that produced good lift force coefficient and low drag force coefficient. Under this subject, at negative angles of attack, the symmetrical aerofoils since are expected to present the same aerodynamic characteristics than at positive angles of attack, then may found a huge amount of available information [116]. Different, other geometrical aerofoils, cambered, slotted, with flap, with trailing edge modification, etc, have been very rare investigated at negative angles of attack and then, more future investigation is required [117, 118, 112].

These results have shown that the cambered aerofoil may improve the power coefficient under some tip speed ratios. For example, the S1210 possess 6% of camber and 12% thickness and compared with the NACA0012 with 0% camber and 12% thickness, produces a larger torque coefficient than the NACA0012 since it has a larger stall-onset

angle upstream and a high lift force coefficient. Only at tip speed ratios corresponding to the optimum operating conditions of the NACA0012, this last aerofoil performed better than the cambered S1210. This observation is in agreement with results presented in [27] where the NACA0012 and cambered NACA5512 and NACA7512 were compared in the power coefficient; both cambered aerofoils present a better performance at low tip speed ratios, where the NACA0012 showed poor performance. In contrast, the NACA2418 with a 2% camber and 18% thickness offer no advantages compared with the symmetrical NACA0018 with 0% camber and 18% thickness. The pointless use of a small percentage-camber of a thick aerofoil was also observed in [119]. In this mentioned investigation, the NACA$63_4$221 aerofoil with 1.1 camber and 21% thickness was compared with the NACA0021; the power coefficient as a function of the tip speed ratio was very similar but in the optimum tip speed ratio, the symmetrical aerofoils performed slightly better than the cambered aerofoil. This agrees with our results by using the NACA2418 and the NACA0018 aerofoil. In [120] a similar conclusion was obtained by using the symmetrical NACA0022 and the camber NACA5522, both with 21% thickness.

Therefore, if the camber percentage improves the delay in the stall angle compared with its symmetrical aerofoil, then some improvement maybe notice at tip speed ratios where dynamic stall occurs. Nevertheless, if the cambered aerofoil has a poor lift force coefficient and large drag force coefficient at negative angles of attack then this can have a detrimental effect on the performance, mainly at high tip speed ratios. While an increase in the magnitudes of the wind velocity downstream at high tip speed ratios is almost impossible, the control in the angle of attack needs to be investigated as a possible strategy to reduce the negative torque production downstream of the rotor. Present results solves the controversy existing in the last few years in the use of cambered over the symmetrical. For instance, some authors claim that cambered aerofoils are promising for VAWTs; others have predicted that it is detrimental for their performance [120, 121, 27, 122, 123]. The results in this Chapter suggest that more than focusing the investigation on the use of cambered or symmetrical aerofoils attention need to be paid in the final aerodynamic characteristics, i.e, the stall-onset and the lift and drag force coefficient at positive and negative angles of attack.

In addition, the results presented have shown that independent of the number of blades the dynamic stall region always take place, thus, in order to increases the torque under the dynamic stall conditions, the dynamic stall-inception of the aerofoil needs to be considered when selecting the aerofoil. The stall-inception point is also known as the stall-onset angle and under dynamic conditions, the most evaluated aerofoils have been symmetrical [65] but some cambered aerofoils have been tested under dynamic conditions and at positive angles of attack [124]. In the present results, the larger dynamic stall inception was shown by the NACA00021, then followed by the NACA0018 and this agrees with the experimental investigation on stall-onset angle under dynamic conditions in [65].

Despite the optimum tip speed ratios differing among the aerofoils and the number of blades, under the optimum operating conditions the symmetrical NACA aerofoils present very similar optimum power coefficients. In addition, after the dynamic stall region, where the flow over the blades is fully attached, huge attention needs to be paid to the performance of the aerofoil under negative angles of attack and low Reynolds number, since the downstream torque contribution plays a significant role in the reduction of the total torque coefficient.

5.6 Summary

The key new information identified in this chapter would allow an analysis of the dynamic stall method to predict the unsteady forces under dynamic stall conditions and fully attached regimen and to assess the DSMT model and its capabilities to take into account the effect of the number of blades under both regimes. Simulations performed in this Chapter has bridged the existing gap in the literature regarding the influence of the upstream and downstream torque contributions on the overall performance of VAWTs. Some of the most important findings are described as following.

(i) When the dynamic stall occurs at upstream of the rotor as well as the downstream of the rotor the lowest is the total torque coefficient. After the optimum torque coefficient, a fully attached flow regime occurs and it has been demonstrated that the decrease in the total torque coefficient is attributed mainly to the downstream region

of the rotor.

(ii) The symmetrical aerofoils NACA0015, NACA0018 and NACA0021 have been demonstrated to be the most effective both upstream and downstream of the rotor. Thus, these aerofoils are further investigated in this thesis. The cambered aerofoil, despite showing some advantages, requires to be optimized in order to work well at negative angles of attack, otherwise, this will cause a significant negative torque downstream that limit the overall power coefficient of the VAWT.

(iii) Under dynamic stall conditions, the most important parameter is the stall-onset angle that is highly dependent on the aerofoil. Under the fully attached regime, the downstream torque contribution becomes critical and hence the more negative its value the larger is the depletion in the VAWT performance. Therefore, the lift/drag relation at negative angles of attack need to be carefully investigated during the selection of the aerofoils profile if large tip speed ratio becomes the range of interest for the VAWT under operation.

(iv) The generated knowledge would assist in the assessment of the LB dynamic stall and the DMST to predict the torque coefficient on VAWTs and that is carried out in Chapter 6.

Chapter 6

Predicting unsteady loads using a dynamic stall algorithm

6.1 Overview

The Leishman-Beddoes dynamic stall algorithm has been used the most to predict the unsteady loads of oscillating aerofoils. Additionally, the existing investigations have been focused on Reynolds number larger than 1 million and therefore, most of the empirical parameters that this dynamic stall model requires are restricted to a few aerofoils and high Reynolds number. As was discussed in previous Chapter, the dynamic stall phenomenon takes place before the optimum tip speed ratio of any turbine and its modelling results crucial for an accurate prediction of the torque coefficient in the VAWTs. Under this subject, still remain a need of a detailed analysis of the use of this LB dynamic stall algorithm to predict the performance of VAWTs, specifically, the implementation of the Kirchhoff flow model and the estimation of the stall-onset at low Reynolds number that is likely to be found in VAWTs operating at low tip speed ratios and low wind speeds. This chapter bridges these gaps in the literature and additionally evaluates the effectiveness of the double multiple streamtube to predict the torque coefficient of VAWTs under the dynamic stall and a fully attached regime of operation.

6.2 The Leishman-Beddoes dynamic stall: modifications

The Leishman-Beddoes dynamic stall (LB) algorithm is based on the physics of the dynamic stall phenomenon described in Section 2.2.2. It predicts the unsteady loads under the fully attached regime; next, it computes the stall-onset angle and finally, calculates the unsteady loads under the separated flow regime, see Section 3.3. Some

of the aspect of the LB model that requires a depth analysis before its application are described in the consecutive sections.

6.2.1 Time delay constant database

The stall-onset module of the Leishman-Beddoes method has the objective to predict the stall-inception. At this point, a minimum value in the leading edge pressure occurs, this is the critical instant when the circulation that is accumulated at the leading edge of the aerofoil (LE) is released downstream and this rolls up to form a vortex which increases in size with its movement along the chord. This vortex is called the detached separated vortex (DSV) and the stall-inception is the most critical parameter for an accurate representation of the dynamic stall phenomenon.

In order to predict accurately the dynamic stall inception, the Leishman-Beddoes method is based on the time delay method. This method is able to predict the stall inception from the static aerofoil data [114, 44] and uses a non-dimensional time (refers as a time delay constant) which may be expressed as follows:

$$T_r = \frac{2U_{ref}\Delta t_{sep}}{c} \tag{6.1}$$

where Δt_{sep} represents the time elapsed from the static stall angle, α_{ss}, to the dynamic stall-onset angle α_{os}, then $\Delta t_{sep} = (\alpha_{os} - \alpha_{ss})/\dot{\alpha}$.

Previous investigations have calculated the time delay constant, T_r, using experimental test consisting on oscillating aerofoils and ramp-up tests [46, 65]. Despite that, the available T_r values are restricted to high Reynolds numbers and then, the need to understand this parameter at low Reynolds number has been investigated as follows.

In the analysis carried out in Chapter 4, corresponding to the stall-onset angle in VAWTs and the operating parameters that affects its value, surprisingly the stall-onset was found to have a linear relationship with the non-dimensional pitch rate, $q = \frac{\dot{\alpha}c}{2U_{ref}}$ calculated when the angle of attack approaches to the static stall angle, α_{ss}. This linear relation was obtained at each tested Reynolds number as observed in Fig. 6.1 (a) for the NACA0015 and following same procedure described in Chapter 4 then, the stall-onset as a function of q was obtained for the NACA0018 and NACA0021 as illustrated

in Fig. 6.1(b) and (c) respectively. The slope of the linear adjustment of the graphs presented in Fig. 6.1 at each Reynolds number give the expression:

$$m = (y - b)/x \tag{6.2}$$

where, m, y, b and x are the variables representing a typical linear equation. The slope m given by Eq.(6.2) produces $m = (\alpha_{os} - \alpha_{ss})/q$ and substituting the definition of the non-dimensional pitch rate q given by Eq. (4.2) then m results to be the time delay constant, T_r.

The values of T_r are calculated for NACA0015, NACA0018 and NACA0021 aerofoils at the corresponding Reynolds numbers included in Table 6.1. The results presented in Table 6.1 showed that the time delay constants for each aerofoil changes with the Reynolds numbers within the range of Re investigated. It was found that T_r increases with the increasing Reynolds number; for the NACA0015 aerofoil T_r varies within a range of 4.28-5.70, and for the NACA0018 aerofoil then T_r changes between 3.45 and 6.35.

The influence of Re on the time delay constant for the NACA0021 is less pronounced compared with the other two aerofoils, being in the range of 5.58-6.78. In addition, the NACA0021 showed the largest value of T_r for all the Re values investigated, but, at $Re = 3.3 \times 10^5$ both the NACA0018 and NACA0021 showed a very similar value of T_r.

The present results then suggest that the NACA0021 may persist attached under larger angle of attacks than the other two aerofoils. Moreover, the similar values of the time delay observed in the range of Re tested for the NACA0021 suggests that this aerofoil is less affected by the decrease in the Reynolds numbers, i.e. it is appropriated to operate at low wind speeds.

The time delay constants calculated by Sheng et al. using experimental data for large Reynolds number of 1 million were as follows: for the NACA0015 , $T_r = 5.78$, for the NACA0018 $T_r = 6.22$ and for the NACA0021 $T_r = 6.30$. These values are similar to the time delay values found with present simulations at $Re = 3.3 \times 10^5$ (the largest tested considered) for each aerofoil according to Table 6.1. This suggests that, after $Re = 3.3 \times 10^5$, the Reynolds number has a minor effect on the time delay constant.

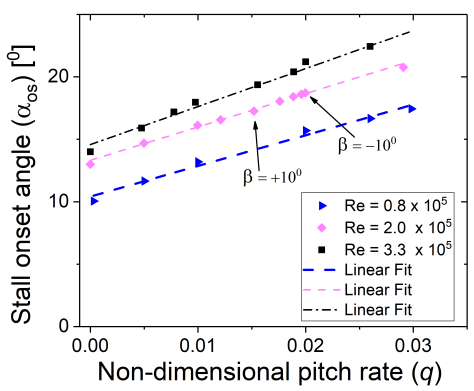

(a)

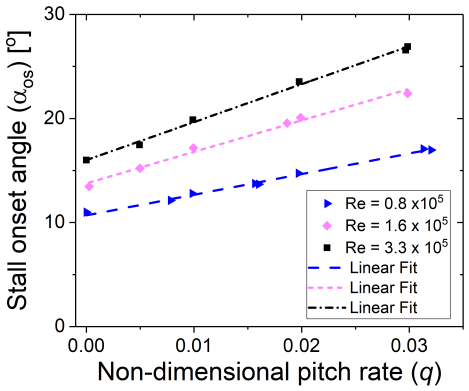

(b)

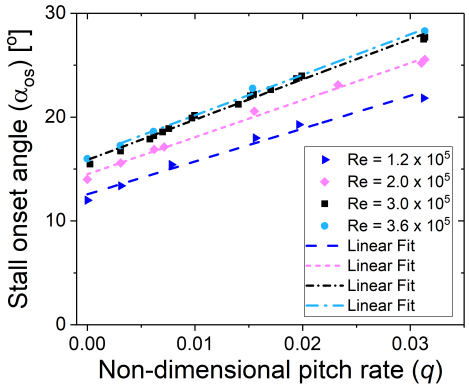

(c)

Figure 6.1: Stall-onset angle as a function of the non-dimensional pitch rate for (a) NACA0015, (b) NACA0018 and, (c) NACA0021.

However this observation needs further verification with experimental data.

6.2.2 Kirchhoff flow equation: Static parameters

In order to replicate the unsteady forces, the LB dynamic stall method requires some empirical parameters that are obtained usually using the static lift force coefficient and are specific for each aerofoil and Reynolds number. The LB method is assisted by the Kirchhoff flow model to obtained these empirical parameters and one of the issues

Table 6.1: Predicted time delay constant at different Reynolds number.

Aerofoil	Re	T_r
NACA0015	0.8×10^5	4.28
	2.0×10^5	4.64
	3.3×10^5	5.70
NACA0018	0.8×10^5	3.45
	2.0×10^5	5.28
	3.3×10^5	6.35
NACA0021	1.2×10^5	5.58
	2.0×10^5	6.03
	3.0×10^5	6.73
	3.6×10^5	6.78

found when applying the Kirchhoff flow model is discussed here as follows.

The Kirchhoff flow model has been widely used in order to generate the static lift force coefficient based on the trailing edge separation of the turbulence boundary layer (f) and reads:

$$C_L(\alpha) = C_{L\alpha}(\frac{1+\sqrt{f(\alpha)}}{2})^2(\alpha) \tag{6.3}$$

where C_L corresponds to the lift coefficient at each angle of attack, and $C_{L\alpha}$ is the slope of the lift force coefficient under the fully attached regime. The Kirchhoff flow model was proposed for thin flat plates merged into a potential flow, but despite this, Eq. (6.3) has been used successfully on aerofoil profiles for many years to approximate both the location of the separation point and the lift force coefficients [125, 8, 115]. The Equation (6.3) that relates the lift force coefficient with the separation of the boundary layer is able to take into account the viscosity of the air under the full-attached flow regime, the thickness, the camber and the flow deflection. A more in-depth discussion of the Kirchhoff model maybe found in [8].

The Kirchoff flow model explains that with the increase of the angle of attack the

separation point (f) at the trailing edge of the aerofoil moves towards the aerofoil leading edge; a value of $f = 1$ means the boundary layer is fully attached and a value of $f = 0$ means the boundary layer is fully separated, see Figure 6.2(a). It has been observed that while the separation point moves towards the LE with the increase of the angle of attack, the lift force coefficient starts to deviate from its linear trend until it reaches a maximum value and immediately after the lift force coefficient drops suddenly, i.e. stall occurs, see Fig. 6.2(b). In addition, at this point a minimum in the pressure coefficient has been observed.

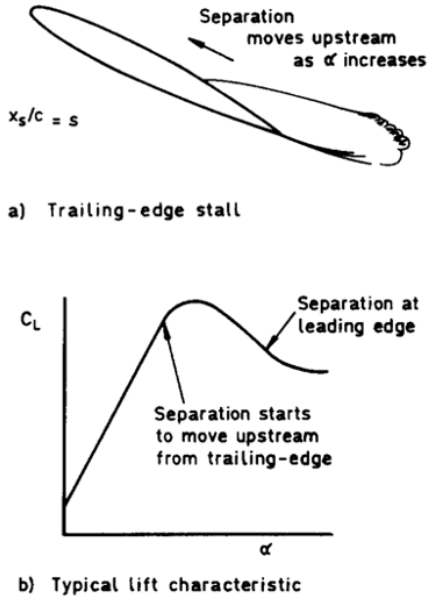

(a)

Figure 6.2: Effect on lift force coefficient due to the trailing edge separation (f) [8]

According to previous investigations, a mathematical expression of the trailing edge separation f as a function of the angle of attack has been proposed based on the analysis of f using several aerofoils. The following expression has been proposed to represent this behaviour under static conditions [48]:

$$f(\alpha) = \begin{cases} (1 - f_{crt}) \exp(\frac{|\alpha| - \alpha_{ss}}{S_1}), & |\alpha| < a_{ss} \\ f_{LE} + (f_{crt} - f_{LE}) \exp(\frac{\alpha_{ss} - |\alpha|}{S_2}), & |\alpha| \geq a_{ss}. \end{cases} \tag{6.4}$$

where f_{LE} represents the point around the leading edge where the boundary layer separates at larger angles of attack; f_{crt} represents the critical separation point where the lift coefficient reaches its maximum value, i.e. at the angle of attack where the static stall occurs, α_{ss}. A value of $f_{crt} = 0.6$ or 0.7 has been usually associated with α_{ss} and after this value, the flow is considered as a separated flow. The critical separation point $f_{crt} = 0.6, 0.7$ has been proposed for high Reynolds numbers, and in order to apply this value with confidence a more in-depth assessment of the separation point f is mandatory. Therefore this parameter is further discussed later in this section. The parameters S_1 and S_2 are the adjusted parameters in Eq. (6.4) with the experimental data of f as a function of the angle of attack and this depends on the Reynolds number.

It is important to mention that Eq. (6.4) has been formulated based on several experimental tests and through the years several different formulations have been proposed. Formulations that are more complex and requires a larger number of empirical parameters are found in [126].

The critical separation point

Due to the shortage of literature about the static separation point f as a function of the angle of attack at Reynolds number lower than one million and being the interest of this thesis, therefore the analysis of the actual f at two Reynolds number as been carried out using the NACA0015 aerofoil. The numerical technique used for these simulations is included in Section 3.2.2.

The trailing edge separation point, f, has been calculated by using the skin friction (C_{fx}) along the aerofoil chord and selecting a value of $C_{fx} = 0$ as the criteria to define the separation point. In addition, the lift force coefficient has been calculated for each angle of attack and the comparison of both these parameters is included in Fig.6.3 at two Reynolds numbers.

Figure 6.3(a) presents the results for a Re of 3.3×10^5. At this Re, the maximum lift

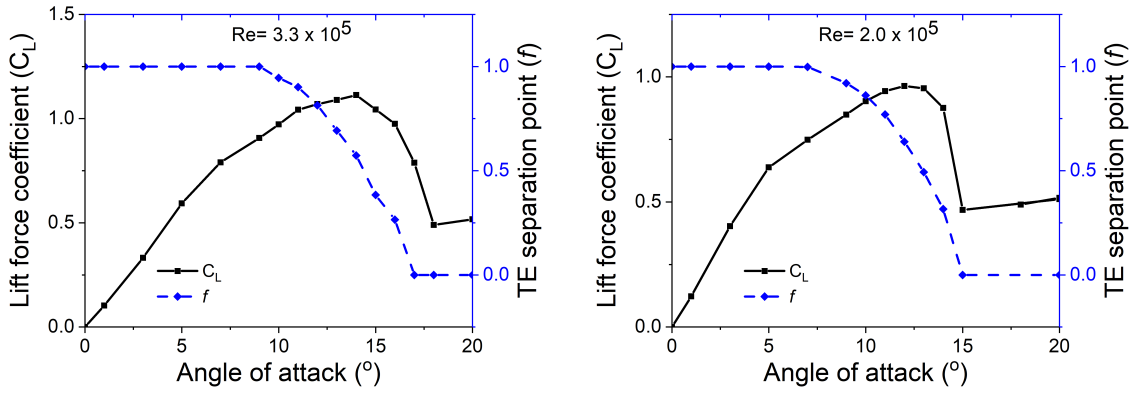

Figure 6.3: Trailing edge separation point as a function of the angle of attack calculated with the skin friction being obtained using CFD simulations for the NACA0015 under static conditions at (a) Re 3.3×10^5 and (b) 2.0×10^5

force coefficient ($C_{L,max}$) occurs when $f_{crt}=0.53$ and $\alpha_{ss}=14°$. A fully attached boundary layer with $f=1$ is observed up to $\alpha=9°$. In the case of Re 2.0×10^5, Fig. 6.3(b), the maximum lift force coefficient occurs when $f_{crt}=0.50$ at $\alpha_{ss}=13°$. Additionally, at this Re a value of $f=1$ is observed up to $\alpha=7°$. According to these results a critical separation point of $f_{crt}=0.5$ is recommended to be used in Eq.(6.4) at these low Reynolds number. The assessment of the using this value is presented in following paragraphs. The value of the separation point, f_{LE} under a larger angle of attack was found to be around 0.02 for both Reynolds number.

The separation of the boundary layer, f, also permit the prediction of the chordwise force coefficient by using next relations [65, 48]:

$$C_C=\begin{cases} C_{L\alpha}\alpha^2\sqrt{f}-C_{D0} & f(\alpha)>f_{crit} \\ C_{L\alpha}\alpha^2(f-E_0)-C_{D0} & f(\alpha)<f_{crit} \end{cases} \tag{6.5}$$

where, C_{D0} represents the drag coefficient at the angle of attack zero and, E_0 is the adjusted parameter that allows to obtained negative values on the chordwise force coefficient under the separated regime.

Procedure to calculate the static Kirchhoff-flow model parameters

The procedure followed to compute the unknown parameters of the Kirchhoff flow model given by Eq. (6.4) and Eq.(6.3) are described as follows for the Reynolds numbers investigated:

1. Using the curve C_L vs α the parameters α_{ss} and $C_{L\alpha}$ are calculated.

2. Using the parameters in the previous step and the Eq.(6.3), the values of f are determined.

3. Adjusting the f values obtained with Eq.(6.3) in previous step with the given Eq. (6.4) then the parameters S_1 and S_2 are estimated.

4. The chordwise force coefficient in Eq.(6.5) and adjusting the values of the static lift and drag force coefficient with the Eq.(4.3) then the parameter E_0 is calculated.

An algorithm in MATLAB was implemented to predict the parameters, $C_{L\alpha}$, α_{ss}, S_1 and S_2 following the procedure described above. An example of the results of this algorithm is included in Fig. 6.4.

In order to have a database to predict the unsteady loads at the range of Re $0.8 - 3.3 \times 10^5$, then the lift and drag force coefficients predicted for this range of Re were calculated with the present CFD techniques. All the empirical parameters explained in the previous paragraphs to replicate the lift and chordwise force coefficient were calculated and included in Table. 6.2. These values were selected since they are within the range of Re of interest for the purpose of this work and because the experimental data of the NACA0015 aerofoils for the static and drag force coefficient is available at these Re in [116].

Figure 6.5(a) compared the CFD results with the prediction of the lift force coefficient using the parameters given in Table 6.2 with expression of Eq.(6.3) and Eq. (6.4). A very good agreement is observed. Additionally, a good agrement is observed with the chordwise force coefficient predicted with the CFD simulations and compared

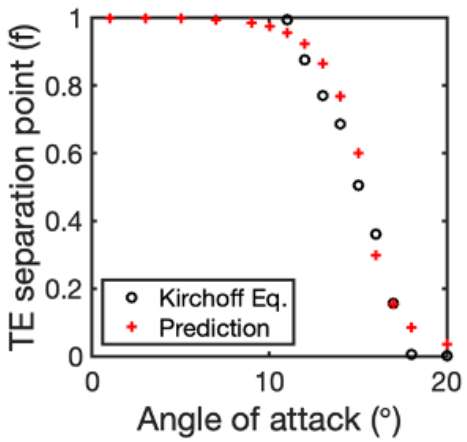

Figure 6.4: TE separation point calculated in step 2 using the Kirchhoff flow Eq.(6.3) and in red, adjusting the S_1 and S_2 parameters in the Eq. (6.4). This example corresponds to the NACA0015 at Re 3.3×10^5.

Table 6.2: The static parameter to replicate the lift force coefficient and the chordwise force coefficient.

Aerofoil	Re	α_{ss} (°)	$C_{L\alpha}$	S_1	S_2	C_{d0}	E_0	f_{crt}
NACA0015	0.8×10^5	10.41	0.10	1.25	2.64	0.020	0.05	0.5
	2.0×10^5	13.31	0.10	3.08	1.02	0.012	0.05	0.5
	3.3×10^5	14.95	0.10	2.25	1.83	0.009	0.05	0.5

with the parameters given in Table 6.2 used in Eq. (6.5). These results suggest that the use of the investigated critical value $f_{crt} = 0.5$ predicts accurately the static force coefficients for the NACA0015 at these low Reynolds number investigated. Despite that, much more efforts need to be made in order to evaluate a wide range of Reynolds number and, additionally take into account different aerofoils profiles to elucidate a general formulation for the TE separation point that improves the current Kirchhoff flow model.

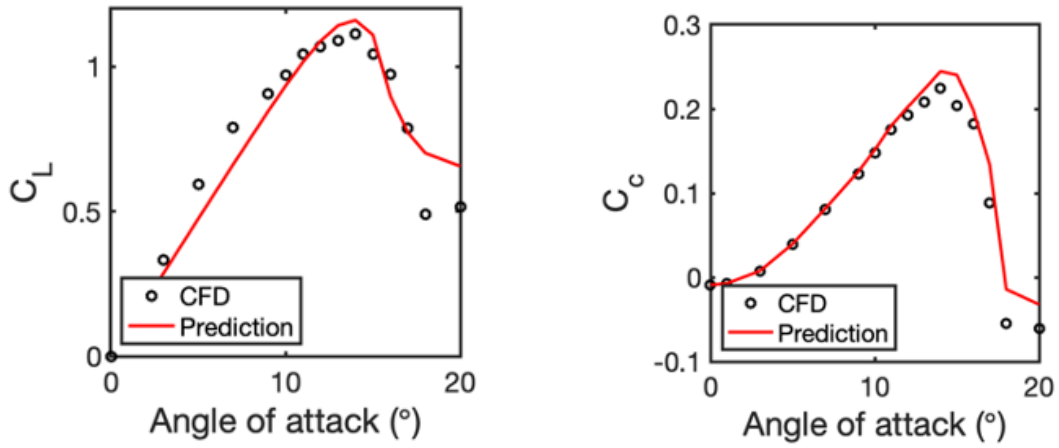

(a) (b)

Figure 6.5: (a) Lift force coefficient as a function of the angle of attack calculated with fluent and using the Kirchhoff flow model, and (b) Chordwise force coefficient calculated by the CFD and predicted with the separation equation.

Stall onset criteria into the Leishman-Beddoes model

The original algorithm of the Leishman-Beddoes model uses the minimum pressure at the leading edge as the criteria for the dynamic stall-inception. Then, by applying a time-lag function, D_{Pn}, to the normal force coefficient described by the unsteady motion, C_{Nn}, a new delayed value of the normal force coefficient is obtained with the expression $C'_N = C_{Nn} - D_{Pn}$. D_{Pn} represents the compensation function containing a time delay constant, T_p, and this is described better in the full algorithm presented Section in A. n represents the time step. Then, the stall-onset criteria of the original LB model reads:

$$C'_N > C_{L1}(Re) \tag{6.6}$$

Equation (6.6) means the dynamic stall-onset angle occurs in an unsteady motion when the delayed normal force coefficient, C'_N, reaches the value of the normal force coeffi-

cient at the static stall conditions that approaches to the value of maximum lift force coefficient, C_{L1}.

Sheng et al. [65] have proposed another stall-onset criteria and this approach consists of applying a delay, $D_{\alpha n}$, directly to the angle of attack, α_n. Hence, the stall-onset occurs as follows:

$$\alpha_n{}' > \alpha_{ss}(Re) \tag{6.7}$$

where, $\alpha_n{}' = \alpha_n - D_{\alpha n}$ and,

$$D_{\alpha n} = D_{\alpha n-1} exp(-\Delta s/T_r) + (\alpha_n - \alpha_{n-1}) exp(-\Delta s/2T_r) \tag{6.8}$$

where Δs represent a non-dimensional time step Δt accordingly the expression $\Delta s = 2U_{ref}\Delta t/c$ This criteria has been used in the modified-Leishman Beddoes algorithm. Additionally, the static parameters investigated in this thesis and included in Table 6.2 as well as the time-delays constants computed in Table 6.1 are also included in this called the LB-modified.

6.3 Analysis of the LB-dynamic stall model under an oscillating motion

At this point, the time delay constants and the Kirchhoff flow parameters have been already computed and hence, the assessment of complete LB algorithm to predict the unsteady loads at Reynolds number lower than one million it can be made. This section analyses the performance of the LB model using the database consisting of the static parameters given in Table 6.2 and the time delay constants included in Table 6.1.

The unsteady chordwise force coefficient (given by Eq. (A.23) has been predicted: (i) using the original LB dynamic stall (LB-OR) model that used the stall-onset criteria given by Eq. (6.6), and, (ii) changing the stall-onset criteria of the original LB dynamic stall model with Eq. (6.7) (LB-mod). The results of the predicted chordwise force coefficient, C_C, with the original and modified LB dynamic stall model has been presented in Fig.6.6.

The Fig. 6.6 (a) includes the case of an oscillating motion at a constant Reynolds number using the VAWT angle of attack equation and a reduced frequency of $\kappa =$

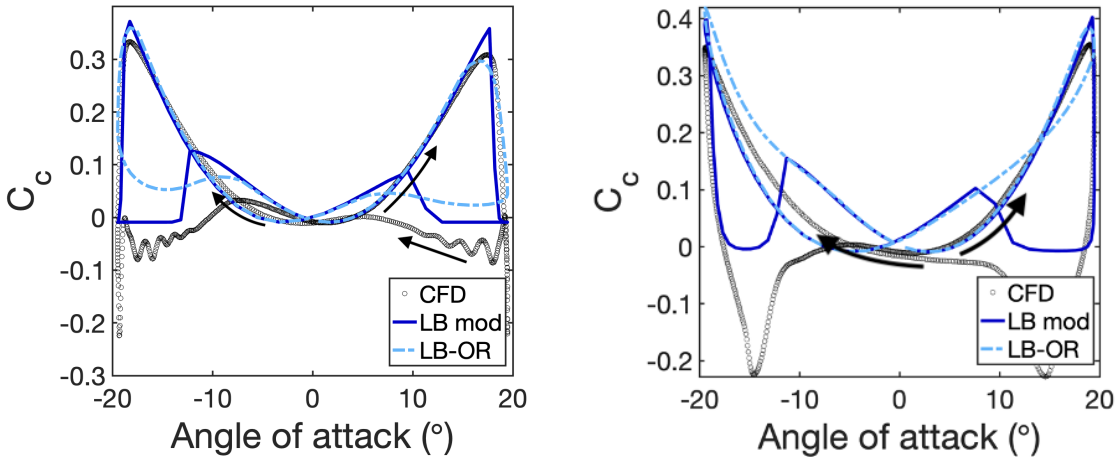

(a) (b)

Figure 6.6: The chordwise force coefficient predicted with the original (LB-OR) and the modified dynamic stall model (LB-OR) at Re 3.3×10^5, $\lambda = 3$ and, (a) $\kappa = 0.025$ and (b) $\kappa = 0.05$. Arrows for both cases of CFD, indicate the direction in the angle of attack.

0.025. For this case, both models compared with the CFD simulations predict very good results, showing some smoother predictions by the original model. In Fig. 6.6 (b) for a case with a reduced frequency of 0.05, the modified LB dynamic stall model, LB mod, predicts accurately the dynamic stall conditions and, in contrast, the original LB dynamic stall fails to accurately predict the stalling conditions, i.e. the loss in the chordwise force coefficient is not detected. The good results obtained by the modified algorithm are attributed to the fact that the criteria given by Eq. (6.7) calculates directly the stall-onset angle. In contrast, the original algorithm needs first to calculate the maximum lift force coefficient using the Kirchhoff flow equation, and then applied the time delay to calculate the stall inception.

The assessment of the modified algorithm of the Leishman-Beddoes model under the fully attached regime is included in Fig. 6.7. The prediction of the chordwise force coefficient with the present CFD simulations are in agreement with the predictions using the modified and original Leishman-Beddoes method. Both LB models capture very well the hysteresis of the forces and it can be concluded that any LB model is able to

predict accurately the unsteady forces of the oscillatory motion under a fully attached regime. In order to have a second point of comparison, the experimental data consisting of an oscillating NACA0015 reproducing the theoretical equation of the VAWT at Re 1.5×10^6, $\lambda = 4.2$ and a frequency of oscillation of 1.463 is included in Fig 6.7. This experimental data shows a maximum angle of attack of 14.47° that is very similar to our present CFD simulations at the tip speed ratio of 4 and a fully attached regime is observed. The hysteresis of the chordwise force coefficient with the experimental data is in agreement with the current CFD simulations and the numerical prediction of the LB models.

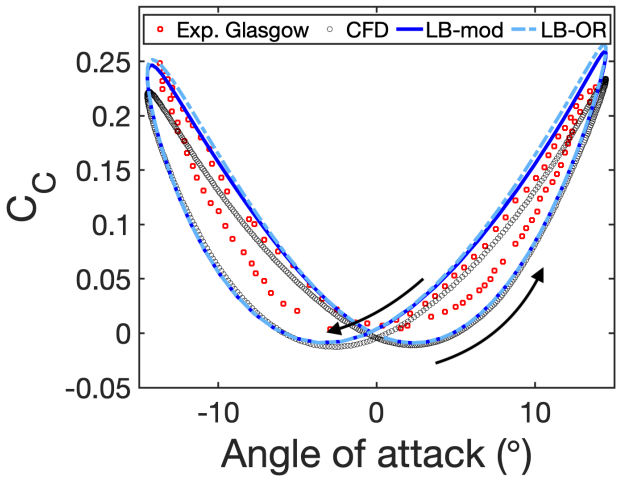

(a)

Figure 6.7: The chordwise force coefficient of an oscillating NACA0015 predicted with numerical techniques at the Re 3.3×10^5 ($\lambda = 4$ and $\kappa = 0.1$) and compared with the experimental data [1] at Re 1.5×10^6. The arrows indicate the direction in the angle of attack during the oscillating motion.

6.4 Prediction of the torque coefficient of VAWTs using the dynamic stall model

The Leishman-Beddoes algorithm including the database tested in the previous Section has been incorporated into the double multiple stream method (DMST) to analyse

the effectiveness of the DMST to predict the unsteady loads. This DMST algorithm has been developed by Parashivoiu and the complete algorithm has been widely described in several investigations [108, 127].

Using the CFD simulations performed in Chapter 5, some cases that clearly show the dynamic stall phenomenon were selected. The first case investigated consists of a one-bladed VAWT turbine using the NACA0015 aerofoil; the incoming flow is 8 m/s, and the Reynolds number is 2.8×10^5. The database allows the interpolation of all the parameters that the Kirchhoff flow model requires as well as the time delay constant, T_r predicted with the stall-onset criteria discussed in the previous Section 6.3. Fig. 6.8 shows the comparison of the CFD simulations (discussed in Chapter 5), the results of using the DMST without any dynamic stall (DMST plain), the results of using the DMST coupled with the original Leishman-Beddoes dynamic stall model (DMST+LB-OR), and the DMST with the modified original Leishman-Beddoes (DMST+LB-mod).

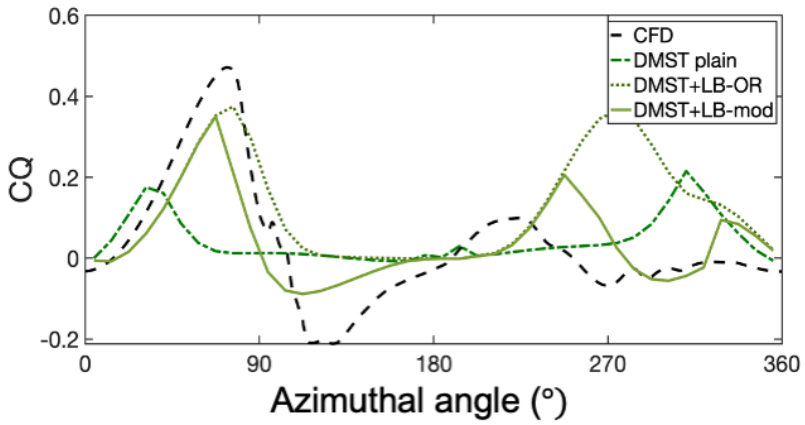

(a)

Figure 6.8: Azimuthal torque coefficient predicted for a one-bladed VAWT and $\lambda = 2$ when employing CFD, non-stall algorithm (DMST plain), the DMST method coupled with the original LB (DMST+LB-OR), and the DMST method coupled with the modified LB (DMST+LB-mod).

The Fig. 6.8 shows that the DMST algorithm without the dynamic stall model is not able to capture the torque coefficient since the stall occurs earlier and it does

not take into account the delay in the stall conditions due to the pitch rate. Using a dynamic stall model, the torque coefficient upstream presents a better agreement with the CFD simulations with both the original and the modified Leishman-Beddoes models. However, downstream, the modified LB dynamic stall model predicts better the torque coefficient and this is attributed to the use of the stall-onset criteria base on the angle of attack.

A second case consisting of two-bladed VAWTs using the NACA0015 and a tip speed ratio $\lambda = 1.5$ has been analysed. It observed in Fig. 6.9 that the DMST alone is not able to capture the stall-onset upstream of the rotor. However, including the dynamic stall model allows a good prediction of the stall-onset upstream of the rotor but downstream the original model over-predicts the torque coefficient. In contrast, the modified LB algorithm is able to calculate not only the stall-onset but also the negative contribution of the torque coefficient.

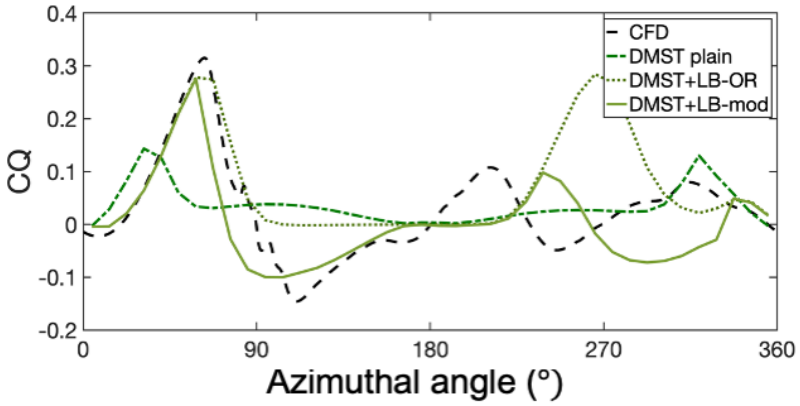

(a)

Figure 6.9: Azimuthal torque coefficient predicted for a two-bladed VAWT and $\lambda = 1.5$ when using CFD, non-stall algorithm (DMST plain), the DMST method coupled with the original LB (DMST+LB-OR), and the DMST method coupled with the modified LB (DMST+LB-mod).

A third case, which shows a light dynamic stall condition at the upstream zone of the rotor in the CFD simulation has been analysed. This case consists of a two-

bladed VAWT at the tip speed ratio of $\lambda = 2.5$ and a pitch angle $\beta = 0°$. In Fig. 6.10 the predictions of the torque coefficient with the plain DMST model, the DMST with the original LB dynamic stall, and the DMST with the modified LB dynamic stall model are included. Also, to compare the CFD prediction with some experimental test, then, the experimental data in [9] was used; the experimental data consists of the azimuthal torque coefficient at a $\lambda = 2.29$ of a two-bladed VAWT with $\beta = 6°$ and using the NACA0015 aerofoil. The comparison between the CFD and the experiment shows a good agreement at the downstream zone. At the downstream zone, the experimental data shows non-stall conditions in C_Q while the CFD does show some light dynamic stall about the $\theta = 90°$. This difference in C_Q is attributed to the pitch angle of 6° in the experimental data, that reduces the maximum angle of attack at upstream, and hence, reduces the probabilities of dynamic stall. This comparison only suggests a good performance of the CFD technique.

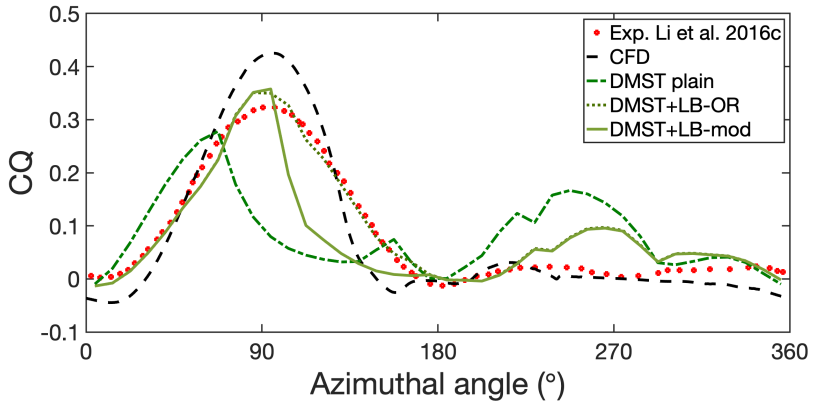

(a)

Figure 6.10: Azimuthal torque coefficient predicted numerically for a NACA 0015 two-bladed VAWT with $\lambda = 2.5$ and $\beta = 0°$ using CFD, non-stall algorithm (DMST plain), the DMST method coupled with the original LB (DMST+LB-OR), and the DMST method coupled with the modified LB (DMST+LB-mod) and, compared with experimental data of a two-bladed VAWT for the NACA0015 at $\lambda = 2.29$ and $\beta = 6°$ [9].

Focus on the analysis of the C_Q prediction with the numerical techniques in Fig. 6.10, the DMST algorithm without a dynamic stall model shows an underprediction

of C_Q at upstream of the rotor and, overpredicts C_Q at the downstream of the rotor compared with the CFD prediction. The DMST coupled with the original-LB dynamic stall fails in predicting the loss in the torque coefficient at $\theta = 90^\circ$ upstream of the rotor and shows some overprediction of C_Q at the downstream zone. In another hand, the DMST coupled with the modified LB model predicts the azimuthal angle where the maximum in the torque coefficient occurs but, after that, the loss in C_Q is not estimate properly accordingly to the CFD results. The underprediction of the torque coefficient at upstream, using both LB algorithms, is associated with curvature effects that need to be included in the numerical predictions with the LB dynamic stall model. This is further discussed in Chapter 7.

In order to assess the capabilities of the DMST+LB to predict the unsteady loads when dynamic stall is not longer observed. Then, two cases without the evidence of dynamic stall were selected. The four case evaluated consists of a one-blade turbine at a tip speed ratio $\lambda = 3$. Figure 6.11 shows that when using the OR LB dynamic stall and the modified, LB mod, the prediction of torque coefficient is equivalent at both the upstream and downstream of the rotor. This agrees also with the predictions for an oscillating aerofoil in Fig. 6.7 under non-stall conditions carried out with both LB models. Despite that, a large underprediction of the torque coefficient is observed upstream of the rotor and an overprediction downstream of the rotor when compared with the CFD simulations. The DMST alone produces the largest difference between the torque coefficients when using the CFD simulations.

The difference observed in Fig. 6.11 between the CFD and the models evaluated maybe attributed to the lack of corrections due to the influence of the curvature effect that is not captured by any of the methods. For example, at the azimuthal angle 0°, all the methods predict a torque coefficient of zero, while the CFD simulations predict a negative torque coefficient. Another reason is explained due to the miscalculation of the interference factor by the DMST model. This is due to the fact that the DMST was formulated based on the VAWTs with very low solidity.

The last case, consisting of a three-bladed VAWTs at a tip speed ratio $\lambda = 2.5$ has been analysed in Fig. 6.12. This case represents a non-stall condition and the results have shown that with and without dynamic stall the torque coefficient is not predicted

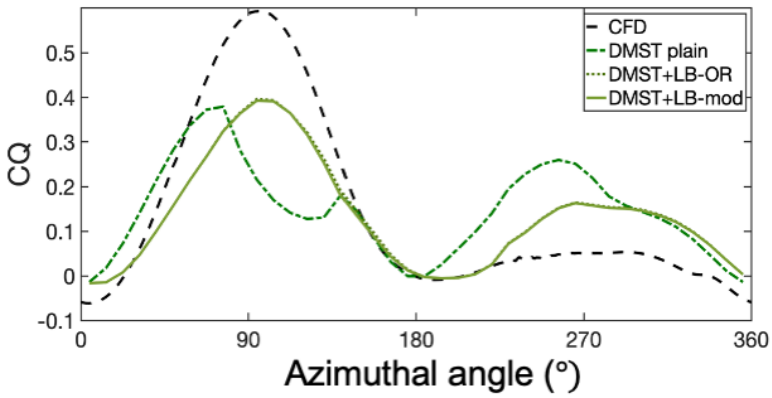

(a)

Figure 6.11: Azimuthal torque coefficient predicted for a one-bladed VAWT and $\lambda = 3$ using the CFD, non-stall algorithm (DMST plain), the DMST method coupled with the original LB (DMST+LB-OR), and the DMST method coupled with the modified LB (DMST+LB-mod).

accurately. At the downstream of the rotor, some good agreement is observed when including the dynamic stall. The disagreement in the torque coefficient among the CFD simulations and the predicting methods is more related to the interference factor and the curvature effects that are not very well capture in the evaluated DMST algorithm. The increase of the tip speed ratio and the increase in the number of blades maybe causing an increase in the blockage effect and in the curvature effects that current methodologies are not able to capture. The effect of both, the number of blades and the curvature effect is discussed in the next Chapter 7 and will assist in a better understanding of the unsteady aerodynamics of the VAWTs.

6.5 Discussion

In this chapter, a deep analysis of the main parameters required to develop a reliable fast tool to predict the unsteady loads on VAWTs has been performed. The dynamic stall model investigated, the Leishman-Beddoes model, considers the main physics behind the dynamic stall phenomenon, but in order to apply this algorithm to understand

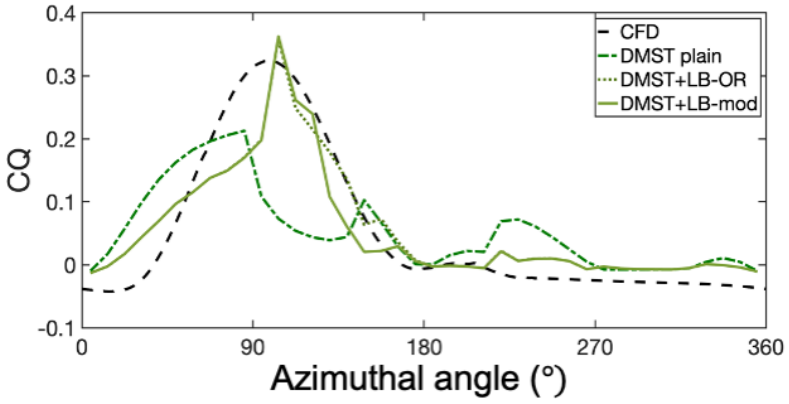

(a)

Figure 6.12: Azimuthal torque coefficient predicted for a three-bladed VAWT and $\lambda = 2.5$ when using CFD, non-stall algorithm (DMST plain), the DMST method coupled with the original LB (DMST+LB-OR), and the DMST method coupled with the modified LB (DMST+LB-mod).

the VAWTs some its sections needs a detailed assessment not previously presented in the reviewed literature.

The analysis of the static separation point of the boundary layer at low Reynolds numbers and its corresponding value of lift force coefficient has revealed that the loss in the lift force coefficient does not occur suddenly as the observations experimentally at high Re as found in several investigations [116], i.e., it occurs smoothly. This aspect has makes the obtention of the representative parameters to predict the lift and the chordwise force coefficient being more challenging as well as very important for an accurate prediction of the static and unsteady forces. Despite that, the database generated has been tested to be good enough to predict the static and unsteady loads for the NACA0015 at the range of Reynolds number investigated. This database can be used complementary to the database presented for the NACA0015 at larger Reynolds number in [48].

The analysis of the trailing edge separation point using the location along the chord where a zero skin friction is experienced have revealed that, at the low Reynolds num-

bers investigated here, the maximum lift coefficient occurs at the critical separation point about 0.5. This value is different from the values 0.6-0.7 usually found in the literature for Reynolds number larger than 1 million. Despite this investigation using CFD simulations, such simulations where very carefully verified with the experimental data of the static lift force coefficient. As a result, the use of a critical separation point of 0.5 into the Leishman-Beddoes model predicts accurately the unsteady forces under dynamic stall conditions. Nevertheless, experimental tests that confirms these results are worthy to be made; i.e. since the VAWTs can operate at low Reynolds number, the more in-depth analysis of how the trailing edge separation point of the boundary layer behaves with the Reynolds number decreasing are crucial for a much better understanding of the unsteady aerodynamics and to improve the Kirchhoff flow model to take into account the effect of these low Reynolds numbers.

The time delay constants investigated for the three aerofoils NACA0015, NACA0018 and NACA0021 at low Reynolds number represents a huge effort to understand the stall inception of VAWTs. The more than 80 CFD unsteady simulations performed to compute the curves of the stall-onset as a function of the non-dimensional pitch rate have to assist to meet the urgent objective of having a broader idea of the time delay constants at different Reynolds numbers. Present results suggest that each aerofoil dictates the behaviour of the time delay constant, T_r but in general T_r reduced its value with the decrease in Re. Additionally, the present analysis revealed that after a Reynolds number of 3.6×10^5 the time delay constant suffers of minor changes in its value. The NACA0021 aerofoil has demonstrated to be the aerofoil with the less impact in the time delay values T_r with the change of the Reynolds. Present results despite they need to be confirmed using experimental data are based in a large number of CFD verifications using static, oscillating and VAWTs cases and then are considered to be accurate enough for the final objective of this thesis, to contribute to the development of fast and reliable engineering tool to predict the performance of VAWTs.

The LB dynamic stall algorithm including the present modifications to the stall-onset criteria and the critical separation point in the Kirchhoff flow model, has demonstrated to be a potential algorithm to predict the unsteady loads under both regimes, under the dynamic stall and non-stall conditions. Also, the results of using the double

multiple streamtube algorithm by incorporating the dynamic stall model have presented some good predictions of the torque coefficient at low tip speed ratios when comparing with the CFD simulations. Nevertheless, with the increase of the tip speed ratio and the number of blades the prediction becomes less reliable since both upstream and downstream torque coefficient predictions present some deficiencies. These deficiencies are attributed to the lack of corrections regarding the curvature effects of the blades. Despite this phenomenon have been discussed and incorporated into the DMST algorithm in [53], still, this mechanism suffers from a shortage of investigations and hence required further investigations to be properly addressed and assessed as described in Chapter 7. This chapter has presented a detailed assessment of the critical aspects that need to be considered during the modelling of the torque coefficient of a VAWT.

6.6 Summary

This chapter has discussed the details that are required for the dynamic stall algorithm to be able to predict the unsteady loads at low Reynolds number that are very useful for the VAWTs torque prediction. Some of the important contributions of this chapter are as follows:

- A database of the time delay constant of three aerofoils at Reynolds number lower than 3.6×10^5. The studied range of Reynolds number has not been studied previously, as far as the knowledge and literature review carried out on this thesis, and thus, this investigation represents a very useful contribution in order to predict unsteady loads in the range of Reynolds number studied here.

- The parameters representing the Kirchhoff flow model to predict the lift force coefficient and chordwise force coefficient at static conditions are very useful data to predict the unsteady loads using the Leishman-Beddoes algorithm.

- The trailing separation point has been analysed by using the skin friction along the chord at each angle of attack. It has been observed that the critical separation

point occurs at the static stall conditions and it has a value of 0.5 at the low Reynolds numbers evaluated in this Chapter. Using this critical value of 0.5 has led to a very good predictions of the lift and chordwise force coefficients.

- The analysis has revealed that the modified Leishman-Beddoes model using the database of the time-delay constant and Kirchhoff flow parameters predict accurately the unsteady loads under both dynamic stall and non-stall conditions for oscillating aerofoils.

- An assessment of the DMST algorithm coupled with the dynamic stall algorithm to predict the torque coefficient of VAWTs has been carried out. The results have demonstrated that under dynamic stall conditions some good agreement with the CFD results are observed. On the contrary, under the fully attached regime the results have shown disagreements with the CFD results where it is observed that there is an under-prediction at the upstream of the rotor and an over-prediction at the downstream of the rotor.

Chapter 7

Curvature effect on the prediction of the torque coefficient of VAWTs

7.1 Overview

Despite previous investigations having studied the influence of the curvature index on the VAWT performance, the assessment of this phenomenon has missed some important details due to the lack of experimental data, such as the azimuthal forces, but instead have relied on the average torque coefficient per revolution. Thus, a full understanding of this phenomenon remains unclear. This chapter analyses the curvature index effect on the torque coefficient of the VAWTs by using CFD simulations and the modified Leishman-Beddoes model introduced in Chapter 6. A new concept to investigate the VAWTs aerodynamics has been proposed. This new concept has been demonstrated to have a huge potential towards the development of a fast tool to predict the power coefficient of VAWTs and that takes into account the unsteady aerodynamics of VAWTs over a wide range of TSRs.

7.2 Interference factor

The increase in the number of blades, as well as the increase in the tip speed ratio, promotes an increase in the blockage effect of the rotor, i.e. the rotor behaves as a solid disk that reduces the magnitude of the actual wind velocity acting on the VAWTs blades. The percentage of the reduction in the incoming wind speed, V_∞, due to the solid aspect of the rotor is called the interference factor and its value may depend on solidity ($\sigma = Nc/D$), the tip speed ratio and the azimuthal position of the blades . Once the flow past the blades with a reduced velocity, V_{up}, at the upstream zone of the rotor, the

actual wind speed that impacts on the blades downstream, V_{dw}, is further reduced, see Fig. 7.1. Thus, the interference factor upstream, u, is much less than the interference factor downstream of the rotor, $u\prime$. Bearing in mind that the theoretical expressions of the relative velocity, Eq. (2.1) and the angle of attack, Eq.(2.2) cannot replicate the effect of the number of blades, the use of the interference factor plays a significant role to compute the actual velocity on the blades and the actual angle of attack.

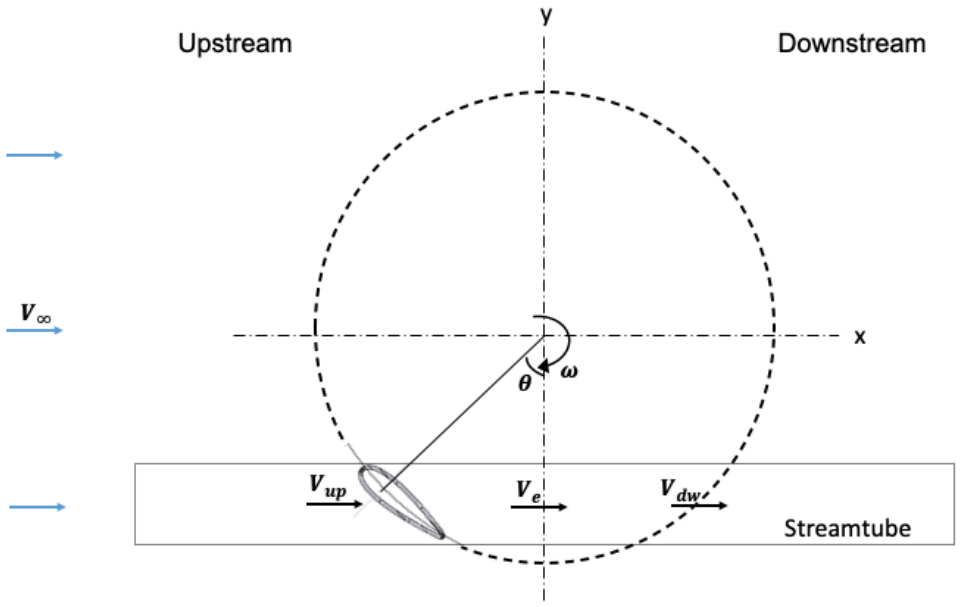

(a)

Figure 7.1: A typical representation of the streamlines when a flow past a VAWT [2]

In previous investigations, the mathematical expressions for the interference factors both upstream and downstream of the rotor has been proposed accordingly Eq. (3.9) in [2]. Despite that, those interference factor relations were obtained for a specific geometry of the rotor (troposkein design) and and are based in a blade element momentum analysis. Using those expressions to predict the torque coefficient of the

VAWTs investigated in this thesis raised some difficulties in obtaining convergence when using the large solidity VAWTs (results from Chapter 6). In addition, despite some investigations have attempt to investigate the interference factor [128], the data with details of this parameter at each azimuthal position are very limited. Nowadays, with the current CFD techniques, is possible to obtained much more details of the flow filed around the blades and then improve or elucidate new interference factor expressions. Therefore, this section investigates by using the CFD simulations carried out in Chapter 5, the interference factors on the VAWTs using the NACA0015 aerofoil with one, two and three bladed and, at a range of tip speeds ratio [1.5-5].

In order to observe the behaviour of the interference factor across the rotor, the x-component of the velocity, V_x, is computed using the CFD simulations along the y-axis, from the centre line of the rotor to two times the rotor diameter, i.e, from $y = -2D$ to $y = 2D$. Moreover, nine positions along the incoming wind flow direction (x-axis) were analysed: at the positions of -10D, -5D, -2D, -1D, 0 at upstream zone of the rotor and, downstream at the positions of 1D, 2D, 5D, 10D. Therefore, any changes in the interference factor perpendicular to the incoming flow directions due to the presence of the rotor were observed. Fig. 7.2(a) includes the interference factor evolution along the x-direction for a one-bladed VAWT and a tip speed ratio of 4 and, Fig. 7.2(b) corresponds to a three-bladed VAWT at a tip speed ratio of 2.

Since the interest is the interference factor on the blades, three positions are the main focus for this analysis, namely (i) the position $-1D$ corresponding to the upstream zone of the rotor when the flow is about to impact the blades, (ii) the position $0D$ that represent the interference factor of the flow before impacting on the blades of the rotor at downstream, and (iii) the position $1D$ that represent the flow interference factor immediately when the flow past the blades that are downstream of the rotor.

It is observed for the one-bladed VAWT in Fig. 7.2(a) that upwind (at $x = -1D$) the interference factor is almost zero and hence the flow disturbances on the flow due to one blade at $\lambda = 2$ is almost negligible. Downstream of the rotor, the interference factor reaches a maximum value of 0.28 at the middle of the rotor at the position $x = 0D$. For the three-bladed VAWT in Fig. 7.2(b) a maximum of 0.17 is reached at the position $x = -1D$; at the position of $x = 0D$ the interference factor reaches a value of 0.80 and

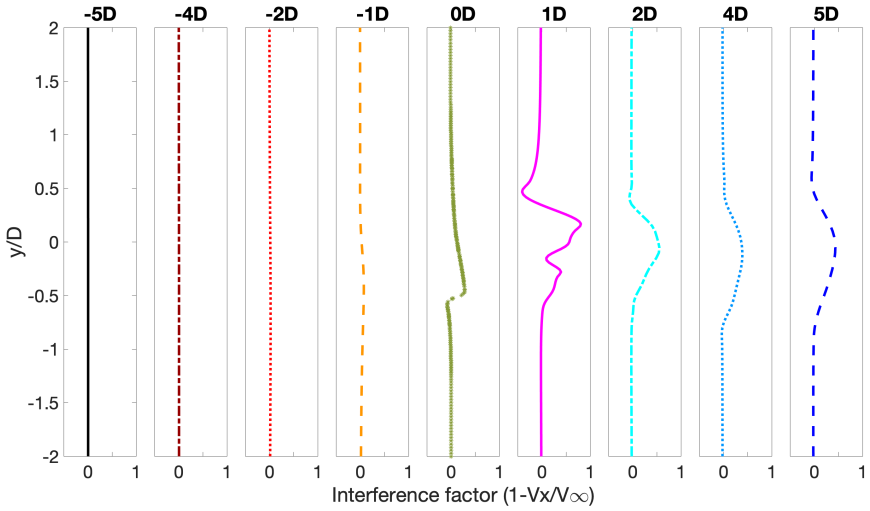

(a)

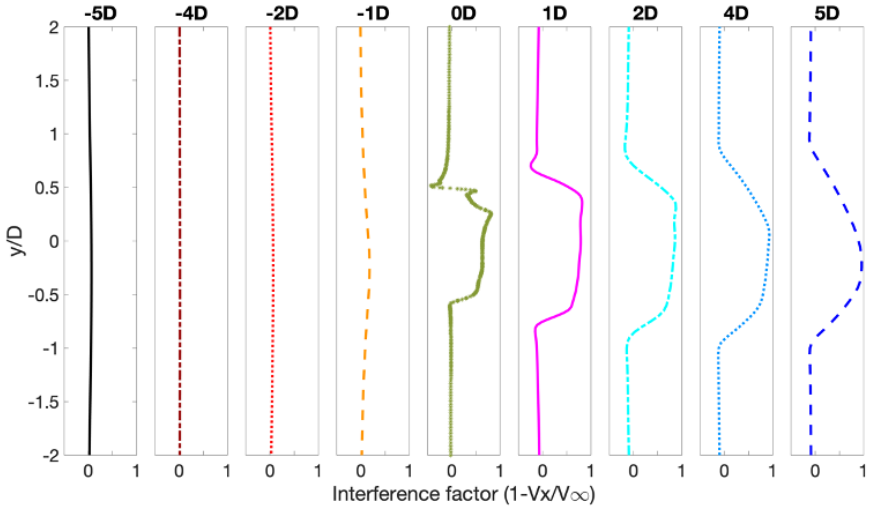

(b)

Figure 7.2: Interference factor at nine positions along the x-direction for:(a) One bladed-turbine and a tip speed ratio of 2, and (b) a three-bladed turbine and a tip speed ratio of 2. Both VAWTs with the NACA0015 aerofoil.

further downstream at the position of $x = 1D$ the interference factor reaches a value of 0.92.

The analysis of the maximum interference factor at the position $x = -1D$, $x = 0D$

and $x = 1D$ for all the cases, i.e., a VAWT with one, two and three blades and at a range of TSRs [1.5-5], included in Section B have revealed the interference factor upstream downstream of the rotor can be represented by some sine azimuthal functions as described below.

The upstream interference factor, u, follows a sine function variation that is described by the following equation:

$$u = \frac{a_1}{2} + \frac{a_1}{2} sin(\omega t) \tag{7.1}$$

where, a_1 represents the maximum interference factor located upstream of the rotor and depends on the solidity and rotational speed and is given by the following expression:

$$a_1 = 0.07\sqrt{\sigma\omega} - 0.035 \tag{7.2}$$

Equation (7.2) results from the linear adjustment of the maximum interference factors located at the positions $x = -1D$ and this is included in Fig. B.1.

Similarly, the analysis downstream of the rotor reveals that the interference factor, $u\prime$, follows the expression:

$$u\prime = abs(a_2 sin(\omega t)) \tag{7.3}$$

where, a_2 represents the average of the maximum interference factors located at the positions $x = 0D$ and $x = 1D$ for all the cases investigated and included in Fig. B.1. The average of this two positions have been considered since after the several analysis performed in Section 7.3 and 7.4 it gives the most reliable prediction of the torque coefficient.

$$a_2 = 0.23\sqrt{\sigma\omega} + 0.08 \tag{7.4}$$

Some examples of the adjusted sine functions given by by Eq. (7.1) and (7.3) are presented in Fig. 7.3. Fig.7.3(a) shows that the sinusoidal function given by Eq.(7.1) starts at half of the maximum value of the maximum interference factor for both cases. The first 90 degrees of the rotor show very good agreement between the approximation

and the CFD results, but from 90 to 180 degrees there is a small difference that overall does not impact the results since the parameters that define the stall-onset angle are more likely to occur before this azimuthal angle. Downstream of the rotor, the sinusoidal Eq. (7.3) results in the most useful and practical approximation since it captures the reduction in the wind speed. Fig. 7.3(b) illustrates that the sine functions starts almost from zero, reaches a maximum and then decays, therefore expression (7.3) it better represents the behaviour of the interference factors at downstream of the rotor.

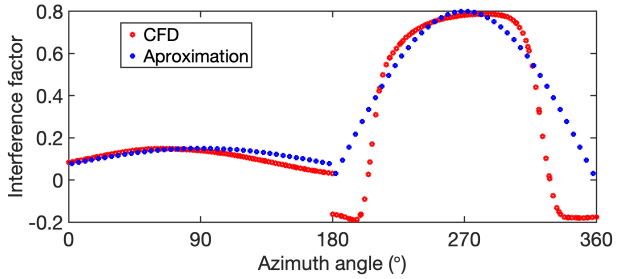

(a)

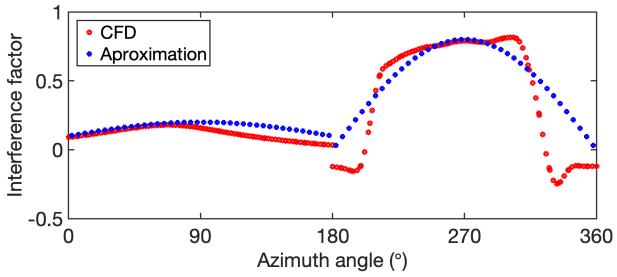

(b)

Figure 7.3: Interference factor as a function of the azimuthal angle for (a) a two-bladed VAWT at $\lambda = 3.5$ and, (b) a three-bladed VAWT at $\lambda = 2$. Both VAWTs using the NACA0015 aerofoil.

7.3 Curvature effects

The curvature effects of the VAWTs originated due to the rotation of the blades around the axis, causes the aerofoil to move along a curved streamlines instead of along a straight line flow. This phenomenon is illustrated in Fig. 7.4. Due to this curved flow,

a virtual camber incidence is induced that causes an increase in the effective angle of attack [52, 129]. In order to include this phenomenon in the prediction of the power coefficient of VAWTs, several procedures have been implemented. The most used is the approximation developed by Migliore et al. [52] consisting of properly transforming the coordinates of the flow curvature to obtained the resulting camber aerofoil coordinates. This method has been implemented in [129, 130]. Despite some knowledge being available on the curvature effects in the existing mentioned literature, its influence due to the number of blades and due to the tip speed ratio remains unclear. This final gap in the literature is the main objective of this section.

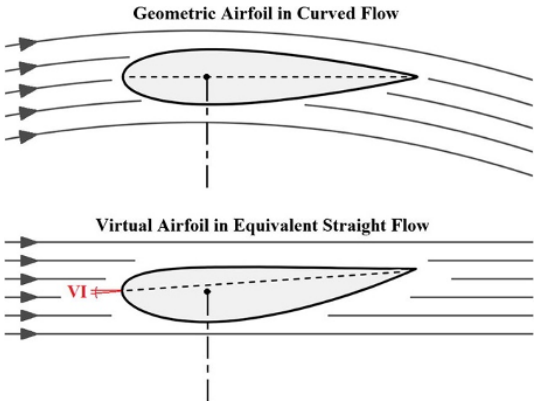

(a)

Figure 7.4: Representation of the curvature effect on the blades of VAWTs [10]. Above, the streamlines of the flow when the blades is rotating around the axis; at the bottom, the transformed aerofoil with equivalent aerodynamics characteristics of the curved flow.

The camber aerofoil

Along the years, the geometrical modification of the aerofoil to obtain specific aerodynamic characteristics has led to the modification of the camber, the thickness, the leading edge, the trailing edge, etc. An increase in the camber with a positive increase in the effective angle of attack produces a positive lift force coefficient with a non-zero value at the angle of attack 0°. For example, Fig. 7.5(a) shows the lift force

coefficient for two cambered aerofoils, NACA2415 and NACA4415, and the symmetrical NACA0015. It is observed that the cambered aerofoils produce a larger lift force coefficient at positive angles of attack. On the contrary, at a negative angle of attack the lift force coefficient reduces its magnitude with the increase in the camber. The drag coefficient remains very similar in value for the three aerofoils as observed in Fig. 7.5(b).

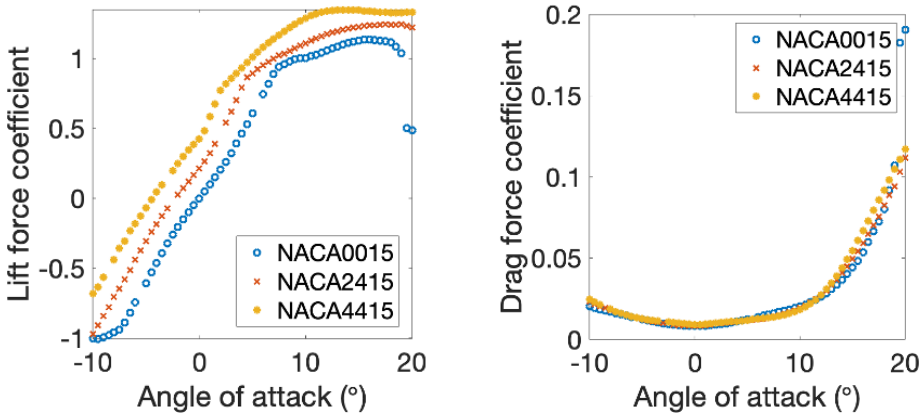

(a) (b)

Figure 7.5: Camber effect on (a) the lift force coefficient and, (b) the drag force coefficient as a function of the angle of attack at Re=3.3×10^5. Data calculated using Xfoil.

The main objective of introducing a camber with a non-zero value consists of modifying the effective angle of attack of the aerofoil profile. Then, this camber effect can be modelled into the LB model by using the angle of attack where the lift force coefficient becomes zero, α_0 and introduces this angle into the effective angle of attack, $alpha_E$. Therefore, in the Leishman-Beddoes algorithm, the effective angle of attack, α_E given by Eq.(A.3) is replaced by: .

$$\alpha_{E_n} = \alpha_n + r_n/2 - X_n - Y_n - \alpha_0 \tag{7.5}$$

Under static conditions and using the Kirchhoff flow model, the lift force coefficient of the cambered NACA2415 and NACA4415 are predicted and included in Fig. 7.6. The

percentage of cambered corresponds to 2% and 4% for the NACA2414 and NACA4415, respectively. For the NACA2415, the lift force coefficient with $C_L = 0$ is found at $\alpha_0 = -2°$; for the NACA4415, $C_L = 0$ at $\alpha_0 = -4°$. Replacing the geometrical angle of attack, $\alpha(t)$ by $\alpha(t) - \alpha_0$ into the Kirchhoff flow model and using the static-parameter characteristic of the symmetrical aerofoil, the NACA0015 produces the actual lift force coefficient of the cambered aerofoil as illustrated in Fig. 7.6. Both cambered aerofoils, NACA2415 and NACA4415, produce a the similar C_L for the NACA0015 but with an initial zero value located at a negative angle of attack, α_0. Therefore, by predicting the virtual angle of incidence, α_0, the curvature effect can be easily investigated.

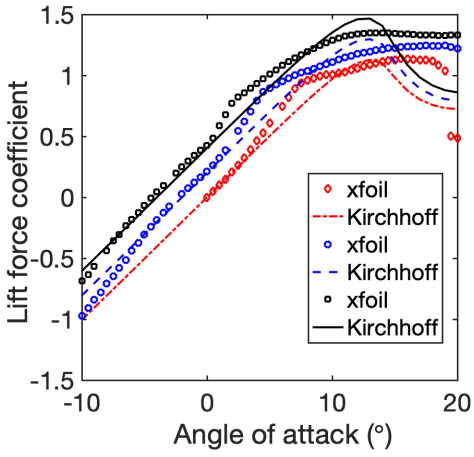

(a)

Figure 7.6: Lift force coefficient calculated with xfoil and predicted with the Kirchhoff flow model by introducing a camber angle of: $\alpha_0 = 0$ for the NACA0015 (red); $\alpha_0 = -2$: for the NACA2415 (blue) and, $\alpha_0 = -4$ for the NACA2415 (black).

The qualitatively analysis of the streamlines in Fig. 7.7(a) of a one-bladed VAWT has revealed that: at the lowest tip speed ratio, $\lambda = 2$, the streamlines describe a virtual curvature index, $c/R\prime$, where $R\prime$ represents the radius described by the streamlines. This virtual curvature index is reduced compared with the geometrical curvature index, c/R. At a higher tip speed ratio of $\lambda = 5$, Fig. 7.7(b), shows that the virtual curvature index described by the streamlines are in accordance to the geometrical curvature

index. In addition, the streamlines at the same tip speed ratio $\lambda = 2$ show that for the two-bladed VAWT shown in Fig. 7.7(c) that the virtual curvature index is larger than the geometrical curvature index, and also a similar virtual curvature index with the one-bladed VAWTs is observed. In the case of the three-bladed VAWT shown in Fig. 7.7(d), the streamlines describe a virtual curvature index that is not clearly defined but are influenced by the blades interaction.

7.3.1 Virtual camber estimation

In this thesis, the estimation of the virtual camber, α_0 has followed a systematically methodology and using previous investigations [52] as a basis to define a relation of the virtual camber with the curvature index, the tip speed ratio and the number of blades.

The results shows that with the increase in the tip speed ratio, the virtual curvature index trends towards the value of the geometrical curvature index, and this is observed in Fig. 7.7(b). Therefore, the virtual camber α_0 was investigated for a range of tip speed ratio of [2-5] using a one-bladed VAWT with a geometric curvature index of $c/R = 0.1325$.

To investigate the influence of the virtual camber in the torque coefficient, then, the torque coefficient as a function of the azimuthal angle has been predicted using the modified Leishman-Beddoes model with: (i) the theoretical angle of attack and theoretical relative velocity given by Eq.(2.2) and Eq.(2.1) respectively; (ii) the new method consisting of the use of the interference factor correlations described in the previous section plus the virtual camber modification to the effective angle of attack by including the virtual incidence, α_0 and; (iii) the CFD simulations performed in Chapter 5.

The torque coefficient predicted with the new proposed method has shown very good agreement with the CFD simulations. At the tip speed ratio of 2, the use of the virtual camber is essential to predict accurately the torque coefficient. As an illustration of this influence, Fig. 7.8(a) shows that the lack of use of the virtual camber, the theoretical case, shows an underprediction of the torque coefficient upstream of the rotor and an over prediction downstream. For a high tip speed ratio of 5, again Fig.

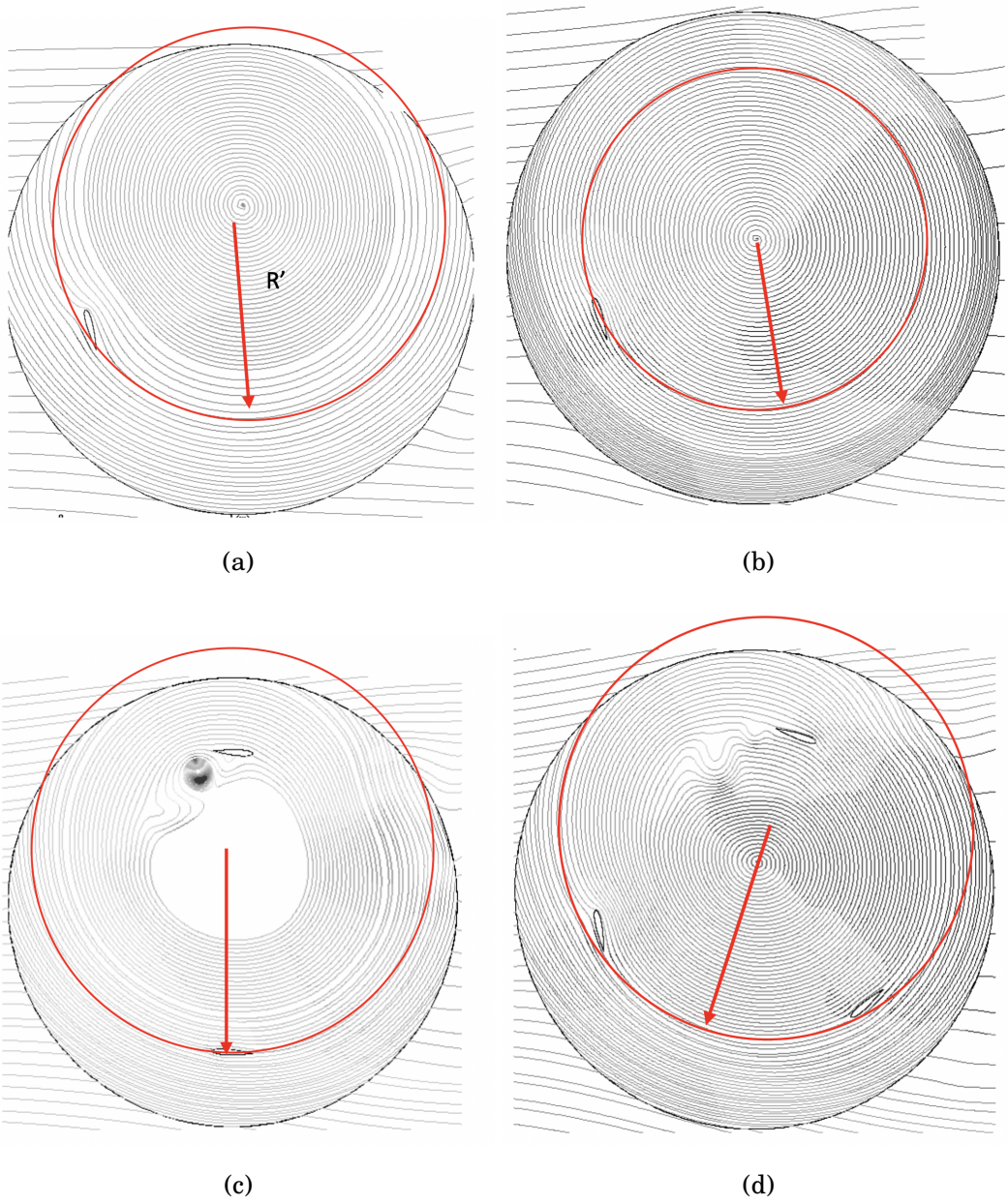

Figure 7.7: Streamlines for (a) one-bladed VAWT with $\lambda = 2$, (b) one-bladed VAWT with $\lambda = 5$, (c)) two-bladed VAWT with $\lambda = 2$ and, (d) three-bladed VAWT with $\lambda = 2$.

7.8(b) shows that the use of the virtual camber improves the prediction of the torque coefficient compared with the under prediction if no virtual camber is used as well as no interference factor. At the high tip speed ratio it can be concluded that the virtual

camber is essential to capture the torque coefficient. Using the new method, it has been found that for the range of tip speed ratio [2-5] and using a one-bladed VAWT, the virtual camber, α_0 presents a value from -2° to -3°.

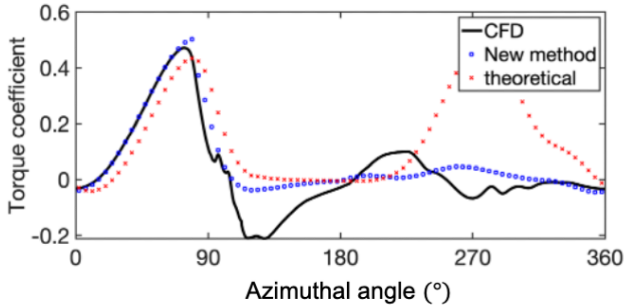

(a)

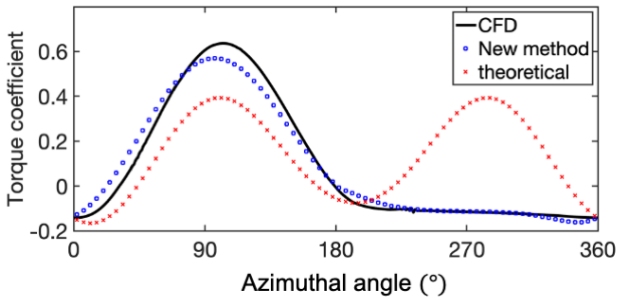

(b)

Figure 7.8: Prediction of the torque coefficient with different approaches as a function of the azimuthal angle using a one-bladed VAWT at (a) $\lambda = 2$ and, (b) $\lambda = 5$.

Using the new proposed method for two-bladed and a three bladed VAWTs, the virtual camber effect has been analysed in detail. It has been observed that for the same tip speed ratio that the increase in the number of blades reduces the virtual camber effect. For example, at the tip speed ratio of 3 the value of α_0 has resulted in -2.7°, -1.76° and -0.77° for one, two and three-bladed VAWT, respectively. In addition, using these values, the predicted torque coefficient has resulted in a very good agreement with the CFD simulations, see Fig. 7.9(a-c).

The present observations have led to the formulation of a mathematical expression

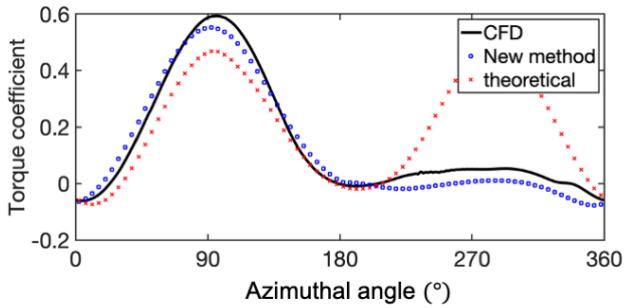

(a)

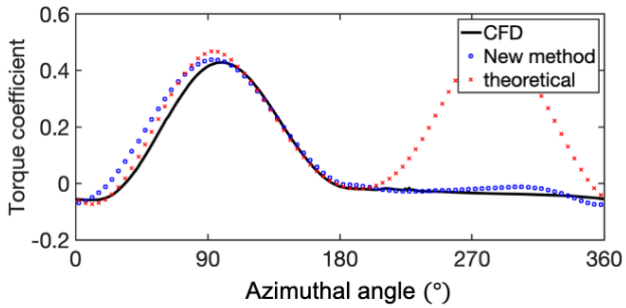

(b)

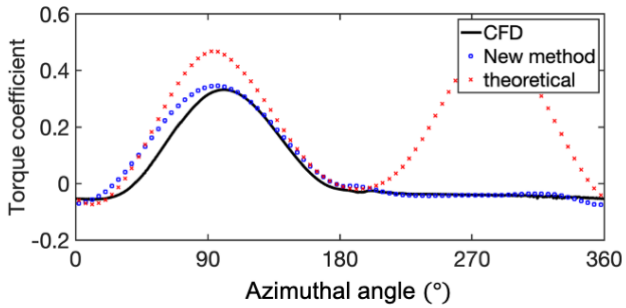

(c)

Figure 7.9: Torque coefficient as a function of the azimuthal angle predicted with the new proposed method at the tip speed ratio of 3 and a (a) one-bladed, (b) two-bladed and, (c) a three-bladed VAWT.

that relate the camber effect, α_0, with the tip speed ratio and the number of blades and this is described as follows.

The values of α_0 estimated with the new proposed method by adjusting this angle

with all the CFD simulations for the NACA0015 VAWT performed in Chapter 5 relates with the following expression:

$$\alpha_0 = (-\frac{\omega c}{4\overline{V_{rel}(t)}})(1-2\sigma)(180^\circ/\pi) \tag{7.6}$$

where the expression for the $\overline{V_{rel}(t)}$ is given by the average of following equation.

$$V_{rel}(t) = V(1+2X_r\cos(\omega t)+X_r^2)^{1/2} \tag{7.7}$$

where, the induced velocity, V, represents the reduced velocity due to the interference factor given by Eq.(7.1) and Eq. (7.3).

$$V = \begin{cases} V_\infty(1-u), & if\,\omega t < \pi(upstream) \\ V_\infty(1-u\prime), & if\,\omega t > \pi(downstream) \end{cases} \tag{7.8}$$

In addition, the local tip speed ratio is given by $X_r = \omega R/V$.

The term, $(-\frac{\omega c}{4\overline{V_{rel}(t)}})$ in Eq.(7.6) takes into account the effect of the tip speed ratio. Since the average of the relative velocity, $\overline{V_{rel}(t)}$ increases with the increase in the tip speed ratio, and approximates to $V_{rel} \approx \omega R$. Then, at larger tip speed ratios, $-\frac{\omega c}{4\overline{V_{rel}(t)}} = -\frac{c}{4R}$. For the VAWT investigated here with $c/R = 0.265$, $-\frac{c}{4R} = -3.79^\circ$. This result agrees with the predicted virtual incidence of 3.7° corresponding to a curvature index $c/R = 0.260$ calculated by Migliore et. al [52] with a method consisting of an inverse virtual transformation of the aerofoil.

It is worth to mentioning that surprisingly, a similar expression $(-\frac{\omega c}{4V_{rel}})$ was also used in [53] to take into account the curvature effect in the angle of attack. However, in this work, the virtual camber changes with the azimuthal angle. Despite this representation of the virtual incidence it is similar, the concept remains different since in this work the aerofoil seems to behave as a cambered aerofoil with a define α_0 accordingly to the TSR and the number of blades instead of changing constantly at each azimuthal position the virtual incidence. Nevertheless it is worthy to investigate at each azimuthal position of the blades the curvature of the streamlines to elucidate the actual influence of the curvature effect. The proposed investigation represents a huge effort and due to the amount of CFD data required are out of the scope of this thesis.

Moreover, in the Eq.(7.6), in order to consider the influence of the solidity then the expression $(1-2\sigma)$ has been included. This expression is limited for the VAWTs evaluated here, despite that, with some further CFD simulations a more general expression may be found.

7.4 Prediction of the torque coefficient: New proposed method

In this section the main governing equations of a new method to predict the torque coefficient of VAWTs has been explained. In summary, the methodology consists of the following steps:

1. Define the geometrical characteristics of the rotor: chord (c), number of blades (N), radius (R), pitch angle (β) and wind speed, V_∞.

2. Predict the interference factor, u and $u\prime$ using the Eqns. (7.1-7.4).

3. Calculates the relative velocity equation, Eq. (7.7).

4. Estimate the angle of incidence due to the virtual camber, α_0, Eq.(7.6).

5. Estimate the angle of attack using following expression:

$$\alpha(t) = atan(\frac{sin(\omega t)}{X_r + cos(\omega t)}) - \beta \tag{7.9}$$

6. Use the expressions of $\alpha(t)$, $V_{rel}(t)$ and α_0 given in previous steps to calculate the dynamic lift $C_L(t)$ and drag $C_D(t)$ force coefficients using the Leishman-Beddoes dynamic stall model with the modifications, namely, the stall-onset criteria, the new predicted static parameters and by modifying the effective angle of attack.

7. Compute the torque coefficient using the expression:

$$C_Q(\theta) = \frac{c}{2R}(\frac{V_{rel}}{V_\infty})^2(C_L sin(\phi) - C_D cos(\phi)) \tag{7.10}$$

   where $\phi = \alpha + \beta$.

8. Calculate the power coefficient :

$$C_p = \frac{N\lambda}{2\pi}\sum_{0}^{2\pi} C_Q(\theta)d\theta \tag{7.11}$$

where, $d\theta = \pi/N_{th}$ and N_{th} represents the number of divisions required to analyse the rotor.

The described methodology has been used to predict the azimuthal torque coefficient at two tip speed ratios. At $\lambda = 2$ in Fig. 7.10(a) and at $\lambda = 3.5$ in Fig. 7.10 (b). This method accurately predicts the torque coefficient for the one and two bladed VAWTs. A small over prediction is observed for a three bladed VAWT at $\lambda = 2$ at the upstream zone of the rotor. Despite that, due to the complexity of the flow and the time consumed by a CFD simulation, this fast tool gives a very good approximation of the torque coefficient. The proposed new method predict with very good agreement azimuthal angle of inception of the CFD simulations of the VAWTs. This suggests that the modifications to the Leishman-Beddoes model and the time delay constant as a function of the Reynolds number performs well under dynamic stall conditions.

The virtual incidence due to the camber effect with the increase in the tip speed ratio has been very well predicted for all the number of blades investigated as observed in Fig. 7.10(b). The results suggest that the equation to predict the camber effect is crucial in the prediction of the torque coefficient at large tip speed ratios

7.5 Influence of the pitch angle of the performance of VAWTs

The pitch angle has been investigated in several studies before, despite that some aspects in the detail both upstream and downstream of the rotor has been missed due to the time consumption of a CFD simulation. Therefore, using the current method, the effect of the pitch angle has been investigated for a wide range of tip speed ratios.

The power coefficient, C_p, as a function of the tip speed ratio, λ, has been predicted for a three bladed VAWT with the pitch angles of $\beta = -1, 0, 1, 2, 3$ and 4°. It has been observed in Fig. 7.11(a) that with a more positive β the power coefficient increases at low tip speed ratio. Nevertheless, after $\beta = 2^\circ$ this increment is minimal and for $\lambda = 1.5$ the power coefficient reduces for these pitch angles. Also, the maximum C_p occurs

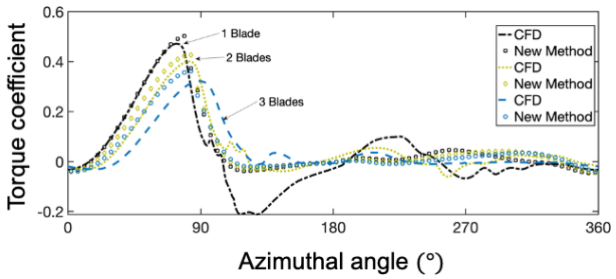

(a)

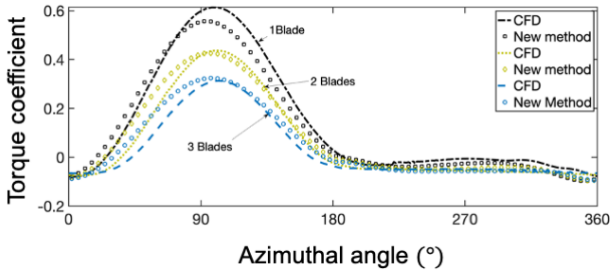

(b)

Figure 7.10: The torque coefficient as a function of the azimuthal angle predicted with the new methodology for one, two and three-bladed VAWTs at (a) $\lambda = 2$ and, (b) $\lambda = 3.5$

at a lower value of λ. In addition, at large tip speed ratios, after the dynamic stall conditions have been reached, the more positive β is, the lower is the power coefficient.

The increase in C_p at low λ values observed in Fig. 7.11(a) is explained to be cause due to mitigation of the stalling conditions at upstream zone of the rotor observed in Fig. 7.11(b): the more positive β is then the angle of attack at upstream reduces its value. A reduction in the maximum angle of attack at upstream reduces the severity on the stall-conditions. In the same manner that β affects the maximum angle of attack (α_{max}) upstream, also affect the value of maximum angle of attack at downstream. If βreduces α_{max} at upstream, then this means that the $abs(\alpha_{max})$ at downstream of the rotor increases. For some tip speed ratios, such as $\lambda = 1.5$, due to this increase in the angle of attack at downstream, then the dynamic stall is also experienced downstream

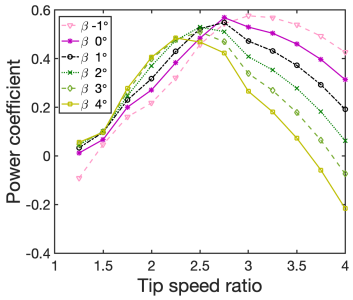

(a)

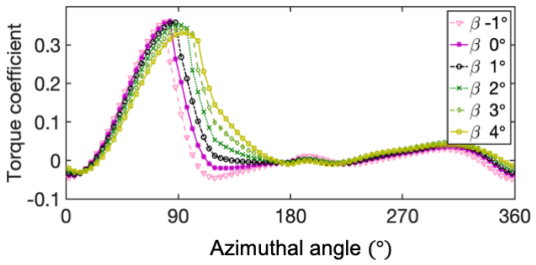

(b)

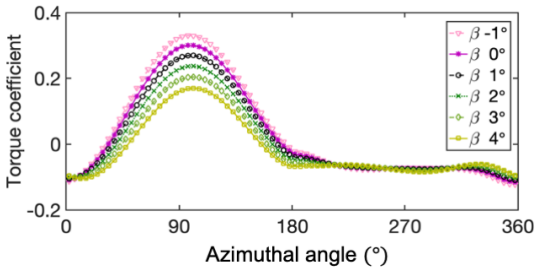

(c)

Figure 7.11: Effect of the pitch angle on a three-bladed VAWT with the NACA0015 aerofoil, (a) the power coefficient as a function of the tip speed ratio, (b) azimuthal torque coefficient at $\lambda = 2$ and, (c) the azimuthal torque coefficient at $\lambda = 4$.

of the rotor and the power coefficient is further reduced.

At large tip speed ratios, after the dynamic stall conditions, the more positive is β then this reduces α_{max} upstream of the rotor and thus, provokes a reduction in the torque coefficient as illustrated in Fig. 7.11(c). This phenomenon is explained due to

the reduction in the maximum angle of attack that reduced the aerodynamic forces upstream and hence the overall torque coefficient. Therefore, accordingly to the final application of the VAWTs and the tip speed ratio of operation, the β value needs to be optimize in order to increase the power coefficient.

7.6 Summary

This chapter has presented an analysis of the curvature effects on the aerodynamic of VAWTs. Some important outcomes have been elucidated, such as the influence of the number of blades on the virtual camber effect. Therefore, the methods to predict the camber effect needs to consider not only the influence of the tip speed ratio but also the influence of the number of blades.

In addition, the interference factor both upstream and downstream of the rotor was analysed and for both sides of the rotor, the interference factor behaves in a sinusoidal function. The equations for the interference factor both upstream and downstream of the rotor as a function of the rotational speed and the solidity has been proposed and verified with the cases investigated in this thesis.

The mathematical expression to estimate the virtual incidence due to the camber effect takes into account the tip speed ratio and the number of blades. This expression, with further verification, is a potential function that may be confidently employed to improve the prediction capabilities of a 1D model for VAWTs.

The methodology presented in this chapter to predict the torque coefficient of VAWTs suggests that these devices need to be analysed as a dynamic system, i.e, interference factor and virtual incidence needs to be investigated with more in-depth detail using unsteady simulations instead using static momentum methods. Further, the momentum methods without a proper assessment such as the large number of conditions tested in this thesis may lead to a fake-good prediction.

Chapter 8

Conclusions and Future work

8.1 Conclusions

In this thesis, an exhaustive analysis of the unsteady aerodynamics of VAWTs has been carried out by using CFD simulations and the new predictions have been rigorously verified with the best available experimental data. As a result, these new CFD predictions have greatly assisted in the proposing of a new methodology to predict the unsteady loads of VAWTs that is based on the Leishman-Beddoes algorithm. The present conclusions are based on the detailed analysis of a wide range of cases: oscillating aerofoils, VAWTs with one, two and three blades; six aerofoils: 4 symmetrical and two cambered and, also covers a wide range of tip speed ratios, namely 1.5-5, where all the aerofoils operate under the dynamic stall and non-stall conditions.

The generated knowledge has allowed the identification of the aerodynamics characteristics that are relevant the most in dictating the performance of the VAWTs. The principal findings of this intensive investigation are summarized as follows:

The dynamic stall-onset angle has been demonstrated to be the most critical parameter in defining the VAWTs performance, i.e. defining the range of tip speed ratio operation. Larger is the stall-onset angle then the lower is the tip speed ratio where the VAWT can produce a positive torque and the optimum power coefficient is observed at a lower value of the tip speed ratio. The stall-onset angle increases its value with the increase of the non-dimensional pitch rate calculated when the angle of attack approaches the static angle. This final value of the non-dimensional pitch rate is dictated by the combined effect of the governing parameter in the VAWTs, namely, the rotational speed, the wind incoming flow, the chord, the pitch angle, the Reynolds number and the aerofoil shape.

The analysis of the torque coefficient, at both upstream and downstream zones of the rotor and using the six different aerofoils, has revealed that: (i) among the two zones, the torque contribution at the downstream zone of the rotor impacts negatively for the total torque coefficient, i.e., its negative magnitude increases with the tip speed ratio for all the aerofoils tested. Therefore, is the main factor that causes the reduction in the total torque coefficient mainly at the tip speed ratios where a fully attached regime is observed. At low tip speed ratios where the dynamic stall is observed at the downstream zone of the rotor, the symmetrical aerofoils NACA0021 and NACA0018 show a torque coefficient with a positive and small torque coefficient.

Under the fully attached regime at upstream the cambered aerofoil S1210 was the aerofoils with the largest torque generation, followed by the cambered NACA2418; the symmetrical aerofoils performed very similarly. Under this fully attached regime and at the downstream zone of the rotor, the cambered S1210 aerofoil was the aerofoil with the most negative torque coefficient generation.

Based in the analysis of the aerofoil profile influence, it is concluded that under the fully attached regime, the lift and drag characteristics of the aerofoils at a negative angle of attack is the most crucial parameter to consider if an improvement in the torque coefficient is pursued. Therefore, as a strategy to increase the performance of VAWTs then morphing blades capable of adjusting their lift and drag coefficient in the downstream region may substantially improve the overall torque coefficient of VAWTs.

The analysis Reynolds number influence on the time delay constant reveals the following outcomes. For the same Reynolds number the three aerofoils studied, the NACA0021, NACA0018 and NACA0015 present a different value in the time-delay constant. Also, the increase of the Reynolds number increases the time delay constant value for the three aerofoils, but this increase becomes less notorious with the increase of the Reynolds number. In addition, the results show that the NACA0021 is the aerofoils with the largest values of time-delay constants and presents a very small increase in the time delays constant values due to the increase in the Reynolds number. Thus, the NACA0021 which the largest stall-onset angles is considered the most potential aerofoil, among the investigated in this thesis, to be used in the design of VAWTs,

especially for devices operating at low wind speed and thus, at low Reynolds numbers.

The modified Leishman-Beddoes algorithm using the time-delay constant as a function of the Reynolds number has been assessed for oscillating aerofoils. The results show this dynamic stall model is able to predict accurately the unsteady loads of oscillating aerofoils under both dynamic stall and fully attached regimes. The assessment of the double multiple streamtube coupled with the Leishman-Beddoes algorithm has demonstrated to fail in the accurate prediction of the torque coefficient at upstream and downstream zones of the rotor. This discrepancy in the predictions was observed mainly under the fully attached regimes.

The virtual incidence angle added by the curvature effects of the rotating blades was investigated by modifying the effective angle of attack in the Leishman-Beddoes algorithm. It has been observed, in agreement with the previous investigations of other authors that the virtual incidence angle increases with the tip speed ratio. The largest estimated virtual incidence angle was 3° and this was observed for the one-bladed VAWT at the tip speed ratio 5. Using this approach to evaluate the curvature effects, it was observed that the increase in the number of blades decreases the value of the virtual incidence angle. Nevertheless, the effect of the number of blades on the curvature requires much more CFD analysis. Since the curvature effects increase the effective angle of attack of the aerofoil, it is a more in depth-investigation that may lead to the development of improved techniques for predicting the power coefficient.

The analysis of the velocity deficit along the streamwise direction of the rotor has been made by using a different number of blades and tip speed ratios. The results have shown that the interference factor at the upstream of the rotor can be accurately represented by a continuous sine function as well as in the downstream zone of the rotor.

The new-proposed method in this thesis was used to investigate the effect of the pitch angle in the performance of the VAWTs. It has been observed that the variation of the pitch angle at high tip speed ratios (under the fully attached regime) produces a huge benefit by increasing the power coefficient. A low tip speed ratios where the dynamic stall phenomenon takes place, if the pitch angle increases the angle of attack, then the overall power coefficient deteriorates. Therefore, the selection of the pitch

angle, if this angle is fixed, depends strongly on the tip speed ratio, but, if a pitch blade control is available, then the power coefficient of the VAWTs can be substantially improved by controlling the pitch angle accordingly to the tip speed ratio of operation.

As the last conclusion, it can be stated that this thesis has substantially contributed to the development of a very deep understanding of the aerodynamics features that are crucial to define the torque coefficient according to the regime of operation of a VAWT and how the performance of VAWTs can be improved by modifying those aerodynamic characteristics. Additionally, the generated knowledge has laid the solid foundations to develop a fast tool that is capable of predicting the power coefficient of VAWTs that is very reliable according to the actual aerodynamics on the blades.

8.2 Future work

The unsteady aerodynamics has been demonstrated to be a very complex subject and in VAWTs this unsteady aerodynamics becomes even more complicated due to the several aspects affecting its performance. Despite this thesis making a huge contribution in the understanding of the unsteady aerodynamics of the VAWTs there are still many aspects that require a much more in depth investigation to guide the theory behind the VAWT performance to a well-known subject, i.e. a well-developed theory.

A possible first interesting investigation consists of the understanding the influence of the Reynolds number (less than 1 million) on the time that the vortex shed from the leading edge travels along the chord up to the trailing edge. Since this means that a fully separated flow needs to be modelled, then experimental tests are highly recommended. This new information would benefit not only the better understanding of the VAWTs aerodynamics but also improve the dynamic stall methods as well as the verification of the large-eddy simulations and other computational fluid dynamics techniques. In addition, a complete design tool for VAWTs needs to consider the structural analysis, i.e. the unsteady momentum coefficient that may affect the bending and other displacements of the blades when the VAWTs are rotating.

Secondly, despite this thesis presenting a new-proposed method that includes the interference factor due to the number of blades, a new method that includes the vir-

tual incidence as a function of the number of blades and tip speed ratio, these results are still limited. Much more investigations using CFD simulations, dealing with the solidity by changing the chord length can lead to a more complete understanding of the interference factor as well as obtaining a more complete mathematical expression that relates the virtual incidence with the tip speed ratio and the solidity. The results from the mentioned future work can lead to a simplified mathematical expression able to compute the power coefficient of the VAWTs and thus considerably reduce the time-consumption of the CFD simulations and give better confidence about the performance of the VAWTs.

Thirdly, the 2D unsteady aerodynamic of the VAWTs, while being the fundamental theory in order to obtain the best power coefficient, it does not take into account the 3D effects of the rotating blade, specifically the dynamic 3D effect of the tip losses. Investigating how the unsteady aerodynamics behaves along the blade from the central vertical position of the blade to the tips are substantially important in order to propose new strategies that mitigate these losses, such as the tip loss devices, but also would contribute substantially to the better understanding of the unsteady aerodynamics of the VAWTs.

REFERENCES

[1] R. K. Angell, P. J. Musgrove, R. A. Galbraith, and R. B. Green, "Summary of the collected data for tests on the NACA 0015, NACA 0018, NACA 0021, NACA 0025 and NACA 0030 aerofoils," tech. rep., University of Glasgow, 1990.

[2] I. Paraschivoiu, *Wind Turbine Design with empasis on Darrieus Concept*. 2002.

[3] A. Sharma and M. Visbal, "Numerical Investigation of the Effect of Airfoil Thickness on Onset of Dynamic Stall," *J. Fluids Mech.*, vol. 870, pp. 870–900, 2019.

[4] T. Lee and P. Gerontakos, "Investigation of flow over an oscillating airfoil," *Journal of Fluid Mechanics*, vol. 512, no. 2004, pp. 313–341, 2004.

[5] D. M. Sharma and K. Poddar, "Investigation of dynamic stall characteristics for flow past an oscillating airfoil at various reduced frequencies by simultaneous PIV and surface pressure measurements," *10th Internationnal symposium on particle image velocimetry -PIV13*, 2013.

[6] A. Rezaeiha, I. Kalkman, and B. Blocken, "CFD simulation of a vertical axis wind turbine operating at a moderate tip speed ratio: guidelines for minimum domain size and azimuthal increment," *Renewable Energy*, 2017.

[7] A.-J. Buchner, J. Soria, D. Honnery, and A. J. Smits, "Dynamic stall in vertical axis wind turbines: scaling and topological considerations," *Journal of Fluid Mechanics*, vol. 841, pp. 746–766, 2018.

[8] D. G. Mabey, "Review of the normal force fluctuations on aerofoils with separated flow," *Progress in Aerospace Sciences*, vol. 29, no. 1, pp. 43–80, 1992.

[9] Q. Li, T. Maeda, Y. Kamada, J. Murata, T. Kawabata, K. Shimizu, T. Ogasawara, A. Nakai, and T. Kasuya, "Wind tunnel and numerical study of a straight-bladed vertical axis wind turbine in three-dimensional analysis (Part I: For predicting aerodynamic loads and performance)," *Energy*, vol. 106, pp. 443–452, 2016.

[10] A. Bianchini, F. Balduzzi, G. Ferrara, and L. Ferrari, "Virtual incidence effect on rotating airfoils in Darrieus wind turbines," *Energy Conversion and Management*, vol. 111, pp. 329–338, 2016.

[11] International Energy Agency (IEA), "World Energy Outlook 2016," tech. rep., 2016.

[12] R. Secretariat, *Renewables 2019 Global Status Report*. Paris: REN21, 2020.

[13] E. Hau, *Wind turbines: Fundamentals, technologies, application, economics*. 2013.

[14] M. R. Islam, S. Mekhilef, and R. Saidur, "Progress and recent trends of wind energy technology," *Renewable and Sustainable Energy Reviews*, vol. 21, pp. 456–468, 2013.

[15] J. F. Manwell, J. G. McGowan, and A. L. Rogers, *Wind Energy Explained*. Wiley, 2nd ed., 2002.

[16] Y. Kumar, J. Ringenberg, S. S. Depuru, V. K. Devabhaktuni, J. W. Lee, E. Nikolaidis, B. Andersen, and A. Afjeh, "Wind energy: Trends and enabling technologies," *Renewable and Sustainable Energy Reviews*, vol. 53, pp. 209–224, 2016.

[17] Z. Simic, J. G. Havelka, and M. Bozicevic Vrhovcak, "Small wind turbines - A unique segment of the wind power market," *Renewable Energy*, vol. 50, pp. 1027–1036, 2013.

[18] T. Burton, N. Jenkins, D. Sharpe, and E. Bossanyi, *Wind Energy Handbook*. Wiley, 2nd ed., 2011.

[19] X. Jin, G. Zhao, K. Gao, and W. Ju, "Darrieus vertical axis wind turbine: Basic research methods," *Renewable and Sustainable Energy Reviews*, vol. 42, pp. 212–225, 2015.

[20] K. Y. Lee, S. H. Tsao, C. W. Tzeng, and H. J. Lin, "Influence of the vertical wind and wind direction on the power output of a small vertical-axis wind turbine installed on the rooftop of a building," *Applied Energy*, 2018.

[21] W. T. Chong, A. Fazlizan, S. C. Poh, K. C. Pan, W. P. Hew, and F. B. Hsiao, "The design, simulation and testing of an urban vertical axis wind turbine with the omni-direction-guide-vane," *Applied Energy*, vol. 112, pp. 601–609, 2013.

[22] C. Li, Y. Xiao, Y. lin Xu, Y. xin Peng, G. Hu, and S. Zhu, "Optimization of blade pitch in H-rotor vertical axis wind turbines through computational fluid dynamics simulations," *Applied Energy*, vol. 212, no. December 2017, pp. 1107–1125, 2018.

[23] Z. Wang and M. Zhuang, "Leading-edge serrations for performance improvement on a vertical-axis wind turbine at low tip-speed-ratios," *Applied Energy*, vol. 208, no. September, pp. 1184–1197, 2017.

[24] M. T. Nguyen, F. Balduzzi, A. Bianchini, G. Ferrara, and A. Goude, "Evaluation of the unsteady aerodynamic forces acting on a vertical-axis turbine by means of numerical simulations and open site experiments," *Journal of Wind Engineering and Industrial Aerodynamics*, 2020.

[25] A. Sagharichi, M. Zamani, and A. Ghasemi, "Effect of solidity on the performance of variable-pitch vertical axis wind turbine," *Energy*, vol. 161, pp. 753–775, 2018.

[26] Y. L. Xu, Y. X. Peng, and S. Zhan, "Optimal blade pitch function and control device for high-solidity straight-bladed vertical axis wind turbines," *Applied Energy*, vol. 242, no. March, pp. 1613–1625, 2019.

[27] S. B. Qamar and I. Janajreh, "Investigation of Effect of Cambered Blades on Darrieus VAWTs," *Energy Procedia*, vol. 105, pp. 537–543, 2017.

[28] M. H. Mohamed, A. M. Ali, and A. A. Hafiz, "CFD analysis for H-rotor Darrieus turbine as a low speed wind energy converter," *Engineering Science and Technology, an International Journal*, vol. 18, no. 1, pp. 1–13, 2015.

[29] A. Rezaeiha, H. Montazeri, and B. Blocken, "Characterization of aerodynamic performance of vertical axis wind turbines: Impact of operational parameters," *Energy Conversion and Management*, vol. 169, no. February, pp. 45–77, 2018.

[30] C. Simão Ferreira, G. Van Kuik, G. Van Bussel, and F. Scarano, "Visualization by PIV of dynamic stall on a vertical axis wind turbine," *Experiments in Fluids*, vol. 46, no. 1, pp. 97–108, 2009.

[31] Q. Li, T. Maeda, Y. Kamada, J. Murata, K. Furukawa, and M. Yamamoto, "The influence of flow field and aerodynamic forces on a straight-bladed vertical axis wind turbine," *Energy*, vol. 111, pp. 260–271, 2016.

[32] Q. Li, T. Maeda, Y. Kamada, J. Murata, K. Furukawa, and M. Yamamoto, "Measurement of the flow field around straight-bladed vertical axis wind turbine," *Journal of Wind Engineering and Industrial Aerodynamics*, vol. 151, pp. 70–78, 2016.

[33] N. Fujisawa and S. Shibuya, "Observations of dynamic stall on turbine blades," *Journal of Wind Engineering and Industrial Aerodynamics*, 2001.

[34] N. F. Krasnov, *Aerodynamics 1: Fundamentals of theory*. Reading, Massachusetts: Mir Publishers Moscow, 1985.

[35] J. G. Leishman, "Challenges in modelling the unsteady aerodynamics of wind turbines," *Wind Energy*, vol. 5, no. 2-3, pp. 85–132, 2002.

[36] W. J. Mccroskey, "Unsteady Airfoils!," *Ann. Rev. Fluid Mech*, vol. 14, pp. 285–311, 1982.

[37] R. Dudley, "Unsteady aerodynamics," 1999.

[38] W. Shyy, Y. Lian, J. Tang, D. Viieru, and H. Liu, *Aerodynamics of low reynolds number flyers*. 2007.

[39] L. W. CARR, "Progress in analysis and prediction of dynamic stall," *Journal of Aircraft*, vol. 25, no. 1, pp. 6–17, 1988.

[40] T. Theodorsen, "General theory of aerodynamic inestability and the mechanism of flutter," tech. rep., National Adivisory Commitee for Aeronautics, 1949.

[41] F. J. Tarzanin, "Prediction of control loads due to blade stall," *27th Annual National Forum of the American Helicopter Society*, 1971.

[42] B. G. van der Wall and J. G. Leishman, "The Influence of Variable Flow Velocity on Unsteady Airfoil Behavior," *Eightteenth European Rotorcraft Forum*, no. 81, 1992.

[43] W. J. Mccroskey, L. W. Carr, and K. W. Mcalister, "Dynamic Stall Experiments on Oscillating Airfoils," *AIAA Journal*, vol. 14, no. 1, pp. 57–63, 1976.

[44] W. J. McCroskey, "The Phenomenon of Dynamic Stall," tech. rep., 1981.

[45] K. W. McAlister, L. W. Carr, and M. W. J., "Dynamic Stall Experiements on the NACA 0012 Airfoil," p. 161, 1978.

[46] J. G. Leishman and T. S. Beddoes, "A generalised model for airofoil unsteady aerodynamic behaviour and dynamic stall using the indicial method," in *42nd Annual Forum of the American He copter Society*, pp. 243–265, 1986.

[47] M. R. Amiralaei, H. Alighanbari, and S. M. Hashemi, "An investigation into the effects of unsteady parameters on the aerodynamics of a low Reynolds number pitching airfoil," *Journal of Fluids and Structures*, vol. 26, no. 6, pp. 979–993, 2010.

[48] E. Dyachuk, A. Goude, and H. Bernhoff, "Dynamic Stall Modeling for the Conditions of Vertical Axis Wind Turbines," *AIAA Journal*, vol. 52, no. 1, pp. 72–81, 2014.

[49] Gupta S. and J. Leishman, "Stall Modeling of a Parked Wind Turbine Blade and Comparison with Experiment," *Proc. of the 43rd AIAA Aerospace Sciences Meeting and Exhibit*, no. January, pp. 1–20, 2005.

[50] K. Gharali and D. A. Johnson, "Dynamic stall simulation of a pitching airfoil under unsteady freestream velocity," *Journal of Fluids and Structures*, vol. 42, pp. 228–244, 2013.

[51] B. Hand, A. Cashman, and G. Kelly, "Numerical simulation of a vertical axis wind turbine airfoil experiencing dynamic stall at high Reynolds numbers (Under Review)," *Computers & Fluids*, vol. 149, pp. 12–30, 2016.

[52] P. Migliore and W. Wolfe, "The Effects of Flow Curvature on the Aerodynamics of Darrieus Wind Turbines," *United States Department of Energy, Division of Solar Energy*, 1980.

[53] E. Dyachuk and A. Goude, "Simulating dynamic stall effects for vertical axis wind turbines applying a double multiple streamtube model," *Energies*, vol. 8, no. 2, pp. 1353–1372, 2015.

[54] Q. Li, T. Maeda, Y. Kamada, J. Murata, K. Furukawa, and M. Yamamoto, "Effect of number of blades on aerodynamic forces on a straight-bladed Vertical Axis Wind Turbine," *Energy*, vol. 90, pp. 784–795, 2015.

[55] G. Brochier, P. Fraunie, C. Beguier, and I. Paraschivoiu, "Water Channel Experiments of Dynamic Stall on Darrieus Wind Turbine Blades," *Journal of Propulsion and Power*, vol. Vol. 2, no. No. 5, pp. pp. 445 – 449, 1986.

[56] B. F. Blackwell, R. E. Sheldahl, and L. V. Feltz, "Wind Tunnel Performance Data for the Darrieus Wind Turbine with NACA 0012 Blades," Tech. Rep. May, Sandia Laboratories, 1976.

[57] M. H. Worstell, "Aerodynamic Performance of the 17 Meter Diameter Darrieus Wind Turbine," no. September, 1978.

[58] K. Mulleners and M. Raffel, "The onset of dynamic stall revisited," *Experiments in Fluids*, vol. 52, no. 3, pp. 779–793, 2012.

[59] P. Vittecoq and A. Laneville, "The aerodynamic forces for a Darrieus rotor with straight blades: Wind tunnel measurements," *Journal of Wind Engineering and Industrial Aerodynamics*, vol. 15, no. 1-3, pp. 381–388, 1983.

[60] M. Rossander, E. Dyachuk, S. Apelfröjd, K. Trolin, A. Goude, H. Bernhoff, and S. Eriksson, "Evaluation of a Blade Force Measurement System for a Vertical Axis Wind Turbine Using Load Cells," *Energies*, vol. 8, no. 6, pp. 5973–5996, 2015.

[61] Y. X. Peng, Y. L. Xu, S. Zhan, and K. M. Shum, "High-solidity straight-bladed vertical axis wind turbine: Aerodynamic force measurements," *Journal of Wind Engineering and Industrial Aerodynamics*, 2019.

[62] F. Balduzzi, A. Bianchini, R. Maleci, G. Ferrara, and L. Ferrari, "Critical issues in the CFD simulation of Darrieus wind turbines," *Renewable Energy*, vol. 85, pp. 419–435, 2016.

[63] A. Rezaeiha, H. Montazeri, and B. Blocken, "Towards optimal aerodynamic design of vertical axis wind turbines: Impact of solidity and number of blades," *Energy*, vol. 165, pp. 1129–1148, 2018.

[64] A. Rezaeiha, H. Montazeri, and B. Blocken, "Characterization of aerodynamic performance of vertical axis wind turbines: Impact of operational parameters," *Energy Conversion and Management*, vol. 169, no. February, pp. 45–77, 2018.

[65] W. Sheng, R. A. Galbraith, and F. N. Coton, "Prediction of Dynamic Stall Onset for Oscillatory Low-Speed Airfoils," *Journal of Fluids Engineering*, vol. 130, no. 10, p. 101204, 2008.

[66] N. Guillaud, G. Balarac, and E. Goncalvès, "Large Eddy Simulations on a pitching airfoil: Analysis of the reduced frequency influence," *Computers and Fluids*, 2018.

[67] D. H. Kim and J. W. Chang, "Low-Reynolds-number effect on the aerodynamic characteristics of a pitching NACA0012 airfoil," *Aerospace Science and Technology*, vol. 32, no. 1, pp. 162–168, 2014.

[68] Y. Kim and Z.-T. Xie, "Modelling the effect of freestream turbulence on dynamic stall of wind turbine blades," *Computers & Fluids*, vol. 129, pp. 53–66, 2016.

[69] F. Geng, I. Kalkman, A. S. Suiker, and B. Blocken, "Sensitivity analysis of airfoil aerodynamics during pitching motion at a Reynolds number of 1.35×10^5," *Journal of Wind Engineering and Industrial Aerodynamics*, vol. 183, no. November, pp. 315–332, 2018.

[70] A. Sharma and M. R. Visbal, "Airfoil Thickness Effects on Dynamic Stall Onset," *23rd AIAA Computational Fluid Dynamics Conference*, no. June, 2017.

[71] M. R. Visbal and D. J. Garmann, "Analysis of Dynamic Stall on a Pitching Airfoil Using High-Fidelity Large-Eddy Simulations," *AIAA Journal*, 2017.

[72] A. J. Buchner, M. W. Lohry, L. Martinelli, J. Soria, and A. J. Smits, "Dynamic stall in vertical axis wind turbines: Comparing experiments and computations," *Journal of Wind Engineering and Industrial Aerodynamics*, vol. 146, pp. 163–171, 2015.

[73] Q. Li, T. Maeda, Y. Kamada, Y. Hiromori, A. Nakai, and T. Kasuya, "Study on stall behavior of a straight-bladed vertical axis wind turbine with numerical and experimental investigations," *Journal of Wind Engineering and Industrial Aerodynamics*, vol. 164, no. January, pp. 1–12, 2017.

[74] A. Choudhry, R. Leknys, M. Arjomandi, and R. Kelso, "An insight into the dynamic stall lift characteristics," *Experimental Thermal and Fluid Science*, vol. 58, pp. 188–208, 2014.

[75] G. B. Mccullough and D. E. Gault, "Examples of Three Representative Types of Airfoil-section Stall at Low Speed. Technical Note 2502," tech. rep., National Advisory Committee for Aeronautics, 1951.

[76] J. W. Larsen, S. R. Nielsen, and S. Krenk, "Dynamic stall model for wind turbine airfoils," *Journal of Fluids and Structures*, vol. 23, no. 7, pp. 959–982, 2007.

[77] J. H. Strickland and G. Graham, "Dynamic stall inception correlation for airfoils undergoing constant pitch rate motions," *AIAA Journal*, vol. 24, no. 4, pp. 678–680, 1985.

[78] J. Walker, H. Helin, and D. Chou, "Unsteady Surface Pressure Measurements on a Pitching Airfoil," in *AIAA Shear Flow Control Conference, Colorado*, 1985.

[79] J. Strickland and G. Graham, "Force coefficients for a NACA0015 airfoil undergoing constant pitch rate motions," *AIAA Journal*, vol. 25, pp. 622–624, 1987.

[80] S. J. Schreck, W. E. Faller, and M. C. Robinson, "Unsteady separation processes and leading edge vortex precursors: Pitch rate and reynolds number influences," *Journal of Aircraft*, vol. 39, no. 5, pp. 868–875, 2002.

[81] J. Walker, H. Helin, and J. Strickland, "An experimental investigation of an airfoil undergoing large-amplitude pitching motion," *AIAA Journal*, vol. 23, no. 8, pp. 1142–1985, 1985.

[82] D. Daley and E. Jumper, "Experimental investigation of dynamic stall for a pitching airfoil," *AIAA Journal*, vol. 21, no. 10, pp. 831–832, 1984.

[83] K. Lu, Y. H. Xie, D. Zhang, and J. B. Lan, "Numerical investigations into the asymmetric effects on the aerodynamic response of a pitching airfoil," *Journal of Fluids and Structures*, vol. 39, pp. 76–86, 2013.

[84] B. Rocchio, C. Chicchiero, M. V. Salvetti, and S. Zanforlin, "A simple model for deep dynamic stall conditions," *Wind Energy*, no. November 2019, pp. 1–24, 2020.

[85] F. Scheurich and R. E. Brown, "Effect of Dynamic Stall on the Aerodynamics of Vertical-Axis Wind Turbines," *AIAA Journal*, vol. 49, no. 11, pp. 2511–2521, 2011.

[86] P. A. Kozak, D. Vallverdú, and D. Rempfer, "Modeling vertical-axis wind-turbine performance: Blade-Element method versus finite volume approach," *Journal of Propulsion and Power*, vol. 32, no. 3, pp. 592–601, 2016.

[87] A. Laneville and P. Vittecoq, "Dynamic Stall: The Case of the Vertical Axis Wind Turbine," *Transactions of the ASME*, vol. 108, no. May 1986, pp. 140–145, 1986.

[88] J. Edwards, L. A. Danao, and R. J. Howell, "PIV measurements and CFD simulation of the performance and flow physics and of a small-scale vertical axis wind turbine," *Wind Energy*, vol. 18, pp. 201–217, 2015.

[89] F. R. Menter, R. B. Langtry, S. R. Likki, Y. B. Suzen, P. G. Huang, and S. Völker, "A Correlation-Based Transition Model Using Local Variables - Part I: Model Formulation," *Journal of Turbomachinery*, vol. 128, no. 3, p. 413, 2006.

[90] P. Durbin, "An intermittency model for bypass transition," *International Journal of Heat and Fluid Flow*, vol. 36, pp. 1–6, 2012.

[91] B. Andersson, R. Andersson, L. Håkansson, M. Mortensen, R. Sudiyo, and B. Van Wachem, *Computational fluid dynamics for engineers*. 2011.

[92] R. Bravo, S. Tullis, and S. Ziada, "Performance testing of a small vertical-axis wind turbine," *21st Canadian Congress of Applied Mechanics CANCAM*, no. September, pp. 2–3, 2007.

[93] Q. Li, T. Maeda, Y. Kamada, J. Murata, K. Shimizu, T. Ogasawara, A. Nakai, and T. Kasuya, "Effect of solidity on aerodynamic forces around straight-bladed vertical axis wind turbine by wind tunnel experiments (depending on number of blades)," *Renewable Energy*, vol. 96, pp. 928–939, 2016.

[94] P. Ouro, T. Stoesser, and L. Ramirez, "Effect of blade cambering on dynamic stall in view of designing vertical axis turbines," *Journal of Fluids Engineering*, vol. 140, no. June, pp. 1–12, 2018.

[95] J. A. Ekaterinaris and M. F. Platzer, "Computational prediction of airfoil dynamic stall," *Progress in Aerospace Sciences*, vol. 33, no. 11-12, pp. 759–846, 1998.

[96] A. S. Rezaei and H. Taha, "Transition regime and its effects on the unsteady aerodynamic characteristics of a pitching airfoil," in *AIAA Scitech 2019 Forum*, no. January, pp. 1–13, 2019.

[97] M. Ge, H. Zhang, Y. Wu, and Y. Li, "Effects of leading edge defects on aerodynamic performance of the S809 airfoil," *Energy Conversion and Management*, vol. 195, no. April, pp. 466–479, 2019.

[98] F. J. Kelecy, "Coupling Momentum and Continuity Increases CFD Robustness," *ANSYS Advantage*, vol. II, no. 2, pp. 49–51, 2008.

[99] F. Trivellato and M. Raciti Castelli, "On the Courant-Friedrichs-Lewy criterion of rotating grids in 2D vertical-axis wind turbine analysis," *Renewable Energy*, vol. 62, pp. 53–62, 2014.

[100] K. M. Almohammadi, D. B. Ingham, L. Ma, and M. Pourkashan, "Computational fluid dynamics (CFD) mesh independency techniques for a straight blade vertical axis wind turbine," *Energy*, vol. 58, pp. 483–493, 2013.

[101] S. I. Benton and M. R. Visbal, "The onset of dynamic stall at a high, transitional Reynolds number," *Journal of Fluid Mechanics*, vol. 861, pp. 860–885, 2019.

[102] A. Rezaeiha, H. Montazeri, and B. Blocken, "On the accuracy of turbulence models for CFD simulations of vertical axis wind turbines," *Energy*, 2019.

[103] A. Rezaeiha, H. Montazeri, and B. Blocken, "Towards accurate CFD simulations of vertical axis wind turbines at different tip speed ratios and solidities: Guidelines for azimuthal increment, domain size and convergence," *Energy Conversion and Management*, vol. 156, no. November 2017, pp. 301–316, 2018.

[104] C. S. Ferreira, H. A. Madsen, M. Barone, B. Roscher, P. Deglaire, I. Arduin, and I. Arduin, "Comparison of aerodynamic models for Vertical Axis Wind Turbines," *Journal of Physics: Conference Series*, vol. 524, p. 012125, 2014.

[105] Z. Cheng, H. A. Madsen, Z. Gao, and T. Moan, "Aerodynamic Modeling of Floating Vertical Axis Wind Turbines Using the Actuator Cylinder Flow Method," *Energy Procedia*, vol. 94, no. 1876, pp. 531–543, 2016.

[106] D. Vallverdú, *Study on vertical axis wind turbine using streamtube and dynamic stall models*. PhD thesis, Univerisitat Politecnica de Catalunya, 2014.

[107] P. Jain and A. Abhishek, "Performance prediction and fundamental understanding of small scale vertical axis wind turbine with variable amplitude blade pitching," *Renewable Energy*, vol. 97, pp. 97–113, 2016.

[108] I. Paraschivoiu, "Double-Multiple Streamtube Model for Studying VAWT's," *Journal of Propulsion and Power*, vol. 4, no. 4, pp. 370–378, 1988.

[109] O. Eboibi, L. A. M. Danao, and R. J. Howell, "Experimental investigation of the influence of solidity on the performance and flow field aerodynamics of vertical axis wind turbines at low Reynolds numbers," *Renewable Energy*, vol. 92, pp. 474–483, 2016.

[110] J. McNaughton, F. Billard, and A. Revell, "Turbulence modelling of low Reynolds number flow effects around a vertical axis turbine at a range of tip-speed ratios," *Journal of Fluids and Structures*, vol. 47, pp. 124–138, 2014.

[111] W. Sheng, R. Galbraith, and F. Coton, *A new stall onset criterion for low speed dynamic stall*. PhD thesis, 2006.

[112] I. H. Abbott and A. E. Von Doenhoff, *Theory of Wing Sections: Including a Summary of Airfoil data*. first ed., 1959.

[113] R. Gerakopulos, M. S. H. Boutilier, and S. Yarusevych, "Aerodynamic Characterization of a NACA 0018 Airfoil at Low Reynolds Numbers," *40th Fluid Dynamics Conference and Exhibit*, no. July, pp. 1–13, 2010.

[114] R. Carlson, R. Blackwell, G. Commerford, and P. Mirick, "Dynamic stall modelling and correlation with experimental data on airfoils and rotors," in *AHS/NACA-Ames Specialists Meeting on Rotorcraft Dynamics*, 1974.

[115] M. Elgammi and T. Sant, "A Modified Beddoes-Leishman Model for Unsteady Aerodynamic Blade Load Computations on Wind Turbine Blades," *Journal of Solar Energy Engineering*, vol. 138, no. October 2016, pp. 1–18, 2016.

[116] E. N. Jacobs and A. Sherman, "Airfoil section characteristics as affected by variations of the Reynold number. Report No. 586," tech. rep., National Advisory Committee for Aeronautics, 1939.

[117] M. Selig, J. J. Guglielmo, A. P. Broeren, and P. Giguere, *Summary of Low-Speed Airfoil Data Summary of Low-Speed Airfoil Data*, vol. 1. 1995.

[118] G. J. Bingham and K. W. Noonan, "Low-speed aerodynamic characteristics 35 percentage-chord single-slotted flaps," Tech. Rep. TM X-2623, NASA, 1974.

[119] M. Elkhoury, T. Kiwata, and E. Aoun, "Experimental and numerical investigation of a three-dimensional vertical-axis wind turbine with variable-pitch," *Journal of Wind Engineering and Industrial Aerodynamics*, vol. 139, pp. 111–123, 2015.

[120] L. A. Danao, N. Qin, and R. Howell, "A numerical study of blade thickness and camber effects on vertical axis wind turbines," *Journal of Power and Energy*, vol. 226, no. 7, pp. 867–881, 2012.

[121] M. D. Bausas and L. A. M. Danao, "The aerodynamics of a camber-bladed vertical axis wind turbine in unsteady wind," *Energy*, 2015.

[122] M. Jafari, A. Razavi, and M. Mirhosseini, "Effect of airfoil profile on aerodynamic performance and economic assessment of H-rotor vertical axis wind turbines," *Energy*, 2018.

[123] J. Healy, "The Influence of Blade Camber on the Output of Vertical-Axis Wind Turbines," *Wind Engineering*, vol. 2, no. 3, pp. 146–155, 1978.

[124] W. J. McCroskey, K. McAlister, L. Carr, and S. Pucci, "An experimental study on Dynamic Stall on Advanced Airfoil Sections Volume 1 Summary of the experiments," tech. rep., National Aeronautics and Space Administration, 1982.

[125] M. H. Hansen, M. Gaunaa, and H. Aasaard Madsen, "A Beddoes-Leishman type dynamic stall model in state-space and indicial formulations," tech. rep., Technical University of Denmarck, 2004.

[126] S. Gupta and J. G. Leishman, "Dynamic stall modelling of the S809 aerofoil and comparison with experiments," *Wind Energy*, vol. 9, no. 6, pp. 521–547, 2006.

[127] Z. Zhao, C. Yan, T. Wang, B. Xu, and Y. Zheng, “Study on approach of performance improvement of VAWT employing double multiple stream tubes model,” *Journal of Renewable and Sustainable Energy*, vol. 9, no. 2, p. 023305, 2017.

[128] E. Saber, R. Afify, and H. Elgamal, “Performance of SB-VAWT using a modified double multiple streamtube model,” *Alexandria Engineering Journal*, vol. 57, no. 4, pp. 3099–3110, 2018.

[129] A. Bianchini, D. Marten, A. Tonini, F. Balduzzi, C. N. Nayeri, G. Ferrara, and C. O. Paschereit, “Implementation of the ”virtual Camber” Transformation into the Open Source Software QBlade: Validation and Assessment,” *Energy Procedia*, vol. 148, no. Ati, pp. 210–217, 2018.

[130] D. Keisar, T. De Troyer, and D. Greenblatt, “Concept and operation of a wind turbine driven by dynamic stall,” *AIAA Journal*, vol. 58, no. 6, pp. 2370–2376, 2020.

[131] J. G. Leishman and T. S. Beddoes, “A Semi-Empirical Model for Dynamic Stall,” in *42nd Annual Forum of the American Helicopter Society*, vol. 34, pp. 3–17, 1986.

[132] J. Leishman and G. L. Crouse, “State-space model for unsteady airfoil behavior and dynamic stall,” in *90th Structures, structural dynamics and materials Conferences. Mobile, Alabama, april 3-5, 1989*, pp. 1372–1382, 1989.

[133] J. G. Leishman and K. Q. Nguyen, “State-space representation of unsteady airfoil behavior,” *AIAA Journal*, vol. 28, no. 5, pp. 836–844, 1990.

[134] J. G. Leishman, “Validation of approximate indicial aerodynamic functions for two-dimensional subsonic flow,” *Journal of Aircraft*, vol. 25, no. 10, pp. 914–922, 1988.

Appendix A

Original algorithm of the Leishman-Beddoes dynamic stall model

After several investigations, Leishman and Beddoes (LB) studied how the vortex provokes the overshoot in the lift coefficient [46, 131, 132, 133]. They proposed the methodology to be explained in this section, to compute the dynamic forces produced by an aerofoil under unsteady conditions. The three stages that the model considers are: (i) during the attached flow regime, (ii) during the onset stall and, (iii) during the separated flow.

A.1 Unsteady Attached flow

During the dynamic movement, the flow around the aerofoil experiences a state of attached flow regime. The LB model calculates the attached response using the Kirchhoff flow parameters as explained in Section 6.2.2.

To compute the normal force in this state, C_N^P, indicial functions have been used. An indicial function is defined as "the response to a disturbance which is applied instantaneously at time zero and held constant after that" [46]. In the case of a pitching motion, the disturbances are due to the step change in the angle of attack and to the pitch rate, in other words due to the variation with the time in the angle of attack and in the pitch rate. The indicial functions are full describe in Leishman [134].

The total aerodynamic force under the attached regime and considering a step change in the angle of attack and in the pitch rate is computed as follows:

$$C_{N_n}^P = C_{N_n}^C + C_{N\alpha_n}^I + C_{Nq_n}^I \tag{A.1}$$

Where the first component, C_N^C, represents the circulatory response (this term in-

clude the step change in the attack angle and the pitch rate). The second term, $C^I_{N\alpha}$, represents the impulsive response considering only a step change in the angle of attack, and the third term, C^I_{Nq}, describes the impulsive response due to the pitch rate step change. To compute the circulatory component for the normal force $C^C_{N_n}$, the slope of the static lift coefficients $C_{N\alpha}$ is used :

$$C^C_{N_n} = C_{N\alpha}\alpha_{E_n} \tag{A.2}$$

$$\alpha_{E_n} = \alpha_n + r_n/2 - X_n - Y_n \tag{A.3}$$

$$X_n = X_{n-1}e^{(-b_1\gamma^2\Delta s)} + A_1\Delta\alpha_n e^{(-b_1\gamma^2\Delta s/2)} \tag{A.4}$$

$$Y_n = Y_{n-1}e^{(-b_2\gamma^2\Delta s)} + A_2\Delta\alpha_n e^{(-b_2\gamma^2\Delta s/2)} \tag{A.5}$$

where M is the Mach number. The normalize pitch rate is defined as $r = \dot{\alpha}c/V$ and the attack angle by α. The constant A_1, A_2, b_1, b_2 are defined by the indicial function and their values are fixed to 0.3, 0.7, 0.14, and 0.23, respectively, and those values are independent of the aerofoil.

The factor of compressibility is $\gamma = \sqrt{(1-M^2)}$. The time constant $\Delta s = 2V\Delta t_n/c$, where $\Delta t = t_n - t_{n-1}$ represents the difference between the current time and the previous time. Due to the continuity in the pitching motion, $t(0) = t(n)$.

For the impulsive response due to the step change in the attack angle, the Equation (A.6) is used.

$$C^I_{N\alpha} = (4K_\alpha T_I/M)(D\alpha_n - D_{In}) \tag{A.6}$$

$$D_{In} = D_{I(n-1)}e^{(-\Delta t/K_a T_I)} + (D\alpha_n - D\alpha_{n-1})e^{(-\Delta t/2K_a T_I)} \tag{A.7}$$

where $D\alpha_n = \Delta\alpha_n/\Delta t$, $K_\alpha = \frac{1}{(1-M)+\pi\gamma M^2(A_1b_1+A_2b_2)}$, and $T_I = c/a$

Due to the pitch rate at 3/4 about the axis, the impulsive component is computed using the Equation is (A.8).

$$C^I_{Nq} = (-K_q T_I/M)(Dq_n - D_{qn}) \tag{A.8}$$

$$D_{qn} = D_{q(n-1)}e^{(-\Delta t/K_q T_I)} + (Dq_n - Dq_{n-1})e^{(-\Delta t/2K_q T_I)} \tag{A.9}$$

where $Dq_n = \Delta r_n/\Delta t$, and $K_q = \frac{1}{(1-M)+2\pi\gamma M^2(A_1b_1+A_2b_2)}$.

For the corresponding chordwise force coefficient in this attached state, the following equation is employed.

$$C_C^P = C_{N\alpha}\alpha_E^2 \tag{A.10}$$

A.2 Stall onset

For unsteady conditions, there is a lag in the pressure response and then the attack angle at which the stall starts is delayed, i.e. the angle of attack at which the stall onset occurs is greater than the static angle. This compensation to the normal force C_N^P is as follows:

$$C_N^{'} = C_{Nn}^P - D_{Pn} \tag{A.11}$$

$$D_{Pn} = D_{Pn-1}e^{(-\Delta s/T_p)} + (C_{Nn}^P - C_{Nn-1}^P)e^{(-\Delta s/2T_p)} \tag{A.12}$$

Thus, if $C_N^{'} > C_{N1}$ then there is a stall condition, where C_{N1} is the static stall lift force and T_p is an empirical constant related to the delay pressure response and its value is 1.7. In unsteady conditions, due to this lag in the pressure, a new effective flow separation point is calculated as follows:

$$\alpha_f = C_N^{'}/C_{N\alpha} \tag{A.13}$$

A.3 Separated flow

With the increase of the angle of attack, the flow at the trailing edge of the aerofoils starts its separation. The dimensionless position along the aerofoil surface where the boundary layer detaches is called the trailing edge separation point, $f = x/c$. As described in Section 6.2.2 the Kirchhoff flow model related the separation point, f with the static lift force coefficient. Therefore, the empirical parameters required to model the separation point with the angle of attack can be found following the procedure described in Section 6.2.2.

In addition to the lag in the pressure, during the dynamic conditions, the separation of the boundary layer, f is time dependent, and the vortex formation induced an overshoot in the lift coefficient that is computed as described in the following sections.

A.3.1 Trailing edge separated module

The dynamic separated boundary layer is calculated using a first lag in the separation point (f'). This lag due to the delay in the pressure response is computed with the following equations:

$$f' = \begin{cases} 1 - 0.3\exp(\alpha_f - \alpha_1)/S_1 & \text{if } \alpha_f \leq \alpha_1 \\ 0.04 + 0.66\exp(\alpha_1 - \alpha_f)/S_2 & \text{si } \alpha_f > \alpha_1 \end{cases} \tag{A.14}$$

A second lag, due to the unsteady boundary layer response, is included as follows:

$$f'' = f' - D_f \tag{A.15}$$

$$D_f = D_{f(n-1)}\exp\left(\frac{-\Delta s}{T_f}\right) + (f'_n - f'_{n-1})\exp\left(\frac{-\Delta s}{2T_f}\right) \tag{A.16}$$

where T_f, is the time constant which controls the velocity of the boundary layer flow. This time constant has a value of three, and the vortex has an influence in its behaviour.

The normal force, C_N^f, incorporating the effects of the unsteady behaviour of the boundary layer is given by [131, 46],

$$C_N^f = C_N^C\left(\frac{1+\sqrt{f''}}{2}\right)^2 + C_N^I \tag{A.17}$$

The chordwise force coefficient due to the dynamic boundary layer, is given by following expression.

$$C_C^f = \eta C_{N\alpha}\alpha_E^2\sqrt{f''} \tag{A.18}$$

where $\eta = 0.95$.

A.3.2 Vortex shedding

The objective of this part of the model is to calculate the overshoot in the normal coefficient due to the formation of the vortex. The vortex is shed when $C'_N \geq C_{N1}$ ($\tau = 0$), then the over lift due to the vortex is computed using the following equation:

$$C_v = C_N^C\left(1 - \left(\frac{1+\sqrt{f''}}{2}\right)^2\right) \tag{A.19}$$

This vortex lift force exits during the development of the vortex over the chord, i.e. after the aerofoil reaches the trailing edge $C_v = 0$. At this point ($\tau = T_{vl}$), where T_{vl} is a non-dimensional parameter that has been studied experimentally and represents the travel of the centre of pressure of the aerofoil.

The normal force due to the vortex, C_N^v, decays at each time and is accumulated with a new increment in the vortex lift as follows:

$$C_N^v = C_{N(n-1)}^v \exp\left(\frac{-\Delta S}{T_v}\right) + (C_{v(n)} - C_{v(n-1)}) \exp\left(\frac{-\Delta S}{2T_v}\right) \tag{A.20}$$

where T_v is the non-dimensional time constant that controls the velocity of the movement of the vortex during its development. After the vortex reaches the trailing edge, the vortex lift is zero, $C_v = 0$, thus, the normal force due to the vortex is represented as follows.

$$C_N^v = C_{N(n-1)}^v \exp\left(\frac{-\Delta S}{T_v}\right) \tag{A.21}$$

The normal force due to the vortex when the vortex passes the trailing edge is dissipated faster, i.e., T_v is halved after the trailing edge.

Finally, the normal force is calculated using the following equation:

$$C_N = C_N^f + C_N^v \tag{A.22}$$

and the chordwise force coefficient is represented by next equation:

$$C_C = \begin{cases} C_{L\alpha}\alpha^2\sqrt{f''} - C_{D0} & f(\alpha) > 0.7 \\ C_{L\alpha}\alpha^2(f'' - E_0) - C_{D0} & f(\alpha) < 0.7 \end{cases} \tag{A.23}$$

Appendix B

Interference factor

This section includes the maximum values of the interferences factor for 22 CFD simulations performed in Chapter 5. The CFD simulations consist of VAWTs using one, two and three blades. These VAWTs were tested at the range of Reynolds number of 1.5-5. The maximum interference factors were calculated at the x positions of $-1D$, $0D$ and $1D$. Therefore in Fig. B.1 the linear regression that adjusted the most the interferences factor are presented.

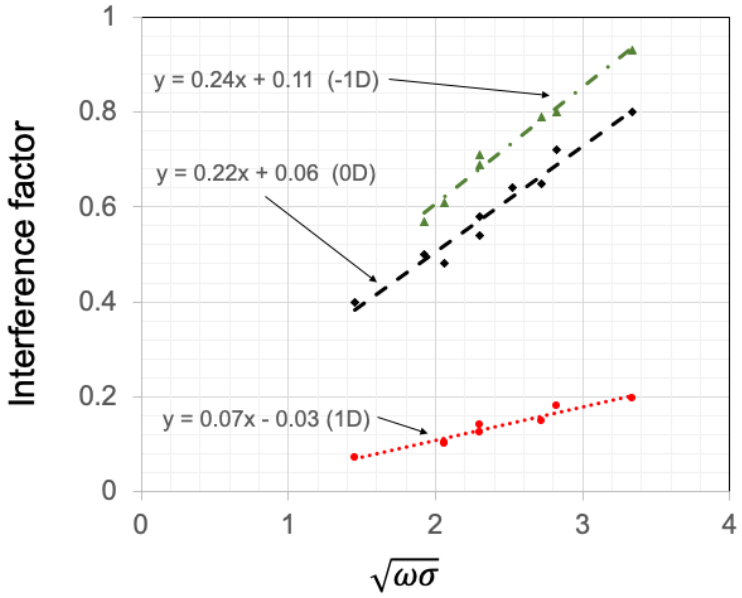

Figure B.1: Linear adjustment of the maximum values of the interference factors at three positions along the x-axis, -1D, 0D and 1D for VAWTs with one, two and three blades and several tip speed ratios.